

ASTRONOMICAL INSTITUTE
SLOVAK ACADEMY OF SCIENCES

SPECIAL ISSUE
**ASTROPHYSICAL SPECTROSCOPY:
A&M DATA -
ATMOSPHERE**

Based on lectures presented at
IV Meeting on Astrophysical Spectroscopy:
A&M DATA - Atmosphere
Andrevlje, Serbia, May 30 - June 2, 2022

**CONTRIBUTIONS
OF THE ASTRONOMICAL OBSERVATORY
SKALNATÉ PLESO**

• VOLUME LII •

Number 3



December 2022

Editorial Board

Editor-in-Chief

Augustín Skopal, *Tatranská Lomnica, The Slovak Republic*

Managing Editor

Richard Komžík, *Tatranská Lomnica, The Slovak Republic*

Editors

Drahomír Chochol, *Tatranská Lomnica, The Slovak Republic*

Július Koza, *Tatranská Lomnica, The Slovak Republic*

Aleš Kučera, *Tatranská Lomnica, The Slovak Republic*

Luboš Neslušan, *Tatranská Lomnica, The Slovak Republic*

Vladimír Porubčan, *Bratislava, The Slovak Republic*

Theodor Pribulla, *Tatranská Lomnica, The Slovak Republic*

Advisory Board

Bernhard Fleck, *Greenbelt, USA*

Arnold Hanslmeier, *Graz, Austria*

Marian Karlický, *Ondřejov, The Czech Republic*

Tanya Ryabchikova, *Moscow, Russia*

Giovanni B. Valsecchi, *Rome, Italy*

Jan Vondrák, *Prague, The Czech Republic*

©

Astronomical Institute of the Slovak Academy of Sciences
2022

ISSN: 1336–0337 (on-line version)

CODEN: CAOPF8

Editorial Office: Astronomical Institute of the Slovak Academy of Sciences
SK - 059 60 Tatranská Lomnica, The Slovak Republic

CONTENTS

List of participants	8
Preface	13

**Session A: BROADENING EFFECTS IN SPECTRAL
LINE SHAPES: ASTROPHYSICS**

A01: M.S. Dimitrijević, M. Christova and S. Sahal-Bréchet: On the similarities of Stark broadening parameters within a Fe XXV multiplet	15
A02: M.S. Dimitrijević, M. Christova and S. Sahal-Bréchet: Stark broadening of Si II spectral lines: comparison with experimental results	25
A03: Z. Simić , M.S. Dimitrijević , S. Sahal-Bréchet and N.M. Sakan On the Stark broadening parameters of Sn III spectral lines	35
A04: L. Abu El Maati, M. Ahmad, I.S. Mahmoud, S.G. Tawfik, N. Alwadii, N. Ben Nessib and M.S. Dimitrijević Atomic structure and transition parameters of the V XVIII carbon-like ion	44

**Session B: A&M PARAMETERS AND DATABASES IN ASTRO-
PHYSICS**

B01: V. Vujčić, V.A. Srećković and D. Jevremović: New database for collisional excitation/ ionization processes of astrophysical interest	71
B02: Ž.D. Nikitović and Z.M. Raspopović: Transport coefficients for He⁺ ions in mixtures He/CF₄: modeling laboratory and astrophysical plasmas	78
B03: V.A. Srećković, Lj.M. Ignjatović and M.S. Dimitrijević: Electron-impact processes involving small molecular ions relevant for the astrochemistry	90
B04: N.M. Sakan, I. Traparić, V.A. Srećković, and M. Ivković: The usage of perceptron, feed and deep feed forward artificial neural networks on the spectroscopy data: astrophysical & fusion plasmas	97

Session C: A&M DATA - ATMOSPHERE

MODELS

C01: A. Kolarski, V.A. Srećković and Z.R. Mijić : Monitoring solar activity during 23/24 solar cycle minimum through VLF radio signals	105
C02: D. Petković, O. Ođalović and A. Nina Influence of the solar hydrogen Lyα line on the GNSS signal delay in the ionospheric D-region	116
C03: M.S. Rabasović, B.P. Marinković and D. Šević: Analysis of laser induced plasma plume in atmosphere using deep learning	126
C04: A. Nina, V.M. Čadež, L.Č. Popović and M. Radovanović: Influence of variations in the solar hydrogen Lyα radiation on the ionospheric D-region electron density during a year and solar cycle	132

The Contributions of the Astronomical Observatory Skalnaté Pleso
are available in a full version
in the frame of ADS Abstract Service
and can be downloaded in a usual way from the URL address:

‘http://adsabs.harvard.edu/article_service.html‘

as well as from the web-site of
the Astronomical Institute of the Slovak Academy of Sciences
on the URL address:

‘<http://www.astro.sk/caosp/>‘

The journal is covered/indexed by:

Thomson Reuters services (ISI)

Science Citation Index Expanded (also known as SciSearch®)
Journal Citation Reports/Science Edition

SCOPUS

SPECIAL ISSUE
**ASTROPHYSICAL SPECTROSCOPY:
A&M DATA - ATMOSPHERE**

Edited by

Vladimir A. Srećković, Milan S. Dimitrijević,
Nikola Cvetanović

Based on lectures presented at
**IV MEETING ON ASTROPHYSICAL
SPECTROSCOPY:
A&M DATA - ATMOSPHERE**

May 30 – June 2, 2022, Andrevlje, Serbia

Institute of Physics Belgrade, University of Belgrade

<http://www.asspectro2022.ipb.ac.rs/>

Scientific Organizing Committee

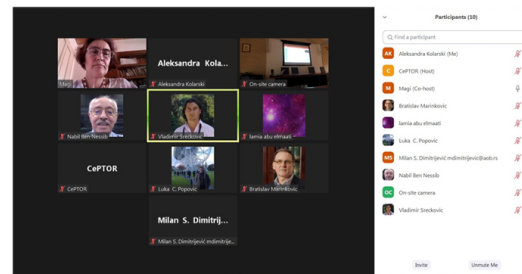
Vladimir A. Srećković, co-chair (Serbia)
Milan S. Dimitrijević, co-chair (Serbia)
Nikolay Bezuglov (Russia)
Nebil Ben Nessib (Saudi Arabia)
Nikola Cvetanović (Serbia)
Saša Dujko (Serbia)
Stevica Djurović (Serbia)
Rafik Hamdi (Tunisia)
Magdalena Hristova (Bulgaria)
Darko Jevremović (Serbia)
Bratislav Marinković (Serbia)
Zoran Mijić (Serbia)
Aleksandra Nina, (Serbia)
Bratislav Obradović (Serbia)
Luka Č. Popović (Serbia)
Branko Predojević (Republic of Srpska)
Maja Rabasović (Serbia)
Sylvie Sahal-Bréchet (France)

Local Organizing Committee

Nikola Veselinović, secretary
Lazar Gavanski
Nataša Simić
Veljko Vujčić
Radomir Banjanac
Aleksandra Kolarski

A&M DATA

IV Meeting on Astrophysical Spectroscopy - A&M DATA - Atmosphere



The photo collage: IV Meeting on Astrophysical Spectroscopy: A&M DATA - Atmosphere

LIST OF PARTICIPANTS

Abu El Maati, Lamia	Department of Physics, Faculty of Science, Benha University, Benha, 13513, Egypt
Ahmad, Mahmoud	Physics Department, College of Science in Zulfi, Majmaah University, 11952, Saudi Arabia
Alwadii, Najah	Department of Physics, College of Sciences, King Khalid University, Saudi Arabia
Banjanac, Radomir	University of Belgrade, IPB, Pregrevica 118, 11080 Belgrade, Serbia
Barović, Jelena	University of Montenegro, Podgorica, Montenegro
Ben Nessib, Nabil	Department of Physics and Astronomy, College of Sciences, King Saud University, Saudi Arabia
Bezuglov, Nikolai	Institute of Atomic Physics and Spectroscopy, University of Latvia, Riga, Latvia
Blanco, Francisco	Facultad de Ciencias Físicas, Universidad Complutense, Avda. Complutense s/n, Madrid, Spain
Bošnjaković, Danko	University of Belgrade, IPB, Pregrevica 118, 11080 Belgrade, Serbia
Brajović, Ljiljana M.	University of Belgrade, Faculty of Civil engineering, Bul. kralja Aleksandra 73, 11120 Belgrade, Serbia
Čadež, Vladimir	Astronomical Observatory, Volgina 7, 11060 Belgrade, Serbia
Christova, Magdalena D.	Department of Applied Physics, Technical University Sofia, 1000 Sofia, Bulgaria
Cvetanović, Nikola	Faculty of Transport and Traffic Engineering, 11000 Belgrade, Serbia
Delibašić Marković, Hristina	Faculty of Science, University of Kragujevac, Radoja Domanovića 12, 34000 Kragujevac, Serbia
Dimitrijević, Milan S.	LERMA, Observatoire de Paris, Université PSL, CNRS, Sorbonne Université, 92190 Meudon, France
Djurović, Stevica	University of Novi Sad, Faculty of Sciences, Department of Physics, 21000 Novi Sad, Serbia
Dragić, Aleksandar	University of Belgrade, IPB, Pregrevica 118, 11080 Belgrade, Serbia
Dujko, Saša	Institute of Physics Belgrade, University of Belgrade, Pregrevica 118, 11080 Belgrade, Serbia
Gajo, Teodora	University of Novi Sad, Faculty of Sciences, Department of Physics, 21000 Novi Sad, Serbia
Garcia, Gustavo	Instituto de Matemáticas y Física Fundamental, Consejo Superior de Investigaciones Científicas, Serrano 121, 28006 Madrid, Spain

Grujić, Zoran D.	University of Belgrade, IPB, Pregrevica 118, 11080 Belgrade, Serbia
Ignjatović, Ljubinko	University of Belgrade, IPB, Pregrevica 118, 11080 Belgrade, Serbia
Ilić, Luka	Barcelona Supercomputing Center, Barcelona, Spain
Ivanović, Stefan	University of Belgrade, IPB, Pregrevica 118, 11080 Belgrade, Serbia
Ivković, Milivoje	University of Belgrade, IPB, Pregrevica 118, 11080 Belgrade, Serbia
Jevremović, Darko	Astronomical Observatory, Volgina 7, 11060 Belgrade 38, Serbia
Joković, Dejan	University of Belgrade, IPB, Pregrevica 118, 11080 Belgrade, Serbia
Jovanović, Gordana	University of Montenegro, Podgorica, Montenegro
Klyucharev, Andrey	Saint Petersburg State University, 7/9 Universitet-skaya nab., St. Petersburg, 199034, Russia
Knežević, David	University of Belgrade, IPB, Pregrevica 118, 11080 Belgrade, Serbia
Kolarski, Aleksandra	University of Belgrade, IPB, Pregrevica 118, 11080 Belgrade, Serbia
Kounchev, Ognyan	Institute of Mathematics and Informatics, Bulgarian Academy of Sciences, Sofia, Bulgaria
Kovačević, Aleksander	University of Belgrade, IPB, Pregrevica 118, 11080 Belgrade, Serbia
Kuzmanoski, Maja	University of Belgrade, IPB, Pregrevica 118, 11080 Belgrade, Serbia
Mahmoud, I. S.	Physics Department, Faculty of Science, Suez Canal University, Ismailia, Egypt.
Majlinger, Zlatko	University of Zagreb, Faculty of Science (PMF), Croatia
Maletić, Dimitrije	University of Belgrade, IPB, Pregrevica 118, 11080 Belgrade, Serbia
Malinović Slavica	Milićević, Geographical Institute Jovan Cvijić, Serbian Academy of Sciences and Arts, Djure Jakšića 9, 11000 Belgrade, Serbia
Maljković, Jelena B.	University of Belgrade, IPB, Pregrevica 118, 11080 Belgrade, Serbia
Malović, Miodrag	University of Belgrade, Innovation center of Faculty of Technology and Metallurgy, Karnegijeva 4, 11120 Belgrade, Serbia
Marinković, Bratislav P.	University of Belgrade, IPB, Pregrevica 118, 11080 Belgrade, Serbia
Mijatović, Zoran	University of Novi Sad, Faculty of Sciences, Department of Physics, 21000 Novi Sad, Serbia

Mijić, Zoran R.	University of Belgrade, IPB, Pregrevica 118, 11080 Belgrade, Serbia
Milovanović, Nenad	Astronomical Observatory, Volgina 7, 11060 Belgrade, Serbia
Ničković, Slobodan	Republic Hydrometeorological Service of Serbia (RHMS), Belgrade, Serbia
Nikitović, Željka D.	University of Belgrade, IPB, Pregrevica 118, 11080 Belgrade, Serbia
Nina, Aleksandra	University of Belgrade, IPB, Pregrevica 118, 11080 Belgrade, Serbia
Obradović, Bratislav M.	University of Belgrade, Faculty of Physics, 11001 Belgrade, Serbia
Odalović, Oleg R.	Faculty of Civil Engineering, University of Belgrade, Bulevar kralja Aleksandra 73, 11000 Belgrade, Serbia
Pešić, Zoran	Thermo Fisher Scientific Inc., West Sussex, RH191UB, United Kingdom
Petković, Dušan S.	Faculty of Civil Engineering, University of Belgrade, Bulevar kralja Aleksandra 73, 11000 Belgrade, Serbia
Petrović, Ivan D.	Technical Collage of Professional Studies Šumadia, Department in Kragujevac, Serbia
Petrović, Violeta M.	Faculty of Science, University of Kragujevac, Radoja Domanovića 12, 34000 Kragujevac, Serbia
Petrović, Zoran Lj.	Serbian Academy of Sciences and Arts, Knez Mihailova 35, 11001 Belgrade, Serbia
Popović, Luka Č.	Astronomical Observatory, Volgina 7, 11060 Belgrade, Serbia
Rabasović, Maja S.	University of Belgrade, IPB, Pregrevica 118, 11080 Belgrade, Serbia
Radovanović, Milan	South Ural State University, Institute of Sports, Tourism and Service, Sony Krivoy street 60, 454080 Chelyabinsk, Russia
Raspopović, Zoran M.	University of Belgrade, IPB, Pregrevica 118, 11080 Belgrade, Serbia
Sahal-Bréchet, Sylvie	LERMA, Observatoire de Paris, Sorbonne Universit, Universit PSL, CNRS, F92190, Meudon, France
Sakan, Nenad M.	University of Belgrade, IPB, Pregrevica 118, 11080 Belgrade, Serbia
Savić, Igor	University of Novi Sad, Faculty of Sciences, Department of Physics, 21000 Novi Sad, Serbia
Savić, Mihailo	University of Belgrade, IPB, Pregrevica 118, 11080 Belgrade, Serbia
Šević, Dragutin	University of Belgrade, IPB, Pregrevica 118, 11080 Belgrade, Serbia

Simić, Zoran	Astronomical Observatory, Volgina 7, 11060 Belgrade, Serbia
Simonović, Ilija	University of Belgrade, IPB, Pregrevica 118, 11080 Belgrade, Serbia
Srećković, Vladimir A.	University of Belgrade, IPB, Pregrevica 118, 11080 Belgrade, Serbia
Tawfik, Sahar G.	Department of Physics, College of Science, Princess Nourah Bint Abdulrahman University, P.O. Box 84428, Riyadh 11671, Saudi Arabia
Topić, Saša	University of Belgrade, IPB, Pregrevica 118, 11080 Belgrade, Serbia
Tošić, Sanja D.	University of Belgrade, IPB, Pregrevica 118, 11080 Belgrade, Serbia
Traparić, Ivan	University of Belgrade, IPB, Pregrevica 118, 11080 Belgrade, Serbia
Udovičić, Vladimir	University of Belgrade, IPB, Pregrevica 118, 11080 Belgrade, Serbia
Vasiljević, Darko	University of Belgrade, IPB, Pregrevica 118, 11080 Belgrade, Serbia
Veselinović, Nikola	University of Belgrade, IPB, Pregrevica 118, 11080 Belgrade, Serbia
Vujčić, Veljko	Astronomical Observatory, Volgina 7, 11060 Belgrade, Serbia
Vukalović, Jelena	Faculty of Science, University of Banja Luka, Mladena Stojanovi ć a 2, 78000 Banja Luka, Republic of Srpska, Bosnia and Herzegovina

PREFACE

This Special Issue on Astrophysical Spectroscopy: A&M DATA - Atmosphere contains papers which were presented at the IV Meeting on Astrophysical Spectroscopy: A&M DATA - Atmosphere. The conference took place at the village called Andrevlje at the foothill of the scenic Fruška Gora mountain, in the northern Serbia from May 30 to June 2, 2022. This conference is unique in that it brings together astronomers and physicists from Serbia and other countries to review the current state of research with the goal of improving our knowledge in this field and better understanding the importance of spectroscopy for future astrophysical investigations. Spectroscopy is considered to be an important tool for the study of plasmas in various fields: astronomy, fusion research, atmospheric research, applied physics and industry. Reliable atomic data from well verified sources are crucial for proper theoretical analysis, spectra synthesis and modelling of both laboratory and astrophysical radiation sources. For instance, for the modeling of stellar atmospheres and opacity calculations a large amount of atomic data is needed, since the chemical composition of stellar atmosphere is not known a priori. Consequently, astroinformatics and development of atomic data databases are important for stellar spectroscopy. Similarly, investigation of laboratory plasma via emission spectroscopy requires the knowledge of atomic and molecular constants, line widths etc. For all these purposes, the A&M Data meeting strives to make the connection between researches that provide the data, those that create and maintain databases, and the data users, both in theory and experiment. The program was divided into several sessions (special mini-projects) dedicated to spectroscopy and data in laboratory and general plasma. The IV Meeting on Astrophysical Spectroscopy was attended by 75 participants from 14 countries. They presented 17 invited talks, and 22 posters. In this Special Issue there are 12 papers. The organizers are grateful to the Ministry of Education, Science and Technological Development of the Republic of Serbia for general support. We thank the members of the scientific and local organizing committees for their help in preparing and running this conference. Finally, we owe an enormous thank you to all the referees for their hard work in peer-reviewing all contributions. Note here that all materials (programme, talks, presentations, photos, etc.) from this and previous meetings are available at <http://asspectro2022.ipb.ac.rs/>

V. A. Srećković, M. S. Dimitrijević & N. Cvetanović
the editors

On the similarities of Stark broadening parameters within a Fe XXV multiplet

M.S. Dimitrijević^{1,2}, M.D. Christova³ and S. Sahal-Bréchet²

¹ *Astronomical Observatory, Volgina 7, 11060 Belgrade, Serbia (E-mail: mdimitrijevic@aob.rs)*

² *Sorbonne Université, Observatoire de Paris, Université PSL, CNRS, LERMA, F-92190, Meudon, France*

³ *Department of Applied Physics, Technical University of Sofia, 1000 Sofia, Bulgaria*

Received: July 23, 2022; Accepted: October 8, 2022

Abstract. Stark broadening parameters, line widths and shifts, have been calculated for spectral lines within Fe XXV $3s^2S_J-3p^2P_J^o$ multiplet, by using the impact semiclassical perturbation theory. The obtained results have been used to demonstrate, that in spite of big differences of line width values expressed as usual in Å, they are practically the same when expressed in angular frequency units. This confirms that in the case of Fe XXV spectral lines we can use the known Stark broadening parameters, expressed in angular frequency units, to obtain the unknown ones, for other lines in the same multiplet. The obtained data are particularly interesting for neutron star atmospheres and environment investigation and modelling as well as for inertial fusion plasma.

Key words: Stark broadening – Fe XXV – spectral lines – line profiles

1. Introduction

Stark broadening parameters, spectral line widths and shifts originating from fluctuating electric microfields created by surrounding charged particles, are of interest for different problems in astrophysics (see for example [Beauchamp et al., 1997](#); [Popović et al., 2001](#); [Dimitrijević & Sahal-Bréchet, 2014](#); [Dimitrijević & Christova, 2021](#); [Dimitrijević et al., 2021](#)), laboratory, ([Konjević, 1999](#); [Blagojević et al., 1999](#); [Torres et al., 2006](#)), fusion ([Griem, 1992](#); [Iglesias et al., 1997](#)), laser produced plasma research ([Gornushkin et al., 1999](#); [Nicolosi et al., 1978](#); [Sorge et al., 2000](#)), different plasmas in technology ([Yilbas et al., 2015](#); [Hoffman et al., 2006](#); [Dimitrijević & Sahal-Bréchet, 2014](#); [Dimitrijević et al., 2021](#)), as well as laser design and development ([Wang et al., 1992](#); [Csillag & Dimitrijević, 2004](#); [Dimitrijević & Sahal-Bréchet, 2014](#)).

Stark broadening data are of interest for a number of astrophysical problems, as for example radiative transfer calculations, abundance determinations and investigation, stellar spectra analysis, modelling and synthesis, and other research

fields (see for example [Dimitrijević & Christova, 2021](#)). In white dwarf atmospheres, plasma conditions are favorable for Stark broadening, and there, it is usually the principal pressure broadening mechanism. For example, the influence of Stark broadening has been investigated in atmospheres of DO ([Dimitrijević et al., 2016, 2018](#); [Dimitrijević & Chougule, 2018](#); [Dimitrijević et al., 2021](#)), DB ([Majlinger et al., 2017, 2018, 2020](#); [Dimitrijević et al., 2021](#)), DA ([Majlinger et al., 2017, 2020](#)) dwarfs and in B subdwarfs ([Hamdi et al., 2017](#); [Chougule et al., 2020](#)). It should be noted that such data may be also of interest in the case of A and late B type stars ([Majlinger et al., 2017, 2020](#)).

Another class of celestial objects where Stark broadening is of interest, are neutron stars (see for example [Madej, 1989](#); [Paerels, 1997](#); [Majczyna et al., 2005](#); [Suleimanov et al., 2014](#)) and their environments ([van Peet et al., 2009](#)). We note as well that exist attempts to create neutron star plasma conditions in laboratory ([Moon et al., 2005](#)) and that for diagnostic of such plasma, Stark broadening data for Fe XXV spectral lines may be also of interest. For modelling and investigation of their atmospheres, highly ionized iron lines are important. They are observed in neutron star spectra, as e.g. by [Cottam et al. \(2002\)](#), who found a Fe XXV feature ($n = 2-3$ transition) in X-ray burst spectra of EXO 0748676. We note as well that [Werner et al. \(2007\)](#) performed spectrum synthesis of neutron star atmospheres with iron lines from Fe XVII up to Fe XXVII.

Our objective here is to examine Stark broadening parameters for particular lines within the multiplet Fe XXV $3s^2S_J - 3p^2P_{J'}$, of interest for neutron stars and their environments, in order to investigate their similarities. We want to check, if from values for one line, one could estimate Stark broadening parameters for other lines in Fe XXV multiplets, in spite of eventual differences between Stark broadening parameters.

2. Theory

For the calculations of Stark broadening parameters of helium-like Fe XXV spectral lines, the impact semiclassical perturbation theory ([Sahal-Bréchet, 1969a,b](#); [Sahal-Bréchet, Dimitrijević, & Ben Nessib, 2014](#)) has been employed. This theoretical method has been described in detail in above mentioned references, and only basic formulas will be given here. According to the semiclassical theory, the emitter is treated as quantum system and perturbers are examined as classical particles. The full width at half maximum (FWHM - W) and shift (d) of an isolated spectral line are given in the case of non-hydrogenic ions as:

$$W = N \int v f(v) dv \left(\sum_{i' \neq i} \sigma_{ii'}(v) + \sum_{f' \neq f} \sigma_{ff'}(v) + \sigma_{el} \right)$$

$$d = N \int v f(v) dv \int_{R_3}^{R_D} 2\pi \rho d\rho \sin(2\varphi_p). \quad (1)$$

where i and f denote the initial and final level of the corresponding transition; i' and f' are perturbing levels; N perturber density; v perturber velocity, and $f(v)$ is the Maxwellian distribution of electron velocities. The inelastic cross sections $\sigma_{kk'}(v)$, $k = i, f$ are presented here by an integration of the transition probability $P_{kk'}(\rho, v)$, over the impact parameter ρ as:

$$\sum_{k' \neq k} \sigma_{kk'}(v) = \frac{1}{2} \pi R_1^2 + \int_{R_1}^{R_D} 2\pi \rho d\rho \sum_{k' \neq k} P_{kk'}(\rho, v). \quad (2)$$

The cross section for elastic collisions is given as:

$$\sigma_{el} = 2\pi R_2^2 + \int_{R_2}^{R_D} 2\pi \rho d\rho \sin^2 \delta + \sigma_r, \quad (3)$$

$$\delta = (\varphi_p^2 + \varphi_q^2)^{\frac{1}{2}}.$$

Here, δ denotes the phase shift with components φ_p (r^{-4}) and φ_q (r^{-3}), describing contributions due to polarization and quadrupole potentials, respectively. The method of symmetrization and calculation of cut-off parameters R_1 , R_2 , R_3 , and the Debye cut-off R_D is explained in [Sahal-Br  chot \(1969b\)](#). The calculation of the contribution of Feshbach resonances (σ_r), is explained in detail in [Fleurier et al. \(1977\)](#) and [Sahal-Br  chot \(2021\)](#).

3. Results and discussion

For calculations of Stark broadening parameters, full width at half intensity maximum (FWHM - W) and shift (d) we used the semiclassical perturbation theory ([Sahal-Br  chot, 1969a,b](#); [Sahal-Br  chot, Dimitrijevi  , & Ben Nessib, 2014](#)). The electron density is 10^{17} cm^{-3} and temperatures 300 000 K, 500 000 K, 1 000 000 K, 5 000 000 K, 10 000 000 K, and 20 000 000 K. The needed set of atomic energy levels for Fe XXV, have been taken from [Sugar & Corliss \(1985\)](#), [Shirai et al. \(2000\)](#) and [Kramida et al. \(2021\)](#). Oscillator strengths have been calculated employing [Bates & Damgaard \(1949\)](#) approach, the tables of [Oertel & Shomo \(1968\)](#) and the method of [van Regemorter et al. \(1979\)](#) for higher levels, in the cases when the approach of [Bates & Damgaard \(1949\)](#) is not suitable.

The results, for Stark Full Width at Half intensity Maximum (FWHM) and shift for three lines within the Fe XXV $3s^2S_J - 3p^2P_{J'}^o$ multiplet broadened with collisions with electrons are presented in Table 1.

The wavelengths are calculated from atomic energy levels, so that they may be different from observed. If the correction of this difference is needed, we can do this for the width and similarly for the shift as:

$$W_1 = \left(\frac{\lambda_1}{\lambda} \right)^2 W. \quad (4)$$

Here, W_1 is the corrected width, λ_1 is the experimental, λ the calculated wavelength and W the width in Å from Table 1 in this paper.

The quantity C (Dimitrijević & Sahal-Bréchet, 1984) gives the maximal perturber density for which the line may be considered as isolated, when it is divided by the corresponding width (W).

In the obtained results we found that the largest Stark width value, expressed as usual in Å, for particular spectral lines within the investigated multiplet, is up to 2.6 times bigger from the smallest one. In the case of the shift, the biggest value is up to 3.0 times larger from the smallest. On the other hand, Wiese and Konjević (1982; 1992) examined regularities and similarities in experimental results for Stark widths and shifts and found that line widths in angular frequency units in multiplets usually agree within a few per cent and shifts within $\pm 10\%$. These findings were very useful to estimate unknown Stark broadening parameters of a line within a multiplet, if we have data for another line within the same multiplet, as well as to critically estimate the published results or results obtained during experiments or calculations. For this reason, in Table 1 are parallelly given and results in angular frequency units.

We can transform Stark width in Å in angular frequency units by the expression:

$$W(\text{Å}) = \frac{\lambda^2}{2\pi c} W(s^{-1}) \quad (5)$$

where c is the speed of light.

One can see from Table 1, that for Stark widths, for all considered temperatures, the largest width is 2.6 times larger than the smallest one. For shift this ratio depends on temperature. For $T = 300\,000$ K, $500\,000$ K, $1\,000\,000$ K, $5\,000\,000$ K, $10\,000\,000$ K and $20\,000\,000$ K, the greatest Stark shift is 2.8, 3.0, 3.0, 2.9, 2.8, and 2.8 times greater from the smallest one respectively. However, if we look at differences of Stark broadening parameters expressed in angular frequency units, the largest Stark width is only 0.065% larger than the smallest one, so that they are practically identical. This is even better than the prediction of Wiese and Konjević (1982; 1992). On the other hand in the case of the Stark shift small differences exist and they are dependent on temperature. So, in the case of the Stark shift, the largest Stark shift is 6.1%, 13.8%, 15.0%, 12.0%, 5.6% and 5.5% larger than the smallest one, for $T = 300\,000$ K, $500\,000$ K, $1\,000\,000$ K, $5\,000\,000$ K, $10\,000\,000$ K and $20\,000\,000$ K, respectively. For some temperatures the difference is a little bit larger than the prediction of 10%

Table 1. This table gives electron-impact broadening parameters for Fe XXV lines, Stark FWHM W and shift d , expressed in Å and in angular frequency units. Calculated wavelength of the transitions (in Å) and parameter C are also given. This parameter, when divided with the corresponding Stark width, gives an estimate for the maximal perturber density for which the line may be treated as isolated. Results are for electron density of 10^{17} cm $^{-3}$ and temperatures are from 300 000 K to 20 000 000 K. A positive shift is towards the red part of the spectrum.

TRANSITION	T[10 ⁵ K]	W[Å]	d[Å]	W[10 ¹² s ⁻¹]	d[10 ¹² s ⁻¹]
3s ³ S ₁ -3p ³ P ₀ ^o	3.	1.98	-0.0422.	15.5	-0.330
1552.8 Å	5.	1.55	-0.0179	12.1	-0.140
C = 1.6 10 ²³	10.	0.592	-0.0157	8.75	-0.123
	50.	0.548	-0.0143	4.28	-0.112
	100.	0.410	-0.0126	3.20	-0.0984
	200.	0.311	-0.0101	2.43	-0.0789
3s ³ S ₁ -3p ³ P ₁ ^o	3.	1.72	-0.0363	15.4	-0.326
1449.3 Å	5.	1.35	-0.0154	12.1	-0.138
C = 1.4 10 ²³	10.	0.976	-0.0133	8.75	-0.119
	50.	0.478	-0.0123	4.29	-0.110
	100.	0.358	-0.0109	3.21	-0.0977
	200.	0.271	-0.00872	2.43	-0.0782
3s ³ S ₁ -3p ³ P ₂ ^o	3.	0.754	-0.0151	15.5	-0.311
956.0 Å	5.	0.591	-0.00599	12.3	-0.123
C = 0.31 10 ²³	10.	0.427	-0.00518	8.80	-0.107
	50.	0.210	-0.00487	4.33	-0.100
	100.	0.157	-0.00452	3.24	-0.0932
	200.	0.119	-0.00363	2.45	-0.0748

of Wiese and Konjević (1982; 1992). One can see that in spite of differences of Stark broadening parameters within the multiplet, expressed in Å we can use these parameters in angular frequency units to obtain the unknown value within the considered multiplet from the known one. For this purpose one can use Eq. 7, where W and λ are FWHM and wavelength of the known Stark width and W_1 and λ_1 of the unknown one. For the shift the corresponding equation is analogous. This can be used to estimate the unknown Stark broadening parameters within a multiplet of Fe XXV from the known ones.

4. Conclusion and future perspectives

The Stark broadening parameters, FWHM and shifts, have been calculated for three lines within the Fe XXV 3s²S _{J} -3p²P _{J'} ^o _{J'} multiplet, by using the impact semi-

classical perturbation theory. (Sahal-Bréchet, 1969a,b; Sahal-Bréchet, Dimitrijević, & Ben Nessib, 2014). The obtained results have been used to demonstrate that, in spite of differences between Stark broadening parameters expressed in Å, when expressed in angular frequency units, we can use the known Stark broadening parameters to obtain the unknown ones, for other lines in the considered multiplet. The obtained Stark broadening parameters will also be implemented in STARK-B database (<http://stark-b.obspm.fr/> - Sahal-Bréchet et al. (2015)), which is included in Virtual Atomic and Molecular Data Center (VAMDC) (<http://www.vamdc.org/> - Dubernet et al. (2010, 2016); Albert et al. (2020)).

The obtained data are particularly interesting for neutron star atmospheres and environment investigation and modelling as well as for inertial fusion plasma.

Acknowledgements. This work has been supported with a STSM visit grant for M.S.D. within the framework of COST Action CA 18104 "Revealing the Milky Way with GAIA".

The authors would like to thank to Research and Development Sector at the Technical University of Sofia for the financial support covering the conference fee for M.D.C.

References

- Albert, D., Antony, B. K., Ba, Y. A., et al., A Decade with VAMDC: Results and Ambitions. 2020, *Atoms*, **8**, 76, DOI: 10.3390/atoms8040076
- Bates, D. R. & Damgaard, A., The Calculation of the Absolute Strengths of Spectral Lines. 1949, *Philosophical Transactions of the Royal Society of London Series A*, **242**, 101, DOI: 10.1098/rsta.1949.0006
- Beauchamp, A., Wesemael, F., & Bergeron, P., Spectroscopic Studies of DB White Dwarfs: Improved Stark Profiles for Optical Transitions of Neutral Helium. 1997, *Astrophys. J., Suppl. Ser.*, **108**, 559, DOI: 10.1086/312961
- Blagojević, B., Popović, M. V., Konjević, & Dimitrijević, M. S., Stark Broadening Parameters of Analogous Spectral Lines Along the Lithium and Beryllium Isoelectronic Sequences. 1999, *Journal of Quantitative Spectroscopy and Radiative Transfer*, **61**, 361, DOI: 10.1016/S0022-4073(98)00002-8
- Chougule, A., Przybilla, N., Dimitrijević, M. S., & Schaffenroth, V., The impact of improved Stark-broadening widths on the modeling of double-ionized chromium lines in hot stars. 2020, *Contributions of the Astronomical Observatory Skalnaté Pleso*, **50**, 139, DOI: 10.31577/caosp.2020.50.1.139
- Cottam, J., Paerels, F., & Mendez, M., Gravitationally redshifted absorption lines in the X-ray burst spectra of a neutron star. 2002, *Nature*, **420**, 51, DOI: 10.1038/nature01159
- Csillag, L. & Dimitrijević, M. S., On the Stark broadening of the 537.8 nm and 441.6 nm Cd⁺ lines excited in a hollow cathode laser discharge. 2004, *Applied Physics B: Lasers and Optics*, **78**, 221, DOI: 10.1007/s00340-003-1368-3
- Dimitrijević, M. & Chougule, A., Stark Broadening of Cr III Spectral Lines: DO White Dwarfs. 2018, *Atoms*, **6**, 15, DOI: 10.3390/atoms6020015

- Dimitrijević, M. & Sahal-Bréchet, S., On the Application of Stark Broadening Data Determined with a Semiclassical Perturbation Approach. 2014, *Atoms*, **2**, 357, DOI: 10.3390/atoms2030357
- Dimitrijević, M. S. & Christova, M., Stark widths of Lu II spectral lines. 2021, *European Physical Journal D*, **75**, 172, DOI: 10.1140/epjd/s10053-021-00179-4
- Dimitrijević, M. S., Christova, M., Simić, Z., Kovačević, A., & Sahal-Bréchet, S., Stark broadening of B IV spectral lines. 2016, *Monthly Notices of the RAS*, **460**, 1658, DOI: 10.1093/mnras/stw1023
- Dimitrijević, M. S., Christova, M. D., Milovanović, N., & Sahal-Bréchet, S., Stark broadening of Zn II spectral lines. 2021, *Monthly Notices of the RAS*, **507**, 2087, DOI: 10.1093/mnras/stab2299
- Dimitrijević, M. S. & Sahal-Bréchet, S., Stark broadening of neutral helium lines. 1984, *Journal of Quantitative Spectroscopy and Radiative Transfer*, **31**, 301, DOI: 10.1016/0022-4073(84)90092-X
- Dimitrijević, M. S., Simić, Z., Kovačević, A., & Sahal-Bréchet, S., The influence of Stark broadening on Xe VIII spectral lines in DO white dwarfs. 2018, *Astronomical and Astrophysical Transactions*, **30**, 331
- Dubernet, M. L., Antony, B. K., Ba, Y. A., et al., The virtual atomic and molecular data centre (VAMDC) consortium. 2016, *Journal of Physics B Atomic Molecular Physics*, **49**, 074003, DOI: 10.1088/0953-4075/49/7/074003
- Dubernet, M. L., Boudon, V., Culhane, J. L., et al., Virtual atomic and molecular data centre. 2010, *Journal of Quantitative Spectroscopy and Radiative Transfer*, **111**, 2151, DOI: 10.1016/j.jqsrt.2010.05.004
- Fleurier, C., Sahal-Bréchet, S., & Chapelle, J., Stark profiles of some ion lines of alkaline earth elements. 1977, *Journal of Quantitative Spectroscopy and Radiative Transfer*, **17**, 595, DOI: 10.1016/0022-4073(77)90019-X
- Gornushkin, I. B., King, L. A., Smith, B. W., Omenetto, N., & Winefordner, J. D., Line broadening mechanisms in the low pressure laser-induced plasma. 1999, *Spectrochimica Acta*, **54**, 1207, DOI: 10.1016/S0584-8547(99)00064-6
- Griem, H. R., Plasma spectroscopy in inertial confinement fusion and soft x-ray laser research. 1992, *Physics of Fluids B*, **4**, 2346, DOI: 10.1063/1.860205
- Handi, R., Ben Nessib, N., Sahal Bréchet, S., & Dimitrijević, M. S., Stark Widths of Ar II Spectral Lines in the Atmospheres of Subdwarf B Stars. 2017, *Atoms*, **5**, 26, DOI: 10.3390/atoms5030026
- Hoffman, J., Szymański, Z., & Azharonok, V., Plasma Plume Induced During Laser Welding of Magnesium Alloys. 2006, in American Institute of Physics Conference Series, Vol. **812**, *PLASMA-2005 Conference on Research and Application of Plasmas*, ed. M. J. Sadowski, M. Dudek, H.-J. Hartfuss, & E. Pawelec, 469–472
- Iglesias, E., Griem, H., Welch, B., & Weaver, J., UV Line Profiles of Biv from a 10-Ps Krf-Laser-Produced Plasma. 1997, *Astrophysics and Space Science*, **256**, 327

- Konjević, N., Plasma broadening and shifting of non-hydrogenic spectral lines: present status and applications. 1999, *Physics Reports*, **316**, 339, DOI: 10.1016/S0370-1573(98)00132-X
- Kramida, A., Yu. Ralchenko, Reader, J., & and NIST ASD Team. 2021, NIST Atomic Spectra Database (ver. 5.9), [Online]. Available: <https://physics.nist.gov/asd> [2022, September 7]. National Institute of Standards and Technology, Gaithersburg, MD.
- Madej, J., Broadening of iron resonance lines in X-ray burst spectra. 1989, *Astronomy and Astrophysics*, **209**, 226
- Majczyna, A., Madej, J., Joss, P. C., & Różańska, A., Model atmospheres and X-ray spectra of bursting neutron stars. II. Iron rich comptonized spectra. 2005, *Astronomy and Astrophysics*, **430**, 643, DOI: 10.1051/0004-6361:20034048
- Majlinger, Z., Dimitrijevic, M. S., & Simic, Z., On the Stark broadening of Co II spectral lines. 2018, *Astronomical and Astrophysical Transactions*, **30**, 323
- Majlinger, Z., Dimitrijević, M. S., & Srećković, V. A., Stark broadening of Co II spectral lines in hot stars and white dwarf spectra. 2020, *Monthly Notices of the RAS*, **496**, 5584, DOI: 10.1093/mnras/staa1947
- Majlinger, Z., Simić, Z., & Dimitrijević, M. S., Stark broadening of Zr IV spectral lines in the atmospheres of chemically peculiar stars. 2017, *Monthly Notices of the RAS*, **470**, 1911, DOI: 10.1093/mnras/stx1321
- Moon, S. J., Wilks, S. C., Klein, R. I., et al., A Neutron Star Atmosphere in the Laboratory With Petawatt Lasers. 2005, *Astrophysics and Space Science*, **298**, 293, DOI: 10.1007/s10509-005-3949-6
- Nicolosi, P., Garifo, L., Jannitti, E., Malvezzi, A. M., & Tondello, G., Broadening and self-absorption of the resonance lines of H-like light ions in laser-produced plasmas. 1978, *Nuovo Cimento B Serie*, **48**, 133, DOI: 10.1007/BF02743638
- Oertel, G. K. & Shomo, L. P., Tables for the Calculation of Radial Multipole Matrix Elements by the Coulomb Approximation. 1968, *Astrophys. J., Suppl. Ser.*, **16**, 175, DOI: 10.1086/190173
- Paerels, F., Pressure Broadening of Absorption Lines in Neutron Star Atmospheres and Prospects for Measuring Neutron Star Masses and Radii. 1997, *Astrophysical Journal, Letters*, **476**, L47, DOI: 10.1086/310485
- Popović, L. Č., Simić, S., Milovanović, N., & Dimitrijević, M. S., Stark Broadening Effect in Stellar Atmospheres: Nd II Lines. 2001, *Astrophys. J., Suppl. Ser.*, **135**, 109, DOI: 10.1086/321778
- Sahal-Bréchet, S., Impact Theory of the Broadening and Shift of Spectral Lines due to Electrons and Ions in a Plasma. 1969a, *Astronomy and Astrophysics*, **1**, 91
- Sahal-Bréchet, S., Impact Theory of the Broadening and Shift of Spectral Lines due to Electrons and Ions in a Plasma (Continued). 1969b, *Astronomy and Astrophysics*, **2**, 322

- Sahal-Bréchet, S., The Semiclassical Limit of the Gailitis Formula Applied to Electron Impact Broadening of Spectral Lines of Ionized Atoms. 2021, *Atoms*, **9**, 29, DOI: 10.3390/atoms9020029
- Sahal-Bréchet, S., Dimitrijević, M., & Ben Nessib, N., Widths and Shifts of Isolated Lines of Neutral and Ionized Atoms Perturbed by Collisions With Electrons and Ions: An Outline of the Semiclassical Perturbation (SCP) Method and of the Approximations Used for the Calculations. 2014, *Atoms*, **2**, 225, DOI: 10.3390/atoms2020225
- Sahal-Bréchet, S., Dimitrijević, M. S., Moreau, N., & Ben Nessib, N., The STARK-B database VAMDC node: a repository for spectral line broadening and shifts due to collisions with charged particles. 2015, *Physica Scripta*, **90**, 054008, DOI: 10.1088/0031-8949/90/5/054008
- Shirai, T., Sugar, J., Musgrove, A., & Wiese, W. L. 2000, *Spectral Data for Highly Ionized Atoms: Ti, V, Cr, Mn, Fe, Co, Ni, Cu, Kr, and Mo*
- Sorge, S., Wierling, A., Röpke, G., et al., Diagnostics of a laser-induced dense plasma by hydrogen-like carbon spectra. 2000, *Journal of Physics B Atomic Molecular Physics*, **33**, 2983, DOI: 10.1088/0953-4075/33/16/304
- Sugar, J. & Corliss, C. 1985, *Atomic energy levels of the iron-period elements: Potassium through Nickel*
- Suleimanov, V. F., Klochkov, D., Pavlov, G. G., & Werner, K., Carbon Neutron Star Atmospheres. 2014, *Astrophys. J., Suppl. Ser.*, **210**, 13, DOI: 10.1088/0067-0049/210/1/13
- Torres, J., van de Sande, M. J., van der Mullen, J. J. A. M., Gamero, A., & Sola, A., Stark broadening for simultaneous diagnostics of the electron density and temperature in atmospheric microwave discharges. 2006, *Spectrochimica Acta*, **61**, 58, DOI: 10.1016/j.sab.2005.11.002
- van Peet, J. C. A., Costantini, E., Méndez, M., Paerels, F. B. S., & Cottam, J., Properties of the ionised plasma in the vicinity of the neutron-star X-ray binary EXO 0748-676. 2009, *Astronomy and Astrophysics*, **497**, 805, DOI: 10.1051/0004-6361/200811181
- van Regemorter, H., Binh Dy, H., & Prudhomme, M., Radial transition integrals involving low or high effective quantum numbers in the Coulomb approximation. 1979, *Journal of Physics B Atomic Molecular Physics*, **12**, 1053, DOI: 10.1088/0022-3700/12/7/009
- Wang, J. S., Griem, H. R., Huang, Y. W., & Böttcher, F., Measurements of line broadening of B v H α and L δ in a laser-produced plasma. 1992, *Physical Review A: General Physics*, **45**, 4010, DOI: 10.1103/PhysRevA.45.4010
- Werner, K., Nagel, T., Rauch, T., & Suleimanov, V., Non-LTE models for neutron star atmospheres and supernova-fallback disks. 2007, *Adv. Space Res.*, **40**, 1512, DOI: 10.1016/j.asr.2006.12.023
- Wiese, W. L. & Konjević, N., Regularities and similarities in plasma broadened spectral line widths (Stark widths). 1982, *Journal of Quantitative Spectroscopy and Radiative Transfer*, **28**, 185, DOI: 10.1016/0022-4073(82)90022-X

- Wiese, W. L. & Konjevic, N., Regularities in experimental Stark shifts. 1992, *Journal of Quantitative Spectroscopy and Radiative Transfer*, **47**, 185, DOI: 10.1016/0022-4073(92)90028-3
- Yilbas, B. S., Patel, F., & Karatas, C., Laser controlled melting of H12 hot-work tool steel with B₄C particles at the surface. 2015, *Optics Laser Technology*, **74**, 36, DOI: 10.1016/j.optlastec.2015.05.012

Stark broadening of Si II spectral lines: comparison with experimental results

M.S. Dimitrijević^{1,2}, M.D. Christova³ and S. Sahal-Bréchet²

¹ *Astronomical Observatory, Volgina 7, 11060 Belgrade, Serbia (E-mail: mdimitrijevic@aob.rs)*

² *Sorbonne Université, Observatoire de Paris, Université PSL, CNRS, LERMA, F-92190, Meudon, France*

³ *Department of Applied Physics, Technical University of Sofia, 1000 Sofia, Bulgaria*

Received: August 20, 2022; Accepted: October 5, 2022

Abstract. Our calculations for Stark broadening parameters of Si II spectral lines obtained using impact semiclassical perturbation theory are compared with experimental data from the literature. Presented data are needed for the evaluation of the physical conditions of stellar plasma, siliciabundance determination, opacity calculations, stellar spectra analysis and synthesis, stellar atmosphere modelling etc.

Key words: Stark broadening – Si II – spectral lines

1. Introduction

Large cosmic abundance of silicon determines the great interest to its spectra for astrophysical and cosmological studies. From another side, it is a principal impurity chemical element in laboratory plasma and nuclear fusion, and its lines are suitable for spectroscopic diagnostics. For the evaluation of the physical conditions of stellar plasma, opacity calculations, etc. reliable data for silicon are necessary.

Silicon is one of the most experimentally investigated emitter after hydrogen, helium, and argon (see e.g. critical reviews of [Konjević & Wiese 1990](#) and [Lesage 2009](#)). We note that the authors of NIST critical review for measured Stark broadening parameters of spectral lines, [Konjević & Wiese \(1990\)](#), report a large scatter in the results for Si II lines from different papers.

Spectral analysis and interpretation of electromagnetic radiation ensure valuable information about our Universe. Various cosmic light sources also contain silicon atoms and ions as emitters ([Peytremann, 1972](#)). Thus, the ionized silicon spectral lines play an important role in the plasma diagnostics within a wide range of plasma conditions in many fields of astrophysics, technology and environmental protection. Singly ionized silicon spectral lines are discovered in the emission and absorption spectra in various cosmic light sources. We mention

here suitable papers emphasizing the importance of Si II lines in various fields of astrophysical plasma diagnostics. Ionized silicon lines are used for solar photosphere study in [Shi et al. \(2008\)](#). Using width of Si II lines, the diversity of supernovae Ia is determined in [Arsenijević et al. \(2008\)](#). Emission spectra of the first helium nova V445 Puppis ([Iijima & Nakanishi, 2008](#)) present prominent Si II lines. In atmospheres of A, B and O type stars, and white dwarfs, many singly charged ion lines are observed ([Peytremann, 1972](#)). The observations indicate strong visible and ultraviolet lines of ionized silicon in the spectrum of stars from type A 0 to B 3. It is known that silicon is significant in solar and stellar research. These lines provide valuable information for silicon abundance, for silicon absorption in the hot stars ([Lanz et al. 1988](#) and references therein). With the development of space born astronomy, less intensive lines become accessible. Such lines, which originated from high energy levels, are sensitive to the plasma broadening mechanisms. According to [Lanz et al. \(1988\)](#), many spectra of Ap Si stars reveal such lines. Their results show that Stark broadening mechanism is a dominant one for higher transitions.

Recently, we calculated Stark width of 13 Si II multiplets for temperatures from 5000 K up to 80 000 K, and for perturber density of 10^{17} cm^{-3} using the MSE - modified semiempirical method ([Dimitrijević & Konjević, 1980](#); [Dimitrijević & Kršljanin, 1986](#)) and Stark widths and shifts for 62 Si II multiplets, for collisions with electrons, protons and ionized helium, for a grid of temperatures and perturber densities ($10^{14} - 10^{20} \text{ cm}^{-3}$). Semiclassical perturbation theory ([Sahal-Bréchet, 1969a,b](#); [Sahal-Bréchet, Dimitrijević, & Ben Nessib, 2014](#)) has been used for calculations. The obtained results will be published elsewhere and here they have been used for comparison with available experimental data.

2. Theory

Broadening of spectral lines in a plasma is provoked by the interactions between emitting particles (atoms/ions) and environments (electrons, protons, atoms, ions, molecules). It is known in the literature as pressure broadening. Stark broadening of spectral lines arises due to interactions with electrically charged particles as electrons, protons, and ions. There are several theories applicable to this type of pressure broadening, depending on the plasma conditions. The data used for comparison with experimental data in this article have been calculated by applying the impact semiclassical perturbation theory ([Sahal-Bréchet, 1969a,b](#); [Sahal-Bréchet, Dimitrijević, & Ben Nessib, 2014](#)). For better understanding how data for comparison have been obtained, we give here briefly the basics of the theory. According to the semiclassical theory, the emitter is treated as quantum system and perturbers are examined as classical particles. The full width at half maximum (FWHM) and shift of an isolated spectral line are given by the expressions:

$$W = N \int v f(v) dv \left(\sum_{i' \neq i} \sigma_{ii'}(v) + \sum_{f' \neq f} \sigma_{ff'}(v) + \sigma_{el} \right)$$

$$d = N \int v f(v) dv \int_{R_3}^{R_D} 2\pi \rho d\rho \sin(2\varphi_p). \quad (1)$$

where i and f denote the initial and final level of the corresponding transition; i' and f' are perturbing levels; N perturber density; v perturber velocity, and $f(v)$ is the Maxwellian distribution of electron velocities. The cross sections $\sigma_{kk'}(v)$, $k = i, f$, concern inelastic interactions. It is presented here by an integration of the transition probability $P_{kk'}(\rho, v)$, over the impact parameter ρ as:

$$\sum_{k' \neq k} \sigma_{kk'}(v) = \frac{1}{2} \pi R_1^2 + \int_{R_1}^{R_D} 2\pi \rho d\rho \sum_{k' \neq k} P_{kk'}(\rho, v). \quad (2)$$

The cross section of elastic collisions between emitting atoms (ions) and charged particles could be estimated by:

$$\sigma_{el} = 2\pi R_2^2 + \int_{R_2}^{R_D} 2\pi \rho d\rho \sin^2 \delta + \sigma_r, \quad (3)$$

$$\delta = (\varphi_p^2 + \varphi_q^2)^{\frac{1}{2}}.$$

Here, δ gives the phase shift which components φ_p (r^{-4}) and φ_q (r^{-3}), describe emitter-perturber elastic interactions via polarization and quadrupole potentials. Explanation of the symmetrization and procedure for cut-off parameters R_1 , R_2 , R_3 , and the Debye cut-off R_D could be found in [Sahal-Br echot \(1969b\)](#). Feshbach resonances, taken into account by the third term σ_r , could be found in [Fleurier \(1977\)](#).

3. Results and discussion

In this paper, we compare our new calculations for Stark broadening width and shift of singly ionized silicon lines, using the semiclassical perturbation theory ([Sahal-Br echot, 1969a,b](#); [Sahal-Br echot, Dimitrijevi c, & Ben Nessib, 2014](#)), with measured ones. Comparatively with other chemical elements, there are many experimental data for Stark broadening of neutral and ionized silicon lines. In the next figures we present such comparison for four spectral lines which are studied in the experimental investigations, prominent in the observed spectra of

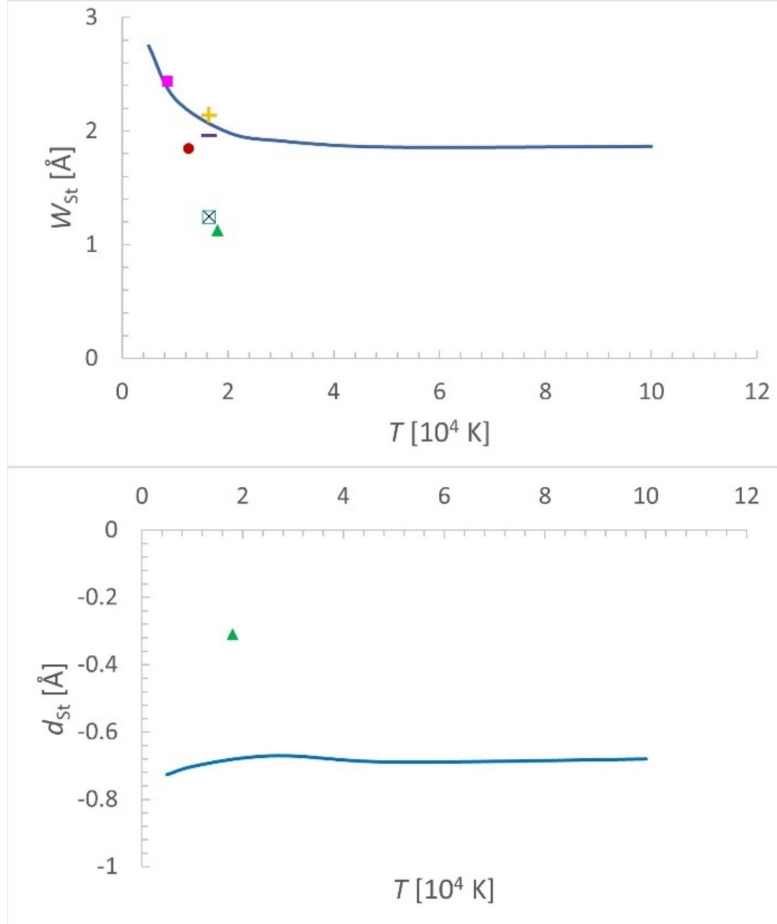


Figure 1. Comparison of the calculated temperature dependence (solid line) of Stark width (up) and shift (down) with experimental results from the literature for spectral line Si II $3s^2 4s \ ^2S_{1/2} - 3s^2 4p \ ^2P_{3/2}^o$ with $\lambda = 6356.9 \text{ \AA}$. The perturber density is $1.10^{17} \text{ cm}^{-3}$. Symbols illustrate results from: Konjević et al. (1970) (solid square); Lesage et al. (1977) (dash); Chiang & Griem (1978) (plus); Lesage et al. (1983) (open square); Pérez et al. (1993) (cross); González et al. (2002) (solid triangle) and Bukvić et al. (2008) (solid circle).

astrophysical objects and suitable for plasma diagnostics. The perturber density is 10^{17} cm^{-3} . One of the most measured spectral lines is Si II $3s^2 4s \ ^2S_{1/2} - 3s^2 4p \ ^2P_{3/2}^o$ with $\lambda = 6356.9 \text{ \AA}$. The reported scattering of experimental Stark width values in the publications that is noticed by Konjević & Wiese (1990), is well observable in Fig. 1 (upper part). Measurements are grouped in two parts, four widths (Konjević et al., 1970; Lesage et al., 1977; Chiang & Griem, 1978; Bukvić

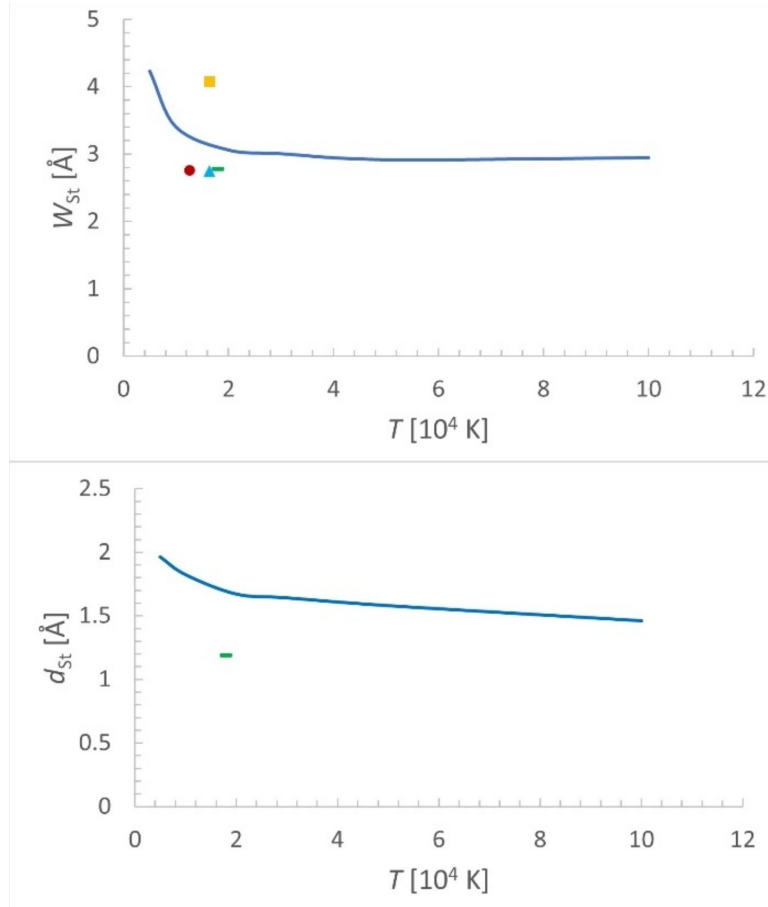


Figure 2. Comparison of the calculated temperature dependence (solid line) of Stark width (up) and shift (down) with experimental results from the literature for spectral line Si II $3s^2 4p \ ^2P_{3/2}^o - 3s^2 5s \ ^2S_{1/2}$ with $\lambda = 5973.4 \text{ \AA}$. The perturber density is $1.10^{17} \text{ cm}^{-3}$. Symbols illustrate results from: Kusch & Schroeder (1982) (solid square); Lesage et al. (1983) (solid triangle); González et al. (2002) (dash) and Bukvić et al. (2008) (solid circle).

et al., 2008) are close to the calculated curve and other three (Lesage et al., 1983; Pérez et al., 1993; González et al., 2002) are around two times smaller. All they fall within the temperature interval where the Stark width decreases noticeably with the temperature. There is one reference (González et al., 2002) that we found in the literature concerning shift measurements. For the first examined line both, measured and calculated values are negative. The measured value in Fig. 1 (lower part) is approximately twice lower than calculated.

Fig. 2 illustrates results for spectral line $\lambda = 5973.4 \text{ \AA}$, Si II $3s^2 4p \ ^2P_{3/2}^o -$

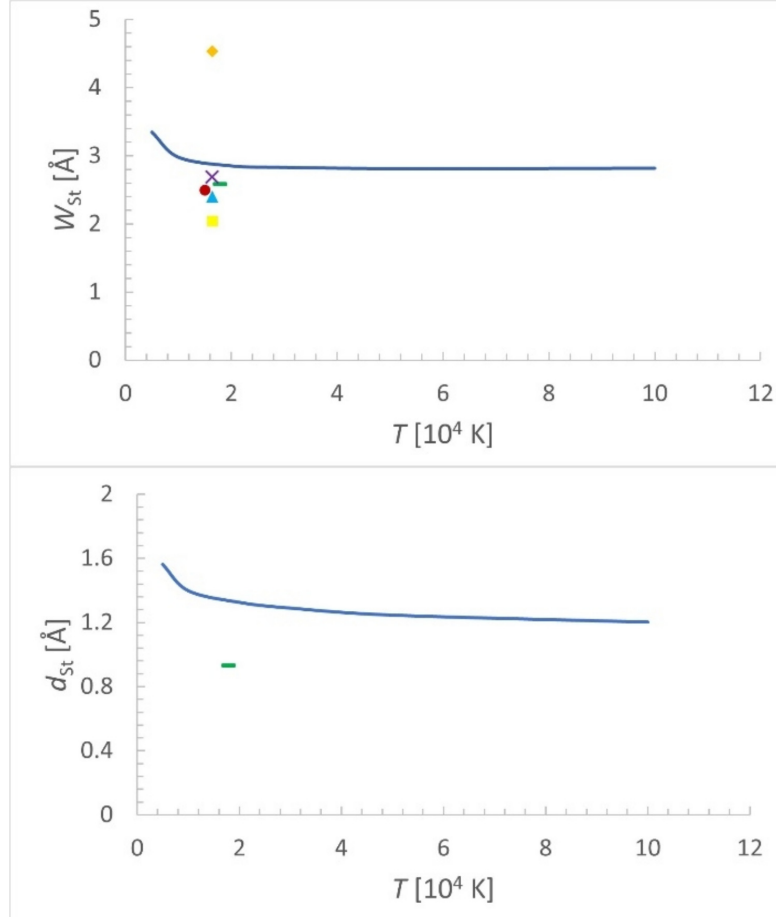


Figure 3. Comparison of the calculated temperature dependence (solid line) of Stark width (up) and shift (down) with experimental results from the literature for spectral line Si II $3s^2 4p \ ^2P_{3/2}^o - 3s^2 4d \ ^2D_{5/2}$ with $\lambda = 5052.4 \text{ \AA}$. The perturber density is $1.10^{17} \text{ cm}^{-3}$. Symbols illustrate results from: Lesage et al. (1977) (cross); Kusch & Schroeder (1982) (rhomb); Lesage et al. (1983) (solid triangle); Pérez et al. (1993) (solid square); González et al. (2002) (dash) and Bukvić et al. (2008) (solid circle).

$3s^2 5s \ ^2S_{1/2}$. There are four width measurements that we found. Three of them (Lesage et al., 1983; González et al., 2002; Bukvić et al., 2008) are grouped and closer to the calculated value, a little bit lower. The Stark width reported by Kusch & Schroeder (1982) is larger from all of them. The theory gives positive (red) shift of this line, and the experiment confirms that. Measured value is smaller again as in the previous case.

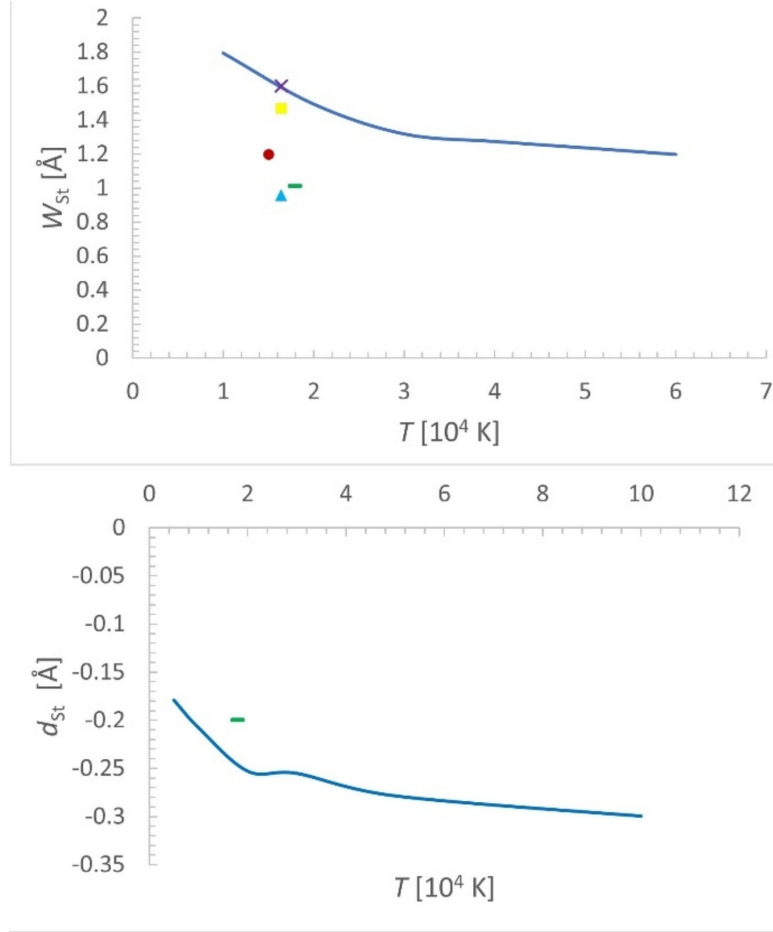


Figure 4. Comparison of the calculated temperature dependence (solid line) of Stark width (up) and shift (down) with experimental results from the literature for spectral line Si II $3s^2 3d^2 D_{5/2} - 3s^2 4f^2 F_{7/2}^o$ with $\lambda = 4130.9 \text{ \AA}$. The perturber density is $1.10^{17} \text{ cm}^{-3}$. Symbols illustrate results from: Lesage et al. (1977) (cross); Lesage et al. (1983) (solid triangle); Pérez et al. (1993) (solid square); González et al. (2002) (dash) and Bukvić et al. (2008) (solid circle).

Next spectral line in our study is in the focus of experimental works. The line is originated from 4d level, corresponding to the transition Si II $3s^2 4p^2 P_{3/2}^o - 3s^2 4d^2 D_{5/2}$ with $\lambda = 5052.4 \text{ \AA}$. Figure 3 demonstrate the behaviour of the corresponding Stark broadening parameters and comparison with experimental data. All measurements are made at close temperatures. There are six width measurements. Five results (Lesage et al., 1977, 1983; Pérez et al., 1993; Gon-

zález et al., 2002; Bukvić et al., 2008) are close to each other and close to the theoretical dependence except data by Kusch & Schroeder (1982) which are higher. The line shift is positive. The deviation of shift result of González et al. (2002) is practically the same as for the previous line. Its value is lower than calculated but the separation from the theoretical curve is smaller than that in Fig. 2.

There are five width measurements from different literature sources (Lesage et al., 1977; González et al., 2002; Lesage et al., 1983; Pérez et al., 1993; González et al., 2002; Bukvić et al., 2008) for line Si II $3s^2 3d \ ^2D_{5/2} - 3s^2 4f \ ^2F_{7/2}^o$ with $\lambda = 4130.9 \text{ \AA}$. (Fig. 4, upper part). They are placed in a vertical intercept as they correspond to close temperature values. The width measured by Lesage et al. (1977) is laying on the curve, the value of Pérez et al. (1993) is close, those of Lesage et al. (1983) and González et al. (2002) are relatively far and close to each other, and the value of Bukvić et al. (2008) is in the middle of the interval where are experimental values. Both predicted shift temperature dependence and measured value (González et al., 2002) are negative, and they are relatively close. Shift comparison in the four cases shows that the disagreement is smaller for higher transitions.

4. CONCLUSION

Recent new calculations for Stark broadening widths and shifts of singly ionized silicon spectral lines for 62 multiplets, performed by using the semiclassical perturbation method (Sahal-Bréchet, 1969a,b; Sahal-Bréchet, Dimitrijević, & Ben Nessib, 2014), have been tested by comparison with experimental data. The agreement with experiments is acceptable in average and it is better for widths than for shifts. In the case of shifts agreement with experimental values is better for transitions involving higher angular momentum quantum numbers. The new Stark broadening data for Si II will be implemented in the Stark-B database (<http://stark-b.obspm.fr/>), which is included in Virtual Atomic and Molecular Data Center (VAMDC) (<http://www.vamdc.org/>).

Acknowledgements. This work has been supported with a STSM visit grant for M.S.D. within the framework of COST Action CA 18104 "Revealing the Milky Way with GAIA".

The authors would like to thank to Research and Development Sector at the Technical University of Sofia for the financial support covering the conference fee for M.D.C.

References

- Arsenijević, V., Fabbro, S., Mourão, A. M., & Rica da Silva, A. J., Diversity of supernovae Ia determined using equivalent widths of Si II 4000. 2008, *Astronomy and Astrophysics*, **492**, 535, DOI: 10.1051/0004-6361:200810675

- Bukvić, S., Spasojević, D., & Žigman, V., Advanced fit technique for astrophysical spectra. Approach insensitive to a large fraction of outliers. 2008, *Astronomy and Astrophysics*, **477**, 967, DOI: 10.1051/0004-6361:20065969
- Chiang, W. T. & Griem, H. R., Measurements of the Stark broadening of ionized silicon lines from a plasma. 1978, *Physical Review A*, **18**, 1169, DOI: 10.1103/PhysRevA.18.1169
- Dimitrijević, M. S. & Konjević, N., Stark widths of doubly- and triply-ionized atom lines. 1980, *Journal of Quantitative Spectroscopy and Radiative Transfer*, **24**, 451, DOI: 10.1016/0022-4073(80)90014-X
- Dimitrijević, M. S. & Kršljanin, V., Electron-impact shifts of ion lines: modified semiempirical approach. 1986, *Astronomy and Astrophysics*, **165**, 269
- Fleurier, C., Stark profiles of some ion lines of alkaline earth elements. 1977, *Journal of Quantitative Spectroscopy and Radiative Transfer*, **17**, 595, DOI: 10.1016/0022-4073(77)90019-X
- González, V. R., Aparicio, J. A., del Val, J. A., & Mar, S., Stark broadening and shift measurements of visible Si II lines. 2002, *Journal of Physics B Atomic Molecular Physics*, **35**, 3557, DOI: 10.1088/0953-4075/35/16/314
- Iijima, T. & Nakanishi, H., Spectroscopic observations of the first helium nova V445 Puppis. 2008, *Astronomy and Astrophysics*, **482**, 865, DOI: 10.1051/0004-6361:20077502
- Konjević, N., Purić, J., Čirković, L. J., & Labat, J., Measurements of the Stark broadening parameters of several Si II lines. 1970, *Journal of Physics B Atomic Molecular Physics*, **3**, 999, DOI: 10.1088/0022-3700/3/7/014
- Konjević, N. & Wiese, W. L., Experimental Stark widths and shifts for spectral lines of neutral and ionized atoms. 1990, *Journal of Physical and Chemical Reference Data*, **19**, 1307, DOI: 10.1063/1.555847
- Kusch, H. J. & Schroeder, K., Experimental Stark broadening data of SI II and SI III lines. 1982, *Astronomy and Astrophysics*, **116**, 255
- Lanz, T., Dimitrijević, M. S., & Artru, M. C., Stark broadening of visible Si II lines in stellar atmospheres. 1988, *Astronomy and Astrophysics*, **192**, 249
- Lesage, A., Experimental Stark widths and shifts for spectral lines of neutral and ionized atoms A critical review of selected data for the period 2001-2007. 2009, *New Astronomy Review*, **52**, 471, DOI: 10.1016/j.newar.2008.01.001
- Lesage, A., Rathore, B. A., Lakićević, I. S., & Purić, J., Stark widths and shifts of singly ionized silicon spectral lines. 1983, *Physical Review A*, **28**, 2264, DOI: 10.1103/PhysRevA.28.2264
- Lesage, A., Sahal-Bréchet, S., & Miller, M. H., Stark broadening of singly ionized silicon. 1977, *Physical Review A*, **16**, 1617, DOI: 10.1103/PhysRevA.16.1617
- Pérez, C., de la Rosa, I., de Frutos, A. M., & Mar, S., Temperature dependence of Stark broadening for several Si II lines. 1993, *Physical Review E*, **47**, 756, DOI: 10.1103/physreve.47.756

- Peytreman, E., Theoretical Effect of Various Broadening Parameters on Ultraviolet Line Profiles. 1972, *Astronomy and Astrophysics*, **17**, 76
- Sahal-Bréchet, S., Impact Theory of the Broadening and Shift of Spectral Lines due to Electrons and Ions in a Plasma. 1969a, *Astronomy and Astrophysics*, **1**, 91
- Sahal-Bréchet, S., Impact Theory of the Broadening and Shift of Spectral Lines due to Electrons and Ions in a Plasma (Continued). 1969b, *Astronomy and Astrophysics*, **2**, 322
- Sahal-Bréchet, S., Dimitrijević, M., & Ben Nessib, N., Widths and Shifts of Isolated Lines of Neutral and Ionized Atoms Perturbed by Collisions With Electrons and Ions: An Outline of the Semiclassical Perturbation (SCP) Method and of the Approximations Used for the Calculations. 2014, *Atoms*, **2**, 225, DOI: 10.3390/atoms2020225
- Shi, J. R., Gehren, T., Butler, K., Mashonkina, L. I., & Zhao, G., Statistical equilibrium of silicon in the solar atmosphere. 2008, *Astronomy and Astrophysics*, **486**, 303, DOI: 10.1051/0004-6361:200809452

On the Stark broadening parameters of Sn III spectral lines

Z. Simić¹ , M.S. Dimitrijević^{1,2}, S. Sahal-Bréchet² and N. Sakan³

¹ *Astronomical Observatory, Volgina 7, 11060 Belgrade, Serbia (E-mail: zsimic@aob.rs)*

² *LERMA, Observatoire de Paris, F-92195 Meudon Cedex, France*

³ *University of Belgrade, Institute of Physics, PO Box 57, 11001 Belgrade, Serbia*

Received: August 23, 2022; Accepted: October 5, 2022

Abstract. Stark broadening parameters for four Sn III spectral line obtained by using semiclassical perturbation approach and Stark widths for this transitions obtained by using modified semiempirical approach have been compared with available experimental and semiempirical data and used for the consideration of the influence of the Stark broadening effect in A type stellar atmospheres.

Key words: Atomic data – Spectral lines – A type stars

1. Introduction

Data on Stark broadening are necessary for the study of astrophysical and technological plasmas, and the need for them has also increased in the laboratory and for fusion and lasers. Today, their application in spectroscopy is necessary for a better understanding of the spectrum of an element that is only present in traces in stars.

One of the first report made by Lunt (1907), announces that a strong tin line occurred on the ultraviolet side of the iron line in the spectrum of α Scorpii. Some spectral lines of tin have been specifically measured such as 4525.01Å which shows that it is more likely to coincide with Rowland's solar line 4525.009Å than with the line closer to the iron line 4525.110Å with different intensities of these two lines. It was also found that many of the tin lines occur in the longer wavelength region.

Tin is an element in Group 14 (the carbon family) and has mainly metallic properties. It has atomic number 50 and an atomic mass of 118.710 atomic mass units. Its ground state electron configuration is noted with [Kr] $4d^{10}5s^25p^2$. Its presence in stellar atmospheres has been reported several times, for example neutral tin in the spectra of A type star γ Equ (Adelman et al., 1979) single ionized tin in Przybylski's star by Cowley et al. (2000). Spectral lines of Sn III registered in the NIST database reach the number of 259, most of which have

a relative intensity below 500, while the others have a higher intensity of up to 1000. Considering that these lines are of similar intensity and appear often with iron lines, they are often obscured by other lines and for now, they are still difficult to be seen in stellar spectra. Chayer et al. (2005) report the presence of elements beyond the iron group in the atmospheres of the cool DO white dwarfs HD 149499 B and HZ 21, specially Sn IV.

Kieft et al. (2004) measured Stark widths and they also, obtained the first theoretical result by using semiempirical (Griem, 1968) approach. We used this results and compared them with our results for Sn III $6s\ ^1S_0 - 6p\ ^1P_1^o$ spectral line (Simić et al., 2008). Here we add the following three spectral lines that are compared with experimental and semi-empirical calculations.

Alonso-Medina & Colón (2011) report on the calculated values of the Stark broadening parameters for 171 lines of Sn III arising from $4d^{10}5sns$ ($n = 69$), $4d^{10}5snp$ ($n = 5, 6$), $4d^{10}5p^2$, $4d^{10}5snd$ ($n = 57$), $4d^{10}5s4f$ and $4d^{10}5s5g$. Stark widths and shifts are presented for an electron density of $10^{23}m^{-3}$ and temperature range (11 00075 000) K. These have been calculated using a semi-empirical approach, with a set of wavefunctions obtained from HartreeFock relativistic calculations, including core polarization effects. The results obtained have been compared with available experimental data.

2. Method

Stark broadening parameter values for doubly charged tin have been obtained using semi-classical method (Sahal-Bréchet, 1969a,b), which is more accurate in contrast to the modified semiempirical method (Dimitrijević & Konjević, 1980) that served us to determine the Stark widths for the same transition thus enabling the comparison of these methods. Different later inovations and optimizations of this theoretical method have been described in details in Sahal-Bréchet (1974, 1991); Fleurier et al. (1977); Dimitrijević et al. (1991); Sahal-Bréchet et al. (2014). Within this theory the FWHM - Full Width at Half intensity Maximum (W) and the shift (d) of an isolated line, originating from the transition between the initial level i and the final level f is expressed for an ionized atom as:

$$W = N \int v f(v) dv \left(\sum_{i' \neq i} \sigma_{ii'}(v) + \sum_{f' \neq f} \sigma_{ff'}(v) + \sigma_{el} \right)$$

$$d = N \int v f(v) dv \int_{R_3}^{R_D} 2\pi \rho d\rho \sin(2\varphi_p). \quad (1)$$

where i' and f' are perturbing levels, N and v are the electron density and the velocity of perturbers respectively, $f(v)$ is the Maxwellian distribution of

electron velocities, and ρ the impact parameter of the free electron colliding with the emitter.

The inelastic cross sections $\sigma_{ii'}(v)$ (respectively $\sigma_{ff'}(v)$), can be expressed by an integration of the transition probability $P_{jj'}(\rho, v)$, $j = i, f$; $j' = i', f'$, over the impact parameter ρ as:

$$\sum_{i' \neq i} \sigma_{ii'}(v) = \frac{1}{2} \pi R_1^2 + \int_{R_1}^{R_D} 2\pi \rho d\rho \sum_{i' \neq i} P_{ii'}(\rho, v). \quad (2)$$

and the elastic contribution to the width is given by:

$$\sigma_{el} = 2\pi R_2^2 + \int_{R_2}^{R_D} 2\pi \rho d\rho \sin^2 \delta + \sigma_r, \quad (3)$$

$$\delta = (\varphi_p^2 + \varphi_q^2)^{\frac{1}{2}}.$$

Here σ_{el} is the elastic cross section, while φ_p (r^{-4}) and φ_q (r^{-3}), are phase shifts due to the polarization and quadrupolar potential respectively, and are defined in Section 3 of Chapter 2 in Sahal-Br  chot (1969a). The cut-offs R_1 , R_2 , R_3 , and the Debye radius R_D , as well as the symmetrization procedure are described in Section 1 of Chapter 3 in Sahal-Br  chot (1969b). The contribution of Feshbach resonances, σ_r is explained in Fleurier et al. (1977) and Sahal-Br  chot (2021).

Within the semiclassical perturbation theory is assumed that electrons are moving along hyperbolic paths due to attractive Coulomb force, while in the case of ionic perturbers this force is repulsive, so that trajectories are different. For ion-impact broadening the formulae are analogous to Eqs. (1) - (3) for electron-impact broadening.

If the considered lines are isolated, the line profile $F(\omega)$ has Lorentzian form and can be expressed as:

$$F(\omega) = \frac{W/(2\pi)}{(\omega - \omega_{if} - d)^2 + (W/2)^2} \quad (4)$$

where

$$\omega_{if} = \frac{E_i - E_f}{\hbar}$$

and E_i , E_f are the energies of initial and final state, respectively. Consequently, if we know Stark width W and shift d it is easy to determine the profile of a considered spectral line.

In addition to the semiclassical method, we also performed a calculation using a modified semiempirical method (MSE) which is described in details in reference Dimitrijevi   & Konjevi   (1980).

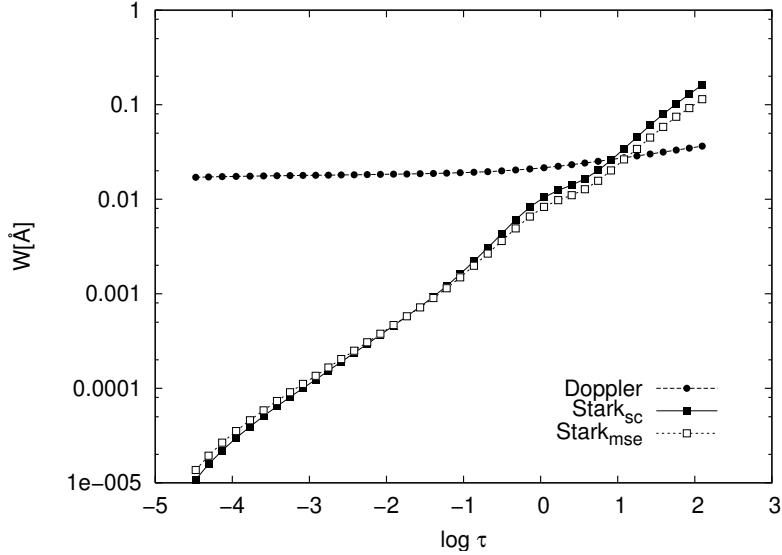


Figure 1. Stark widths (sc-semiclassical and mse-modified semiempirical) and thermal Doppler widths for Sn III 5226.2 Å spectral lines as a function of Roseland optical depth for an A type model of stellar atmosphere $T_{\text{eff}} = 10000$ K, $\log g = 4.5$ (Kurucz, 1979).

3. Results

For four doubly ionized tin spectral lines Stark broadening parameters, the full semiclassical perturbation approach (Sahal-Bréchet, 1969a,b) as well as the modified semiempirical approach (Dimitrijević & Konjević, 1980) have been applied. The needed energy levels have been taken from Moore (1971). The oscillator strengths have been calculated by using the method of Bates & Damgaard (1949), and the tables of Oertel & Shomo (1968). For higher levels, the method of van Regemorter et al. (1979) has been used.

The tables 1 and 2 contain the results of our calculations of Stark broadening parameters for four lines of Sn III and we specify a parameter C (Dimitrijević & Sahal-Bréchet, 1984) which gives an estimate for the maximum perturber density for which the line may be treated as isolated, when it is divided by the corresponding full width at half maximum.

Experimental values by Kieft et al. (2004) have been obtained by arc discharge through tin vapor. The Stark half-widths of doubly ionized tin have been measured at an electron density of 10^{17} cm^{-3} and an electron temperature of 11604 K. All broadening mechanisms have been investigated. Natural broadening is negligible. The Doppler broadening only becomes significant at 30 times higher electron temperature values, but does not exceed the value

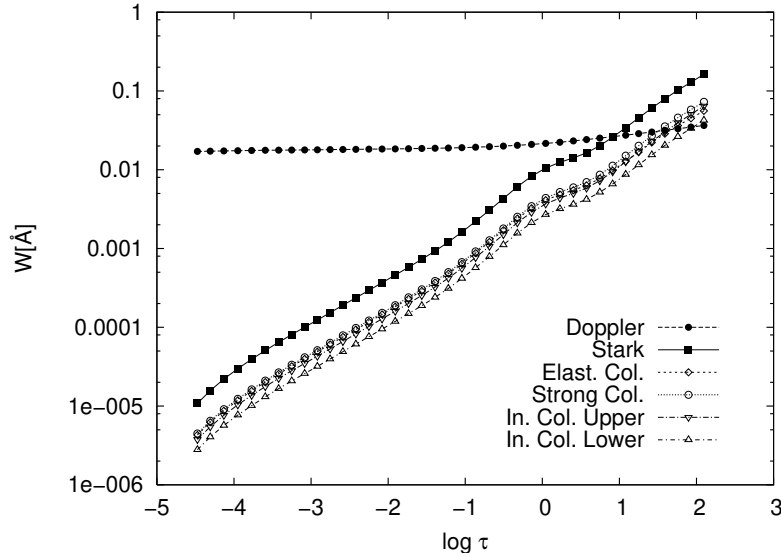


Figure 2. Stark and thermal Doppler widths and widths due to various collisional processes for Sn III 5226.2 Å spectral lines as a function of Roseland optical depth for an A type model of stellar atmosphere $T_{\text{eff}} = 10000$ K, $\log g = 4.5$ Kurucz (1979).

of 0.25\AA . Broadening due to collisions with neutral atoms is far less than the interaction with charged particles. Therefore, Stark broadening dominates all the mentioned mechanisms. All measured Sn III profiles show a Voigt profile, with a fixed Gaussian contribution originating in the aperture profile while the Lorentzian contribution is entirely attributed to Stark broadening.

Experimental and theoretical values within the framework of semi-empirical approaches obtained by Kieft et al. (2004) for spectral lines Sn III for which we also did the calculations enable us to compare the obtained results. There is a good agreement with experimental value of both our results obtained by using semiclassical and modified semiempirical approach for Stark width for Sn III, see Table 3. Obviously, this ratio is better for our values than for semiempirical one obtained by Kieft et al. (2004) using Griem (1968) method, which uses semiempirical Gaunt factor suitable for singly charged ions (see Dimitrijević & Konjević, 1980).

We used Kurucz (1979) atmosphere model of A type star with effective temperature $T_{\text{eff}} = 10000$ K and logarithm of surface gravity $\log g = 4.5$. As one can see from Fig 1. there are layers where Stark broadening is less significant compared to the thermal Doppler effect, but, if it is not sufficiently small, it may have influence on the wings of the spectral line. For $\log \tau \geq 1$ Stark broadening effect is more and more expressive and becomes the dominant. Contributions of

Table 1. Stark broadening parameters for Sn III spectral lines for perturber density of 10^{17}cm^{-3} and temperature range from 10000 up to 150000 K, obtained by using the semiclassical perturbation method (Sahal-Bréchet, 1969a,b)

Transition	T (K)	W_e (Å)	d_e (Å)	W_p (Å)	d_p (Å)	$W_{\text{He}^{++}}$ (Å)	$d_{\text{He}^{++}}$ (Å)
Sn III 6s $^1S_0 - 6p \ ^1P_1^o$ 5226.2 Å C= 0.24E+21	10000	1.39	-0.149	0.391E-01	-0.207E-01	0.507E-01	-0.189E-01
	20000	1.05	-0.987E-01	0.615E-01	-0.339E-01	0.724E-01	-0.294E-01
	30000	0.907	-0.886E-01	0.758E-01	-0.426E-01	0.794E-01	-0.361E-01
	50000	0.788	-0.900E-01	0.869E-01	-0.513E-01	0.891E-01	-0.423E-01
	150000	0.676	-0.846E-01	0.102	-0.619E-01	0.101	-0.505E-01
Sn III 5d $^3D_1 - 6p \ ^3P_1^o$ 5292.7 Å C= 0.52E+21	10000	0.921	0.727E-02	0.338E-01	0.340E-02	0.460E-01	0.332E-02
	20000	0.692	0.121E-01	0.526E-01	0.673E-02	0.648E-01	0.619E-02
	30000	0.594	0.122E-01	0.640E-01	0.919E-02	0.712E-01	0.806E-02
	50000	0.504	0.143E-01	0.722E-01	0.119E-01	0.783E-01	0.104E-01
	150000	0.423	0.147E-01	0.817E-01	0.159E-01	0.871E-01	0.130E-01
Sn III 5d $^3D_2 - 6p \ ^3P_1^o$ 5350.7 Å C= 0.53E+21	10000	0.945	0.786E-02	0.347E-01	0.358E-02	0.471E-01	0.349E-02
	20000	0.710	0.128E-01	0.539E-01	0.707E-02	0.664E-01	0.650E-02
	30000	0.610	0.129E-01	0.656E-01	0.964E-02	0.730E-01	0.843E-02
	50000	0.517	0.150E-01	0.740E-01	0.125E-01	0.802E-01	0.109E-01
	150000	0.434	0.155E-01	0.838E-01	0.166E-01	0.892E-01	0.135E-01
Sn III 5d $^3D_1 - 6p \ ^3P_0^o$ 5371.1 Å C= 0.53E+21	10000	0.948	0.791E-02	0.347E-01	0.371E-02	0.471E-01	0.361E-02
	20000	0.712	0.132E-01	0.539E-01	0.730E-02	0.665E-01	0.671E-02
	30000	0.612	0.133E-01	0.656E-01	0.995E-02	0.731E-01	0.868E-02
	50000	0.519	0.154E-01	0.741E-01	0.129E-01	0.803E-01	0.112E-01
	150000	0.434	0.172E-01	0.839E-01	0.170E-01	0.894E-01	0.140E-01
		0.399	0.167E-01	0.892E-01	0.190E-01	0.925E-01	0.155E-01

different collision processes to the total Stark width in comparison with Doppler one, can be seen in Fig. 2. The behavior with $\log \tau$ is similar for Full Stark width as well as for strong, elastic, upper and lower level inelastic contributions..

The investigated Stark broadening parameters for the Sn III are of importance for the study of astrophysical and technological plasmas. For the four selected lines a comparison between semi-classical method Sahal-Bréchet (1969a,b) and the modified semi-empirical method Dimitrijević & Konjević (1980) is carried out. The more precise, but also more time consuming semi-classical method and MSE have shown a good agreement of the calculated data. The importance of the Stark broadening processes is analyzed with the help of the Kurucz (1979) model. From the presented results it could be seen that the use of modified semiempirical method is valid for the analyzed lines and as such could be a recommended one for the fast calculations for the broadening parameters within the ranges of investigated plasma conditions. There is a need for further investigation of lines that could be observed in stellar and laboratory plasma, and as such it is still an open field for both theoretical as well as experimental research and observations.

Table 2. Stark widths obtained by MSE method (Dimitrijević & Konjević, 1980) for Sn III spectral lines for perturber density of 10^{17}cm^{-3} and temperature range from 2500 do 50000 K. These values have been calculated separately in order to compare with the semiclassical results. Only for Sn III $6s\ ^1S_0 - 6p\ ^1P_1^\circ$ spectral line results are taken from Simić et al. (2008)

Transition	T(K)	W(Å)	Prelaz	T(K)	W(Å)
$6s\ ^1S_0 - 6p\ ^1P_1^\circ$ 5226.2Å	2500	2.217	$5d\ ^3D_2 - 6p\ ^3P_1^\circ$ 5350.7Å	2500	1.497
	5000	1.567		5000	1.059
	10000	1.108		10000	0.749
	20000	0.784		20000	0.529
	30000	0.640		30000	0.432
	50000	0.514		50000	0.339
$5d\ ^3D_1 - 6p\ ^3P_1^\circ$ 5292.7Å	2500	1.465	$5d\ ^3D_1 - 6p\ ^3P_0^\circ$ 5371.6Å	2500	1.500
	5000	1.036		5000	1.061
	10000	0.732		10000	0.750
	20000	0.518		20000	0.530
	30000	0.423		30000	0.433
	50000	0.332		50000	0.340

Table 3. Comparison between W_m -experimental Stark widths (Kieft et al., 2004) with theoretical: W_{se} -semiempirical (Kieft et al., 2004), W_{sc} -semiclassical i W_{mse} -modified semiempirical. Results performed for an electron density of 10^{17}cm^{-3} and an electron temperature of 11604K.

Transition	W_m (Å)	Rel. exp error	$\frac{W_m}{W_{se}}$	$\frac{W_m}{W_{sc}}$	$\frac{W_m}{W_{mse}}$
Sn III $6s\ ^1S_0 - 6p\ ^1P_1^\circ$ 5226.2 Å	1.22	50%	1.70	0.92	1.15
Sn III $5d\ ^3D_1 - 6p\ ^3P_1^\circ$ 5292.7 Å	0.86	30%	1.43	0.98	1.23
Sn III $5d\ ^3D_2 - 6p\ ^3P_1^\circ$ 5350.7 Å	0.68	30%	1.13	0.76	0.96
Sn III $5d\ ^3D_1 - 6p\ ^3P_0^\circ$ 5371.1 Å	0.64	30%	1.07	0.70	0.90

Acknowledgements. This work is supported by Ministry of Education, Science and Technological Development of the Republic of Serbia through the project contract No. 451-03-68/2022-14/200002 and 451-03-68/2022-14/200024.

References

- Adelman, S. J., Bidelman, W. P., & Pyper, D. M., The Peculiar A Star γ Equulei: a Line Identification Study of $\lambda\lambda$ 3086 - 3807. 1979, *Astrophysical Journal Supplement*, **40**, 371, DOI: 10.1086/190592
- Alonso-Medina, A. & Colón, C., Stark broadening of Sn III spectral lines of astrophysical interest: predictions and regularities. 2011, *Monthly Notices of the RAS*, **414**, 713, DOI: 10.1111/j.1365-2966.2011.18438.x
- Bates, D. R. & Damgaard, A., The Calculation of the Absolute Strengths of Spectral Lines. 1949, *Philosophical Transactions of the Royal Society of London. Series A, Mathematical and Physical Sciences*, **242**, 101
- Chayer, P., Vennes, S., Dupuis, J., & Kruk, J. W., Abundance of Elements beyond the Iron Group in Cool DO White Dwarfs. 2005, *Astrophysical Journal, Letters*, **630**, L169, DOI: 10.1086/491699
- Cowley, C. R., Ryabchikova, T., Kupka, F., et al., Abundances in Przybylski's star. 2000, *Monthly Notices of the RAS*, **317**, 299, DOI: 10.1046/j.1365-8711.2000.03578.x
- Dimitrijević, M. & Konjević, N., Stark widths of doubly- and triply-ionized atom lines. 1980, *Journal of Quantitative Spectroscopy and Radiative Transfer*, **24**, 451, DOI: [https://doi.org/10.1016/0022-4073\(80\)90014-X](https://doi.org/10.1016/0022-4073(80)90014-X)
- Dimitrijević, M. S. & Sahal-Bréchet, S., Stark broadening of neutral helium lines. 1984, *Journal of Quantitative Spectroscopy and Radiative Transfer*, **31**, 301, DOI: 10.1016/0022-4073(84)90092-X
- Dimitrijević, M. S., Sahal-Bréchet, S., & Bommier, V., Stark Broadening of Spectral Lines of Multicharged Ions of Astrophysical Interest - Part Two - Si IV Lines. 1991, *Astronomy and Astrophysics, Supplement*, **89**, 591
- Fleurier, C., Sahal-Bréchet, S., & Chapelle, J., Stark profiles of some ion lines of alkaline earth elements. 1977, *Journal of Quantitative Spectroscopy and Radiative Transfer*, **17**, 595, DOI: [https://doi.org/10.1016/0022-4073\(77\)90019-X](https://doi.org/10.1016/0022-4073(77)90019-X)
- Griem, H. R., Semiempirical Formulas for the Electron-Impact Widths and Shifts of Isolated Ion Lines in Plasmas. 1968, *Physical Review*, **165**, 258, DOI: 10.1103/PhysRev.165.258
- Kieft, E. R., van der Mullen, J. J. A. M., Kroesen, G. M. W., Banine, V., & Koshelev, K. N., Stark broadening experiments on a vacuum arc discharge in tin vapor. 2004, *Physical Review E*, **70**, 066402, DOI: 10.1103/PhysRevE.70.066402
- Kurucz, R. L., Model atmospheres for G, F, A, B and O stars. 1979, *ApJS*, **40**, 1, DOI: 10.1051/0004-6361/201118205
- Lunt, J., On the presence of tin in stellar atmospheres. 1907, *Monthly Notices of the RAS*, **67**, 487, DOI: 10.1093/mnras/67.7.487

- Moore, C. E. 1971, *Selected tables of atomic spectra - A: Atomic energy levels - Second edition - B: Multiplet tables; N IV, N V, N VI, N VII. Data derived from the analyses of optical spectra*
- Oertel, G. K. & Shomo, L. P., Tables for the Calculation of Radial Multipole Matrix Elements by the Coulomb Approximation. 1968, *Astrophysical Journal, Supplement*, **16**, 175, DOI: 10.1086/190173
- Sahal-Bréchet, S., Impact Theory of the Broadening and Shift of Spectral Lines due to Electrons and Ions in a Plasma. 1969a, *Astronomy and Astrophysics*, **1**, 91
- Sahal-Bréchet, S., Impact Theory of the Broadening and Shift of Spectral Lines due to Electrons and Ions in a Plasma (Continued). 1969b, *Astronomy and Astrophysics*, **2**, 322
- Sahal-Bréchet, S., Stark Broadening of Isolated Lines in the Impact Approximation. 1974, *Astronomy and Astrophysics*, **35**, 319
- Sahal-Bréchet, S., Broadening of ionic isolated lines by interactions with positively charged perturbers in the quasistatic limit. 1991, *Astronomy and Astrophysics*, **245**, 322
- Sahal-Bréchet, S., The Semiclassical Limit of the Gailitis Formula Applied to Electron Impact Broadening of Spectral Lines of Ionized Atoms. 2021, *Atoms*, **9**, 29, DOI: 10.3390/atoms9020029
- Sahal-Bréchet, S., Dimitrijević, M., & Nessib, N., Widths and Shifts of Isolated Lines of Neutral and Ionized Atoms Perturbed by Collisions With Electrons and Ions: An Outline of the Semiclassical Perturbation (SCP) Method and of the Approximations Used for the Calculations. 2014, *Atoms*, **2**, 225, DOI: 10.3390/atoms2020225
- Simić, Z., Dimitrijević, M. S., Kovačević, A., & Dačić, M., Stark broadening of Sn III lines in a type stellar atmospheres. 2008, *Publications de l'Observatoire Astronomique de Beograd*, **84**, 487
- van Regemorter, H., Binh Dy, H., & Prudhomme, M., Radial transition integrals involving low or high effective quantum numbers in the Coulomb approximation. 1979, *Journal of Physics B Atomic Molecular Physics*, **12**, 1053, DOI: 10.1088/0022-3700/12/7/009

Atomic structure and transition parameters of the V XVIII carbon-like ion

Lamia Abu El Maati¹, Mahmoud Ahmad^{2,3}, I.S. Mahmoud^{2,4},
Sahar G. Tawfik^{5,6}, Najah Alwadii⁷, Nabil Ben Nessib⁸ and
M.S. Dimitrijević^{9,10}

¹ *Department of Physics, Faculty of Science, Benha University, Benha,
13513, Egypt.*

² *Physics Department, College of Science in Zulfi, Majmaah University,
11952, Saudi Arabia.*

³ *Physics Department, Faculty of Science, Al Azhar University,
71524 Assuit, Egypt.*

⁴ *Physics Department, Faculty of Science, Suez Canal University, Ismailia,
Egypt.*

⁵ *Physics Department, Faculty of Science, Alexandria University, Egypt.*

⁶ *Department of Physics, College of Science, Princess Nourah Bint
Abdulahman University, P.O. Box 84428, Riyadh 11671, Saudi Arabia.*

⁷ *Department of Physics, College of Sciences, King Khalid University, Saudi
Arabia.*

⁸ *Department of Physics and Astronomy, College of Sciences, King Saud
University, Saudi Arabia.*

⁹ *Astronomical Observatory, Volgina 7, 11060 Belgrade, Serbia.*

¹⁰ *LERMA, Observatoire de Paris, Universit PSL, CNRS, Sorbonne
Universit, 5 Place Jules Janssen, 92190 Meudon, France.*

Received: August 23, 2022; Accepted: October 1, 2022

Abstract. The atomic and transition parameters of carbon-like ions are significant for many important astrophysical researches, such as the modeling of stellar atmospheres, the determination of stellar abundance, the analysis of spectral lines for laboratory plasmas or astronomical objects. In this contribution, we calculated the energy levels and lifetimes of the carbon-like vanadium ion (V XVIII) using the atomic structure codes AUTOSTRUCTURE and GRASP2018. Weighted oscillator strengths and transition probabilities are also calculated for the allowed transitions between the energy levels considered. The calculations were carried out for the first 17 configurations: $2s^2 2p^2$, $2p^4$, $2s^2 2p^3 p$, $2s 2p^2 3s$, $2s 2p^2 3d$, $2p^3 3p$, $2s^2 2p^4 p$, $2s^2 3d^2$, $2s 2p^3$, $2s^2 2p^3 s$, $2s^2 2p^3 d$, $2s 2p^2 3p$, $2p^3 3s$, $2p^3 3d$, $2s^2 2p^4 s$, $2s^2 2p^4 d$ and $2s 2p^3 d^2$.

Key words: energy levels – lifetimes – oscillator strengths – transition probabilities – AUTOSTRUCTURE – GRASP2018

1. Introduction

A wide variety of astrophysical plasmas show emission lines resulting from transitions involving carbon-like (C-like) ions, such as planetary nebulae (Aller, 1987) and the solar corona (Widing et al., 1986; Widing & Cook, 1987) as well as being observed in the laboratory (Keenan et al., 1988). For this reason, many theoretical and experimental investigations of the spectra of C-like ions have been performed. In the Opacity Project, atomic data for photoabsorption from a large number of bound states; energy levels, oscillator strengths and photoionisation cross sections are computed for carbon like ions (Luo & Pradhan, 1989). Fawcett (1987) used the HartreeFock pseudo-relativistic (HFR) code of Cowan (1981) to calculate oscillator strengths and energy levels in C-like ions between F IV and Ni XXIII. Bhatia & Doschek (1993), used the SUPERSTRUCTURE (SS) code to calculate electron impact collision strengths and spontaneous radiative decay rates for the C-like ion, Si IX. Zhang & Sampson (1996) and Zhang & Sampson (1996) calculated values for a large number of states using GRASP (General purpose Relativistic Atomic Structure Program). Aggarwal et al. (1997), Aggarwal (1998) and Aggarwal et al. (2001) have obtained rates between low-lying states using the CIV3 code for a number of C-like ions. Froese Fischer & Tachiev (2004) calculated energy levels and transition rates for low-lying states using multi-configuration BreitPauli wave-functions. Jönsson et al. (2011) used the relativistic configuration interaction (RCI) method to obtain energy levels, transition rates, hyperfine structure parameters and Landé g_J values in carbon like ions. Recently, Li et al. (2022) performed a large-scale Multi-Configuration Dirac-Hartree-Fock (MCDHF) calculations for the $n \leq 5$ states in C-like ions from O III to Mg VII.

Vanadium is an important element in physics laboratories and in technology. The first C-like spectra of V XVIII in the range 16-22 Å are reported by Goldsmith et al. (1972). Jönsson et al. (2011) used MCDHF to calculate energies, electric dipole, magnetic dipole, and electric quadrupole transition rates, hyperfine structures, and Landé g_J factors from relativistic configuration interaction calculations for the states of the $(1s^2)2s^22p^2$, $2s2p^3$, and $2p^4$ configurations in all C-like ions between F IV and Ni XXIII. Ekman et al. (2014) have performed Self-consistent MCDHF and subsequent RCI calculations using the GRASP2K program suite in the carbon isoelectronic sequence from Ar XIII to Zn XXV. Most recently, Wu et al. (2022) presented a theoretical study of the transition energies and the oscillator strengths gf for the C-like ions (with Z from 14-36) subject to plasma environment for atomic transitions.

In a first work concerning the atomic structure in the C-like ions (Al-Modlej et al., 2018), we calculated excitation energies and oscillator strengths for the $2s^22p^2$, $2s2p^3$, $2s^22p3s$, $2s^22p3p$, $2s^22p3d$, $2s^22p4s$, $2s^22p4p$, and $2s^22p5s$ configurations in C-like ions from N II to Ne V, using the three different codes: Cowan (Cowan, 1981), SUPERSTRUCTURE (Eissner et al., 1974), and AU-

TOSTRUCTURE (Badnell, 1986). The two latest codes use the Thomas-Fermi-Dirac-Amaldi (TFDA) potential method.

After this purely *ab initio* calculations, we extended the same methods (HFR and TFDA methods) to calculate *ab initio* and semi-empirical values in the C-like sequence from Na VI to Ar XIII (Almodlej *et al.*, 2021). We added the calculation of the transition probabilities of these C-like ions. We also calculated atomic structure and transition parameters of the Ca XIV C-like ion (Alwadie *et al.*, 2020). The calculated parameters are produced by the suite of atomic structure codes of GRASP2018 (Froese Fischer *et al.*, 2019). The configuration expansion of the basis set used consists of 4 even parity configurations: $2s^2 2p^2$ and $2s^2 2p np$ ($n = 3 - 5$) and 5 odd parity configurations: $2s 2p^3$, $2s^2 2p ns$ ($n = 3 - 5$) and $2s^2 2p 3d$. The calculated values of energy levels and oscillator strengths obtained with the GRASP2018 code have been compared with other theoretical methods and with data from NIST database (Kramida *et al.*, 2021).

In this work, we extend our previous works to study the atomic structure and transition parameters of the C-like ion V XVIII using the TFDA and MCDHF methods. In section 2, we present briefly the two methods of calculation used for this work. In section 3, we present the results and discussion, and we finish by concluding in section 4

2. Theoretical methods

We will use two completely different methods TFDA and MCDHF:

2.1. Thomas-Fermi-Dirac-Amaldi (TFDA) potential method

In this method approximate Thomas-Fermi-Dirac-Amaldi (TFDA) potential used in the Hamiltonian of the system. This potential is given as follows:

$$V(r) = \frac{Z_{eff}(\lambda_{nl}, r)}{r} = -\frac{Z}{r}\varphi(x) \quad (1)$$

where

$$\varphi(x) = e^{-\frac{Zr}{2}} + \lambda_{nl} \left(1 - e^{-\frac{Zr}{2}}\right), x = \frac{r}{\mu}$$

and

$$\mu = \frac{1}{4} \left(\frac{N}{N-1}\right)^{2/3} \left(\frac{9\pi^2}{2Z}\right)^{1/3} \approx 0.8853 \left(\frac{N}{N-1}\right)^{2/3} (Z)^{-1/3}$$

where Z is the atomic number and N the number of electrons. Z_{eff} is the effective charge function depending on λ_{nl} and r . λ_{nl} are the orbital scaling parameters.

This theoretical method is used by the AUTOSTRUCTURE (AS) atomic structure code (Badnell, 2011, 2022) .

A configuration C is defined by a set of one-particle orbitals $n_i\ell_i$. It can be represented by [Eissner et al. \(1974\)](#):

$$C \equiv \prod_{\gamma=1}^m (n_\gamma\ell_\gamma)^{q_\gamma} = (n_1\ell_1)^{q_1} (n_2\ell_2)^{q_2} \dots (n_m\ell_m)^{q_m}, \sum_{\gamma=1}^m q_\gamma = N \quad (2)$$

Each configuration gives rise to a set of terms $\Gamma S L M_S M_L$ which defines a solution ψ of the system.

The TFDA potential is included in the Hamiltonian in any of the two coupling models, Russell-Saunders (LS) or intermediate (LSJ). It is diagonalized to obtain eigenvalues and eigenvectors:

In LS coupling, the wave functions of an N electrons atom or ion, can be written as:

$$\psi = \psi(\Gamma S M_S M_L | x_1, \dots x_N) \quad (3)$$

which are eigenvectors with the corresponding eigenvalues in this state $E(LS)$.

In intermediate coupling, the wave functions of an N electrons atom or ion, can be written as:

$$\psi = \psi(\Gamma S L J M_J | x_1, \dots x_N) \quad (4)$$

which are eigenvectors with the corresponding eigenvalues in this state $E(LSJ)$.

2.2. Multi-Configuration Dirac-Hartree-Fock (MCDHF) method

The fully relativistic multiconfiguration Dirac-Hartree-Fock (MCDHF) method described by [Fischer et al. \(2016\)](#) for computing the atomic structures and radiative parameters is used for C-like V XVIII ion, with the latest version of GRASP (General Relativistic Atomic Structure Program), i.e. GRASP2018 ([Froese Fischer et al., 2019](#)). In this approach, the atomic state functions (ASFs), Ψ , are represented by a superposition of configuration state functions (CSFs), Φ , with the same parity, P , total angular momentum, and total magnetic quantum numbers, J and M :

$$\psi(\gamma P J M) = \sum_{j=1}^{N_{CSF}} c_j \Phi(\gamma_j P J M), \quad (5)$$

where the label γ_j represents all the other quantum numbers needed to uniquely specify CSFs that are jj -coupled Slater determinants built from one-electron spinorbitals. The configuration mixing coefficients c_j are obtained through the diagonalisation of the Dirac-Coulomb Hamiltonian

$$H_{DC} = \sum_{i=1}^N [c\alpha_i \cdot \mathbf{p}_i + (\beta_i - 1) c^2 + V(r_i)] + \sum_{i>j}^N \frac{1}{r_{ij}} \quad (6)$$

where $V(r)$ is the monopole part of the electron-nucleus interaction. Finally, the high-order relativistic effects, i.e. the Breit interaction, QED self-energy and

vacuum polarization effects are incorporated in the relativistic configuration interaction (RCI) step of the GRASP2018 package. In the present work, we optimize the wave functions and the corresponding energy levels by gradually increasing the basis of CSFs, and thus taking into account more correlated orbitals.

In the present work valence, corevalence, and corecore correlation effects were included, and the configuration expansions were obtained by single/double-excitations to active sets with principal quantum numbers n from 3 to 8 and orbital quantum numbers $\ell = 0,1,2,3$ (i.e., angular symmetries s, p, d, f) from all shells belongs to multireference (MR) configurations of $(1s^2) 2s^2 2p^2$, $2s2p^3$, $2p^4$, $2s^2 3d^2$, $2s 2p 3d^2$, $2s^2 2p 3\ell$, $2s 2p^2 3\ell$, $2p^3 3\ell$ and $2s^2 2p 4\ell$ ($\ell = s,p,d,f$).

The multireference was chosen based on the criteria that it should contain the configurations that had the largest weights in the preceding self-consistent field calculations (Jansson *et al.*, 2011). Among the states generated by single/double-excitations from the multireference set, only those interacting with the multireference states were kept. The self-consistent field calculations for each layer of orbitals were followed by RCI calculations, including the Breit interaction. The leading QED effects vacuum polarization and self-energy were included in the final multireference RCI calculations. The total number of CSFs that are included in the calculations in the different layers is shown in Tab. 1

Table 1. The total number of CSFs that are included in the calculations in the different layers of V XVIII.

Parity	n	$2J_{min}$	$2J_{max}$	No. of CSF
Even	MR	0	10	139
	4			9730
	5			27894
	6			55573
	7			92767
	8			139476
Odd	MR	0	12	222
	4			12239
	5			36725
	6			74141
	7			124646
	8			188222

3. Results and discussion

We used the v28.46.9 version of AS (Badnell, 2022) and the GRASP2018 (Froese Fischer et al., 2019) of the GRASP atomic structure codes. The two codes are applied to study the atomic structure (energy levels and lifetimes) and transition parameters (oscillator strengths and transition probabilities) for the vanadium C-like ion (V XVIII).

3.1. Atomic structure of the V XVIII ion

Table 2. Energy levels calculated by AS code (E_{ab} (AS) for ab initio and E_{fit} (AS) fitted calculated values) and E(GRASP) for GRASP2018 code calculated values, compared with NIST database values E(NIST). All energies are in cm^{-1}

No.	Level	E(NIST)	E_{ab} (AS)	E_{fit} (AS)	E(GRASP)
1	$2s^2 2p^2 ({}^3P) {}^3P_0$	0	0	0	0
2	$2s^2 2p^2 ({}^3P) {}^3P_1$	37960	38494	38194	37771
3	$2s^2 2p^2 ({}^3P) {}^3P_2$	68190	69636	67897	68088
4	$2s^2 2p^2 ({}^1D) {}^1D_2$	160910	166591	161667	161161
5	$2s^2 2p^2 ({}^1S) {}^1S_0$	269000	272384	269025	268878
6	$2s 2p^3 ({}^4S) {}^5S_2$	366870	355786	366944	366708
7	$2s 2p^3 ({}^3D) {}^3D_2$	623860	625808	624102	625018
8	$2s 2p^3 ({}^3D) {}^3D_1$	625040	627032	625194	626316
9	$2s 2p^3 ({}^3D) {}^3D_3$	634950	637632	635238	636125
10	$2s 2p^3 ({}^3P) {}^3P_0$	731870	733749	732154	733015
11	$2s 2p^3 ({}^3P) {}^3P_1$	735420	737632	735618	736611
12	$2s 2p^3 ({}^3P) {}^3P_2$	743350	746031	743584	744581
13	$2s 2p^3 ({}^4S) {}^3S_1$	897330	905012	897336	901381
14	$2s 2p^3 ({}^2D) {}^1D_2$	908420	920421	909045	911791
15	$2s 2p^3 ({}^2P) {}^1P_1$	1014420	1026011	1015243	1017964
16	$2p^4 {}^3P_2$	1358710	1363958	1358599	1362046
17	$2p^4 {}^3P_1$	1410770	1416810	1411126	1413939
18	$2p^4 {}^3P_0$	1416110	1422576	1415929	1419409
19	$2p^4 {}^1D_2$	1480330	1492832	1481175	1483705
20	$2p^4 {}^1S_0$	1668300	1683630	1669640	1671963
21	$2s^2 2p^2 P 3s {}^3P_0$		5741747	5726678	5727408
22	$2s^2 2p^2 P 3s {}^3P_1$	5726000	5749002	5742005	5734362
23	$2s^2 2p^2 P 3s {}^3P_2$	5786000	5808065	5787164	5795086
24	$2s^2 2p^2 P 3s {}^1P_1$	5805000	5830422	5806629	5816030
25	$2s^2 2p^2 P 3p {}^3D_1$		5893348	5893638	5879738

Table 2. Continued.

No.	Level	E(NIST)	E_{ab} (AS)	E_{fit} (AS)	E(GRASP)
26	$2s^2 2p^2 P\ 3p\ ^1P_1$		5977494	5977784	5916694
27	$2s^2 2p^2 P\ 3p\ ^3D_2$		5930946	5931236	5918275
28	$2s^2 2p^2 P\ 3p\ ^3P_0$		5949954	5950244	5937593
29	$2s^2 2p^2 P\ 3p\ ^3P_1$		5928975	5929265	5966188
30	$2s^2 2p^2 P\ 3p\ ^3D_3$		5980661	5980931	5969441
31	$2s^2 2p^2 P\ 3p\ ^3S_1$		5994329	5994619	5983123
32	$2s^2 2p^2 P\ 3p\ ^3P_2$		6000027	6000317	5988688
33	$2s^2 2p^2 P\ 3p\ ^1D_2$		6050362	6050652	6036511
34	$2s2p^2(^3P)\ ^4P\ 3s\ ^5P_1$		6070076	6070367	6068096
35	$2s^2 2p^2 P\ 3d\ ^3F_2$	6073000	6089405	6076514	6074663
36	$2s^2 2p^2 P\ 3p\ ^1S_0$		6105286	6100963	6091781
37	$2s2p^2(^3P)\ ^4P\ 3s\ ^5P_2$		6097022	6097312	6095391
38	$2s^2 2p^2 P\ 3d\ ^3F_3$		6114466	6105576	6099769
39	$2s^2 2p^2 P\ 3d\ ^1D_2:a$		6122010	6112204	6106912
40	$2s^2 2p^2 P\ 3d\ ^3D_1$	6100000	6140364	6137252	6124638
41	$2s2p^2(^3P)\ ^4P\ 3s\ ^5P_3$		6127021	6115589	6125534
42	$2s^2 2p^2 P\ 3d\ ^3F_4$		6158858	6159148	6145669
43	$2s2p^2(^3P)\ ^4P\ 3s\ ^3P_0$		6160881	6161166	6154005
44	$2s^2 2p^2 P\ 3d\ ^1D_2:b$		6122010	6112204	6154936
45	$2s^2 2p^2 P\ 3d\ ^3D_3$	6157000	6187577	6182368	6173056
46	$2s2p^2(^3P)\ ^4P\ 3s\ ^3P_1$	6174000	6182078	6176765	6176182
47	$2s^2 2p^2 P\ 3d\ ^3P_2$		6197672	6187899	6183871
48	$2s^2 2p^2 P\ 3d\ ^3P_1$		6199099	6196301	6185563
49	$2s^2 2p^2 P\ 3d\ ^3P_0$	6188000	6200763	6201012	6187517
50	$2s2p^2(^3P)\ ^4P\ 3s\ ^3P_2$	6195000	6214599	6214889	6208761
51	$2s2p^2(^3P)\ ^4P\ 3p\ ^5D_0$		6228663	6227959	6228586
52	$2s2p^2(^3P)\ ^4P\ 3p\ ^5D_1$		6230644	6230657	6230282
53	$2s^2 2p^2 P\ 3d\ ^1F_3$		6250984	6249822	6233066
54	$2s^2 2p^2 P\ 3d\ ^1P_1$		6247647	6231339	6234691
55	$2s2p^2(^3P)\ ^4P\ 3p\ ^3S_1$		6251025	6249834	6249320
56	$2s2p^2(^3P)\ ^4P\ 3p\ ^5D_2$	6226000	6249551	6235938	6250264
57	$2s2p^2(^3P)\ ^4P\ 3p\ ^5D_3$		6273475	6273762	6274627
58	$2s2p^2(^3P)\ ^4P\ 3p\ ^5P_1$	6234000	6280441	6280680	6281143
59	$2s2p^2(^3P)\ ^4P\ 3p\ ^5P_2$		6281544	6281822	6282258
60	$2s2p^2(^3P)\ ^4P\ 3p\ ^5D_4$		6301934	6302224	6303229
61	$2s2p^2(^3P)\ ^4P\ 3p\ ^5P_3$		6302997	6303373	6303696
62	$2s2p^2(^3P)\ ^4P\ 3p\ ^3D_1$		6309608	6309867	6306719
63	$2s2p^2(^3P)\ ^4P\ 3p\ ^3D_2$		6328832	6326594	6326082

Table 2. Continued.

No.	Level	E(NIST)	E_{ab} (AS)	E_{fit} (AS)	E(GRASP)
64	$2s2p^2(^1D) ^2D 3s ^3D_1$		6355744	6351092	6343261
65	$2s2p^2(^1D) ^2D 3s ^3D_2$		6358922	6359212	6346527
66	$2s2p^2(^1D) ^2D 3s ^3D_3$		6363171	6363006	6350738
67	$2s2p^2(^3P) ^4P 3p ^5S_2$		6350807	6329120	6350784
68	$2s2p^2(^3P) ^4P 3p ^3P_0$		6356557	6356034	6353947
69	$2s2p^2(^3P) ^4P 3p ^3D_3$		6359071	6360638	6356703
70	$2s2p^2(^3P) ^4P 3p ^3P_1$		6369204	6369478	6366732
71	$2s2p^2(^3P) ^4P 3p ^3P_2$		6374857	6375142	6371960
72	$2s2p^2(^1D) ^2D 3s ^1D_2$		6414931	6415220	6401195
73	$2s2p^2(^3P) ^4P 3d ^5F_1$		6403691	6403981	6402335
74	$2s2p^2(^3P) ^4P 3d ^5F_2$	6323300	6409095	6409385	6407843
75	$2s2p^2(^3P) ^4P 3d ^5F_3$		6419356	6419642	6418241
76	$2s2p^2(^3P) ^4P 3d ^5F_4$		6438472	6438762	6437440
77	$2s2p^2(^3P) ^4P 3d ^5D_0$		6449489	6448385	6449838
78	$2s2p^2(^3P) ^4P 3d ^5D_1$		6450163	6450453	6450333
79	$2s2p^2(^3P) ^4P 3d ^5D_2$		6451499	6451788	6451253
80	$2s2p^2(^3P) ^4P 3d ^5D_3$		6455729	6455984	6455234
81	$2s2p^2(^3P) ^4P 3d ^5F_5$		6462921	6463211	6461691
82	$2s2p^2(^1S) ^2S 3s ^3S_1$		6478695	6478985	6468148
83	$2s2p^2(^3P) ^4P 3d ^5D_4$		6475251	6475541	6475040
84	$2s2p^2(^3P) ^2P 3s ^3P_0$		6492936	6490852	6479653
85	$2s2p^2(^3P) ^4P 3d ^3P_2$		6483543	6483831	6480330
86	$2s2p^2(^3P) ^4P 3d ^5P_3$		6495315	6495523	6494621
87	$2s2p^2(^3P) ^4P 3d ^3F_2$		6506799	6504788	6500486
88	$2s2p^2(^1D) ^2D 3p ^3F_2$		6515149	6510532	6503533
89	$2s2p^2(^3P) ^4P 3d ^5P_2$		6504472	6504762	6503941
90	$2s2p^2(^3P) ^4P 3d ^3P_1$		6510244	6509439	6507239
91	$2s2p^2(^3P) ^4P 3d ^5P_1$		6509149	6507089	6508631
92	$2s2p^2(^1D) ^2D 3p ^3F_3$		6531204	6531606	6520173
93	$2s2p^2(^3P) ^4P 3d ^3F_3$		6526407	6515383	6520278
94	$2s2p^2(^3P) ^4P 3d ^3P_0$	6500000	6527315	6526697	6524579
95	$2s2p^2(^1D) ^2D 3p ^1D_2$		6540057	6540316	6528886
96	$2s2p^2(^1D) ^2D 3p ^3F_4$		6543104	6543394	6532562
97	$2s2p^2(^1D) ^2D 3p ^3D_1$		6546646	6546921	6535757
98	$2s2p^2(^3P) ^2P 3s ^3P_1$		6548950	6549240	6537337
99	$2s2p^2(^1D) ^2D 3p ^1F_3$	6674000	6555647	6557588	6543959
100	$2s2p^2(^1D) ^2D 3p ^3D_2$		6557312	6564823	6546739
101	$2s2p^2(^3P) ^4P 3d ^3F_4$		6554550	6554840	6548724

Table 2. Continued.

No.	Level	E(NIST)	E_{ab} (AS)	E_{fit} (AS)	E(GRASP)
102	$2s2p^2(^3P) ^2P 3s ^3P_2$		6565500	6565789	6551335
103	$2s2p^2(^1D) ^2D 3p ^3D_3$		6565719	6569280	6555082
104	$2s2p^2(^1D) ^2D 3p ^1P_1$		6569041	6578319	6557794
105	$2s2p^2(^3P) ^2P 3s ^1P_1$		6581583	6583350	6566792
106	$2s2p^2(^1S) ^2S 3s ^1S_0$		6578032	6581873	6568288
107	$2s2p^2(^1D) ^2D 3p ^3P_0$		6584368	6587912	6573693
108	$2s2p^2(^1D) ^2D 3p ^3P_1$		6587703	6588169	6577037
109	$2s2p^2(^3P) ^4P 3d ^3D_1$		6583060	6583486	6577834
110	$2s2p^2(^3P) ^4P 3d ^3D_2$		6587880	6593843	6582363
111	$2s2p^2(^1D) ^2D 3p ^3P_2$		6594511	6634065	6584159
112	$2s2p^2(^3P) ^4P 3d ^3D_3$		6593554	6594717	6587788
113	$2s2p^2(^3P) ^2P 3p ^3P_0:a$		6633798	6655454	6622129
114	$2s2p^2(^3P) ^2P 3p ^3D_1$		6655212	6669332	6643916
115	$2s2p^2(^3P) ^2P 3p ^3D_2$		6669119	6669376	6658714
116	$2s2p^2(^3P) ^2P 3p ^3P_1$		6670171	6670339	6660018
117	$2s2p^2(^1D) ^2D 3d ^3G_3$		6700514	6700804	6687925
118	$2s2p^2(^3P) ^2P 3p ^1S_0$		6699942	6700164	6690409
119	$2s2p^2(^1D) ^2D 3d ^3G_4$		6705961	6706251	6693160
120	$2s2p^2(^1D) ^2D 3d ^3G_5$		6712503	6712793	6699723
121	$2s2p^2(^1D) ^2D 3d ^3F_2$		6718777	6719067	6703787
122	$2s2p^2(^1D) ^2D 3d ^3F_3$		6722518	6722808	6707516
123	$2s2p^2(^1D) ^2D 3d ^3F_4$		6725204	6725494	6709918
124	$2s2p^2(^1S) ^2S 3p ^1P_1$		6723434	6723640	6713721
125	$2s2p^2(^1D) ^2D 3d ^3D_1$		6724936	6725226	6713897
126	$2s2p^2(^1S) ^2S 3p ^3P_2$		6725654	6725867	6716788
127	$2s2p^2(^1D) ^2D 3d ^3D_2$		6728114	6728404	6717197
128	$2s2p^2(^3P) ^2P 3p ^3D_3$		6730742	6731273	6718506
129	$2s2p^2(^1D) ^2D 3d ^3D_3$		6730983	6734379	6719585
130	$2s2p^2(^1D) ^2D 3d ^1F_3$		6743017	6743307	6730355
131	$2s2p^2(^3P) ^2P 3p ^3P_2$		6725654	6725867	6730377
132	$2s2p^2(^3P) ^2P 3p ^3S_1$		6741704	6741964	6731167
133	$2s2p^2(^3P) ^2P 3p ^3P_0:b$		6742834	6742515	6731869
134	$2s2p^2(^1S) ^2S 3p ^3P_1$		6745641	6745885	6736397
135	$2s2p^2(^1D) ^2D 3d ^1G_4$		6760536	6760826	6745195
136	$2s2p^2(^1D) ^2D 3d ^3P_0$		6759391	6759566	6745372
137	$2s2p^2(^1D) ^2D 3d ^3P_1$		6761523	6761813	6747918
138	$2s2p^2(^1D) ^2D 3d ^3P_2$		6763993	6764281	6750371
139	$2s2p^2(^1D) ^2D 3d ^3S_1$		6773976	6774266	6762330

Table 2. Continued.

No.	Level	E(NIST)	E_{ab} (AS)	E_{fit} (AS)	E(GRASP)
140	$2s2p^2(^1D) 2D 3d ^1D_2$		6786475	6786751	6770475
141	$2s2p^2(^1D) 2D 3d ^1P_1$		6791180	6791470	6778053
142	$2s2p^2(^3P) 2P 3p ^1D_2$		6795469	6795742	6778329
143	$2p^3(^4S) 3s ^5S_2$		6791745	6792010	6797008
144	$2s2p^2(^1D) 2D 3d ^1S_0$		6828378	6828554	6811372
145	$2s2p^2(^3P) 2P 3p ^1P_1$		6832720	6832844	6816537
146	$2s2p^2(^3P) 2P 3d ^3F_2$		6836989	6837279	6822060
147	$2s2p^2(^3P) 2P 3d ^3F_3$		6897901	6898190	6827253
148	$2s2p^2(^1S) 2S 3d ^3D_1$		6840140	6840430	6827349
149	$2s2p^2(^1S) 2S 3d ^3D_2$		6855839	6856129	6842158
150	$2p^3(^4S) 3s ^3S_1$		6890278	6890499	6885290
151	$2s2p^2(^1S) 2S 3d ^3D_3$		6923450	6923739	6885411
152	$2s2p^2(^3P) 2P 3d ^3F_4$		6901606	6901896	6885667
153	$2s2p^2(^3P) 2P 3d ^3D_2$		6912061	6912351	6898769
154	$2s2p^2(^3P) 2P 3d ^1P_1$		6912138	6912428	6898869
155	$2s2p^2(^3P) 2P 3d ^3D_3$		6923450	6923739	6907325
156	$2s2p^2(^3P) 2P 3d ^3D_1$		6927015	6927305	6912222
157	$2s2p^2(^1S) 2S 3d ^1D_2$		6928253	6928542	6915637
158	$2s2p^2(^3P) 2P 3d ^3P_2$		6940380	6940669	6924457
159	$2s2p^2(^3P) 2P 3d ^3P_0$		6953789	6953815	6935785
160	$2s2p^2(^3P) 2P 3d ^3P_1$		6954920	6955208	6936294
161	$2p^3(^2D) 3s ^3D_1$		6950261	6950503	6940370
162	$2p^3(^2D) 3s ^3D_2$		6951940	6952169	6941806
163	$2p^3(^4S) 3p ^5P_1$		6943746	6944036	6950681
164	$2s2p^2(^3P) 2P 3d ^1F_3$		6971686	6971976	6950784
165	$2p^3(^2D) 3s ^3D_3$		6962318	6962641	6952252
166	$2p^3(^4S) 3p ^5P_2$		6950971	6951261	6954357
167	$2p^3(^4S) 3p ^5P_3$		6959208	6959440	6965811
168	$2p^3(^2D) 3s ^1D_2$		6992832	6993090	6981197
169	$2s2p^2(^3P) 2P 3d ^1D_2$		7018949	7019237	6992640
170	$2p^3(^4S) 3p ^3P_1$		6999757	7000047	7001672
171	$2p^3(^4S) 3p ^3P_2$		7003762	7004051	7009236
172	$2p^3(^4S) 3p ^3P_0$		7010694	7010775	7013325
173	$2p^3(^2D) 3p ^3D_1$		7074853	7075143	7067415
174	$2p^3(^2P) 3s ^3P_0$		7083881	7084124	7074533
175	$2p^3(^2P) 3s ^3P_1$		7090002	7089744	7080633
176	$2p^3(^2D) 3p ^3D_2$		7090247	7090537	7081966
177	$2p^3(^2D) 3p ^3D_3$		7101254	7101544	7092984

Table 2. Continued.

No.	Level	E(NIST)	E_{ab} (AS)	E_{fit} (AS)	E(GRASP)
178	$2p^3(^3D) 3p ^3F_2$		7104662	7104952	7095870
179	$2p^3(^2P) 3s ^3P_2$		7110085	7109885	7101083
180	$2p^3(^3D) 3p ^1P_1$		7109363	7109653	7102443
181	$2p^3(^3D) 3p ^3F_3$		7115091	7115381	7106652
182	$2p^3(^3D) 3p ^1F_3$		7123559	7123849	7113829
183	$2p^3(^3D) 3p ^3F_4$		7124032	7124322	7115274
184	$2p^3(^3S) 3d ^5D_0$		7118129	7118419	7123530
185	$2p^3(^3S) 3d ^5D_1$		7118329	7118615	7123677
186	$2p^3(^3S) 3d ^5D_2$		7118574	7118849	7123824
187	$2p^3(^3S) 3d ^5D_3$		7118952	7119232	7124015
188	$2p^3(^3S) 3d ^5D_4$		7120699	7120989	7125760
189	$2p^3(^2P) 3s ^1P_1$		7137295	7137044	7127552
190	$2p^3(^3D) 3p ^3P_0$		7179087	7179371	7167848
191	$2p^3(^3D) 3p ^3P_1$		7186048	7186337	7176347
192	$2p^3(^3S) 3d ^3D_2$		7178450	7178719	7177011
193	$2p^3(^3D) 3p ^3P_2$		7192508	7192797	7182120
194	$2p^3(^3S) 3d ^3D_3$		7188146	7188428	7187396
195	$2p^3(^3S) 3d ^3D_1$		7188421	7188703	7187939
196	$2p^3(^3D) 3p ^1D_2$		7224525	7224812	7211136
197	$2p^3(^2P) 3p ^3D_1$		7235122	7235412	7225340
198	$2p^3(^2P) 3p ^3S_1$		7248516	7248806	7241695
199	$2p^3(^3D) 3d ^3F_2$		7251687	7251937	7243328
200	$2p^3(^2P) 3p ^3D_2$		7252630	7252920	7243842
201	$2p^3(^3D) 3d ^3F_3$		7258935	7259219	7250333
202	$2p^3(^3D) 3d ^3G_4$		7267143	7267433	7258224
203	$2p^3(^3D) 3d ^1S_0$		7267287	7267577	7258336
204	$2p^3(^3D) 3d ^3G_3$		7269033	7269312	7260016
205	$2p^3(^2P) 3p ^3D_3$		7268773	7269062	7260930
206	$2p^3(^2P) 3p ^1P_1$		7274720	7275010	7265566
207	$2p^3(^3D) 3d ^3F_4$		7276654	7276944	7267758
208	$2p^3(^3D) 3d ^3G_5$		7281367	7281657	7272356
209	$2p^3(^3D) 3d ^1G_4$		7284361	7284651	7274780
210	$2p^3(^2P) 3p ^3P_0$		7293324	7293601	7282919
211	$2p^3(^3D) 3d ^3D_1$		7290736	7290979	7283196
212	$2p^3(^2P) 3p ^3P_1$		7300121	7300411	7290418
213	$2p^3(^2P) 3p ^3P_2$		7304161	7304451	7295131
214	$2p^3(^2P) 3p ^1D_2$		7323328	7323616	7310062
215	$2p^3(^3D) 3d ^3D_2$		7318862	7319113	7310196

Table 2. Continued.

No.	Level	E(NIST)	E_{ab} (AS)	E_{fit} (AS)	E(GRASP)
216	$2p^3({}^3D) 3d {}^1P_1$		7319556	7319836	7311015
217	$2p^3({}^3D) 3d {}^3D_3$		7326383	7326665	7315245
218	$2p^3({}^3D) 3d {}^3P_2$		7332437	7332706	7324495
219	$2p^3({}^3D) 3d {}^3P_0$		7334573	7334863	7326757
220	$2p^3({}^3D) 3d {}^3P_1$		7337715	7337987	7329772
221	$2p^3({}^3D) 3d {}^1D_2$		7348934	7349205	7337502
222	$2p^3({}^3D) 3d {}^3S_1$		7359484	7359750	7346647
223	$2p^3({}^3D) 3d {}^1F_3$		7380513	7381084	7366579
224	$2p^3({}^2P) 3d {}^3F_2$		7411647	7411611	7402549
225	$2p^3({}^2P) 3d {}^3F_3$		7416885	7417141	7407777
226	$2p^3({}^2P) 3p {}^1S_0$		7427895	7428172	7409852
227	$2p^3({}^2P) 3d {}^3F_4$		7426969	7427259	7418490
228	$2p^3({}^2P) 3d {}^3P_2$		7436573	7436651	7427040
229	$2p^3({}^2P) 3d {}^3P_0$		7436818	7437108	7430308
230	$2p^3({}^2P) 3d {}^3P_1$		7439845	7440051	7431960
231	$2p^3({}^2P) 3d {}^1D_2$		7486657	7486822	7440360
232	$2p^3({}^2P) 3d {}^3D_1$		7465372	7465633	7452683
233	$2p^3({}^2P) 3d {}^3D_3$		7466444	7466518	7456489
234	$2p^3({}^2P) 3d {}^3D_2$		7451816	7451960	7472850
235	$2p^3({}^2P) 3d {}^1F_3$		7493789	7493772	7478909
236	$2p^3({}^2P) 3d {}^1P_1$		7561443	7561290	7543791
237	$2s^2 2p^2 P 4s {}^3P_0$		7795381	7795670	7749456
238	$2s^2 2p^2 P 4s {}^3P_1$		7797987	7798268	7752082
239	$2s^2 2p^2 P 4p {}^3D_1$		7858690	7858980	7812720
240	$2s^2 2p^2 P 4s {}^3P_2$		7863544	7863823	7817484
241	$2s^2 2p^2 P 4s {}^1P_1$		7869822	7870105	7823822
242	$2s^2 2p^2 P 4p {}^3P_1$		7873758	7874048	7828846
243	$2s^2 2p^2 P 4p {}^3D_2$		7875543	7875833	7830393
244	$2s^2 2p^2 P 4p {}^3P_0$		7880856	7881146	7836188
245	$2s^2 2p^2 P 4d {}^3F_2$		7931974	7932255	7885404
246	$2s^2 2p^2 P 4p {}^1P_1$		7931877	7932167	7886477
247	$2s^2 2p^2 P 4p {}^3D_3$		7934743	7935033	7889498
248	$2s^2 2p^2 P 4p {}^3P_2$		7938902	7939192	7893544
249	$2s^2 2p^2 P 4p {}^3S_1$		7939643	7939933	7894058
250	$2s^2 2p^2 P 4d {}^3P_{2;a}$		8013799	8014088	7898263
251	$2s^2 2p^2 P 4d {}^3F_3$		7944931	7945220	7898372
252	$2s^2 2p^2 P 4d {}^3D_1$		7950293	7950582	7904345
253	$2s^2 2p^2 P 4p {}^1D_2$		7955151	7955441	7909857

Table 2. Continued.

No.	Level	E(NIST)	E_{ab} (AS)	E_{fit} (AS)	E(GRASP)
254	$2s^2 2p^2 P$ 4p 1S_0		7974259	7974549	7928738
255	$2s^2 2p^2 P$ 4f 3G_3		7980672	7980962	7937815
256	$2s^2 2p^2 P$ 4f 3F_2		7982863	7983153	7939610
257	$2s^2 2p^2 P$ 4f 3G_4		7982588	7982878	7939891
258	$2s^2 2p^2 P$ 4d 3F_4		8001725	8002015	7955060
259	$2s^2 2p^2 P$ 4d 1D_2		8003031	8003319	7956528
260	$2s^2 2p^2 P$ 4d 3D_3		8009038	8009327	7962650
261	$2s^2 2p^2 P$ 4d $^3P_2:b$		8013799	8014088	7967552
262	$2s^2 2p^2 P$ 4d 3P_1		8014529	8014819	7968190
263	$2s^2 2p^2 P$ 4d 3P_0		8015398	8015688	7968989
264	$2s^2 2p^2 P$ 4d 1F_3		8030100	8030388	7982900
265	$2s^2 2p^2 P$ 4d 1P_1		8031033	8031320	7985215
266	$2s^2 2p^2 P$ 4f 3F_4		8047872	8048162	8005173
267	$2s^2 2p^2 P$ 4f 3D_2		8050954	8051244	8007598
268	$2s^2 2p^2 P$ 4f 3D_1		8055435	8055725	8012289
269	$2s^2 2p^2 P$ 4f 1D_2		8057313	8057603	8013991
270	$2s 2p^2(^3P)$ 4P 4s 3P_0		8111191	8111481	8109236
271	$2s 2p^2(^3P)$ 4P 4p 5D_0		8152227	8152517	8151980
272	$2s 2p^2(^3P)$ 4P 4p 5D_1		8153548	8153838	8152944
273	$2s 2p^2(^3P)$ 4P 4p $^5D_2:a$		8162997	8163287	8163322
274	$2s 2p^2(^3P)$ 4P 4p 3S_1		8176073	8176363	8174042
275	$2s 2p^2(^3P)$ 4P 4p 5P_1		8183623	8183913	8183504
276	$2s 2p^2(^3P)$ 4P 4p 5D_3		8187668	8187958	8188402
277	$2s 2p^2(^3P)$ 4P 4p $^5D_2:b$		8162997	8163287	8189522
278	$2s 2p^2(^3P)$ 4P 4p 3D_1		8199262	8199552	8198102
279	$2s 2p^2(^3P)$ 4P 4p 3D_2		8208095	8208385	8207330
280	$2s 2p^2(^3P)$ 4P 4p 5P_3		8216544	8216834	8217080
281	$2s 2p^2(^3P)$ 4P 4p 3P_0		8218277	8218564	8217719
282	$2s 2p^2(^3P)$ 4P 4p 5D_4		8217578	8217868	8218590
283	$2s 2p^2(^3P)$ 4P 4p 5S_2		8226239	8226529	8227146
284	$2s 2p^2(^3P)$ 4P 4p 3P_1		8239826	8240116	8238638
285	$2s 2p^2(^3P)$ 4P 4p 3D_3		8239693	8239983	8239229
286	$2s 2p^2(^3P)$ 4P 4p 3P_2		8245703	8245993	8244974
287	$2s 2p^2(^3P)$ 4P 4d 5D_0		8253408	8253698	8254194
288	$2s 2p^2(^3P)$ 4P 4f 5G_2		8267517	8267807	8267688
289	$2s 2p^2(^3P)$ 4P 4f $^5G_3:a$		8268250	8268540	8268616
290	$2s 2p^2(^3P)$ 4P 4f 5D_4		8269290	8269580	8270118
291	$2s 2p^2(^3P)$ 4P 4f $^3G_3:a$		8272585	8272875	8272482

Table 2. Continued.

No.	Level	E(NIST)	E_{ab} (AS)	E_{fit} (AS)	E(GRASP)
292	$2s2p^2(^3P) ^4P 4f ^5G_{3:b}$		8268250	8268540	8295909
293	$2s2p^2(^3P) ^4P 4f ^5G_4$		8295260	8295550	8296354
294	$2s2p^2(^3P) ^4P 4f ^5F_2$		8297149	8297439	8297743
295	$2s2p^2(^3P) ^4P 4f ^5G_5$		8298122	8298412	8299557
296	$2s2p^2(^3P) ^4P 4f ^3G_{3:b}$		8272585	8272875	8299785
297	$2s2p^2(^3P) ^4P 4f ^5F_1$		8300261	8300551	8301019
298	$2s2p^2(^3P) ^4P 4f ^3G_4$		8301129	8301419	8301612
299	$2s2p^2(^3P) ^4P 4f ^3F_2$		8304031	8304321	8304478
300	$2s2p^2(^3P) ^4P 4f ^5D_0$		8327198	8327488	8328229
301	$2s2p^2(^3P) ^4P 4f ^5D_1$		8328019	8328309	8328907
302	$2s2p^2(^3P) ^4P 4f ^5G_6$		8327343	8327633	8330148
303	$2s2p^2(^3P) ^4P 4f ^5D_2$		8329593	8329883	8330524
304	$2s2p^2(^3P) ^4P 4f ^3G_5$		8333112	8333402	8331132
305	$2s2p^2(^3P) ^4P 4f ^5F_3$		8331046	8331336	8332023
306	$2s2p^2(^3P) ^4P 4f ^3D_1$		8331600	8331890	8332356
307	$2s2p^2(^3P) ^4P 4f ^5F_4$		8331715	8332005	8333061
308	$2s2p^2(^3P) ^4P 4f ^5F_5$		8329609	8329899	8334663
309	$2s2p^2(^3P) ^4P 4f ^3D_2$		8334495	8334785	8335018
310	$2s2p^2(^3P) ^4P 4f ^3F_3$		8336429	8336719	8336780
311	$2s2p^2(^3P) ^4P 4f ^3F_4$		8336641	8336931	8337257
312	$2s2p^2(^1D) ^2D 4p ^3F_2$		8432436	8432725	8422797
313	$2s2p^2(^1D) ^2D 4p ^3F_3$		8439354	8439644	8430659
314	$2s2p^2(^1D) ^2D 4p ^3D_1$		8439923	8440213	8431188
315	$2s2p^2(^1D) ^2D 4p ^3D_2$		8443704	8443994	8434788
316	$2s2p^2(^1D) ^2D 4p ^3F_4$		8446787	8447077	8438803
317	$2s2p^2(^1D) ^2D 4p ^1D_2$		8450342	8450632	8439411
318	$2s2p^2(^1D) ^2D 4p ^1F_3$		8449473	8449772	8439531
319	$2s2p^2(^1D) ^2D 4p ^3D_3$		8448117	8448416	8440871
320	$2s2p^2(^1D) ^2D 4p ^3P_1$		8453637	8453926	8443308
321	$2s2p^2(^1D) ^2D 4p ^3P_0$		8453845	8454128	8443942
322	$2s2p^2(^1D) ^2D 4p ^3P_2$		8463127	8463416	8453012
323	$2s2p^2(^1D) ^2D 4p ^1P_1$		8464465	8464754	8453409
324	$2s2p^2(^1D) ^2D 4f ^3G_3$		8539625	8539915	8532346
325	$2s2p^2(^1D) ^2D 4f ^3G_4$		8540911	8541201	8534340
326	$2s2p^2(^1D) ^2D 4f ^3F_2$		8543073	8543360	8535458
327	$2s2p^2(^1D) ^2D 4f ^3F_3$		8544386	8544676	8537297
328	$2s2p^2(^1D) ^2D 4f ^3H_4$		8545576	8545866	8538613
329	$2s2p^2(^1D) ^2D 4f ^3G_5$		8545639	8545929	8541462

Table 2. Continued.

No.	Level	E(NIST)	E_{ab} (AS)	E_{fit} (AS)	E(GRASP)
330	$2s2p^2(^1_0S) ^2S 4p ^3P_0$		8550727	8551016	8541948
331	$2s2p^2(^1_2D) ^2D 4f ^3F_4$		8549385	8549675	8542672
332	$2s2p^2(^1_2D) ^2D 4f ^1F_3$		8550932	8551223	8543483
333	$2s2p^2(^1_2D) ^2D 4f ^3D_1$		8551576	8551866	8543758
334	$2s2p^2(^1_2D) ^2D 4f ^1G_4$		8551605	8551895	8544719
335	$2s2p^2(^1_2D) ^2D 4f ^3D_2$		8552597	8552883	8545004
336	$2s2p^2(^1_2D) ^2D 4f ^3H_5$		8551201	8551491	8546910
337	$2s2p^2(^3_3P) ^2P 4p ^3D_1:a$		8629504	8629794	8548860
338	$2s2p^2(^1_2D) ^2D 4f ^3D_3$		8556110	8556398	8548931
339	$2s2p^2(^1_2D) ^2D 4f ^1D_2$		8557008	8557297	8549291
340	$2s2p^2(^1_2D) ^2D 4f ^1H_5$		8557193	8557483	8552539
341	$2s2p^2(^1_2D) ^2D 4f ^3P_2$		8561243	8561531	8554302
342	$2s2p^2(^1_2D) ^2D 4f ^3P_1$		8562383	8562670	8554490
343	$2s2p^2(^1_2D) ^2D 4f ^3H_6$		8556169	8556459	8556266
344	$2s2p^2(^1_2D) ^2D 4f ^3P_0$		8564100	8564390	8556516
345	$2s2p^2(^1_0S) ^2S 4p ^3P_2:a$		8564356	8564643	8557699
346	$2s2p^2(^1_2D) ^2D 4f ^1P_1:a$		8565732	8566017	8557866
347	$2s2p^2(^1_2D) ^2D 4f ^1P_1:b$		8565732	8566017	8559474
348	$2s2p^2(^3_3P) ^2P 4p ^1S_0$		8622972	8623260	8617089
349	$2s2p^2(^3_3P) ^2P 4p ^3D_1:b$		8629504	8629794	8622145
350	$2s2p^2(^1_0S) ^2S 4p ^3P_2:b$		8649315	8649603	8624138
351	$2s2p^2(^3_3P) ^2P 4p ^3P_1$		8638664	8638953	8629689
352	$2s2p^2(^3_3P) ^2P 4p ^3P_2$		8649315	8649603	8633308
353	$2s2p^2(^3_3P) ^2P 4p ^3D_3$		8646398	8646687	8633453
354	$2s2p^2(^3_3P) ^2P 4p ^1D_2$		8660102	8660392	8647410
355	$2s2p^2(^3_3P) ^2P 4f ^3G_3$		8736401	8736690	8660666
356	$2s2p^2(^1_0S) ^2S 4f ^3F_4:a$		8665287	8665577	8662200
357	$2s2p^2(^1_0S) ^2S 4f ^1F_3$		8666624	8666913	8662705
358	$2s2p^2(^1_0S) ^2S 4f ^3F_3$		8758923	8759212	8732041
359	$2s2p^2(^1_0S) ^2S 4f ^3F_4:b$		8760381	8760671	8733179
360	$2s2p^2(^3_3P) ^2P 4f ^1G_4$		8753252	8753542	8744359
361	$2s2p^2(^3_3P) ^2P 4f ^3G_5$		8752933	8753223	8745053

In Tab. 2, we present the calculated energy levels and compared to the NIST database values. There are only 34 energy levels in the NIST database and the corresponding *ab initio* and fitted AS values and GRASP values differ from the NIST values by 0.81 % , 0.25 % and 0.31 % respectively. For all 361 energy

levels calculated by the TFDA and the MCDHF methods, the average difference between them is only 0.19 %.

Table 3. Lifetimes (τ_l in s. in the length form) calculated by AS code $\tau_l(AS)$ and by GRASP2018 code $\tau_l(GRASP)$ for *V XVIII*

No.	Level	$\tau_l(GRASP)$	$\tau_l(AS)$
1	$2s^2 2p^2 P 3s \ ^3P_0$	8.147E-13	8.246E-13
2	$2s^2 2p^2 P 3s \ ^3P_1$	7.090E-13	7.325E-13
3	$2s^2 2p^2 P 3s \ ^3P_2$	7.773E-13	8.102E-13
4	$2s^2 2p^2 P 3s \ ^1P_1$	5.094E-13	5.243E-13
5	$2s^2 2p^2 P 3p \ ^3D_1$	3.581E-11	2.963E-11
6	$2s^2 2p^2 P 3p \ ^1P_1$	1.344E-11	7.594E-12
7	$2s^2 2p^2 P 3p \ ^3D_2$	2.643E-11	2.227E-11
8	$2s^2 2p^2 P 3p \ ^3P_0$	5.564E-12	4.513E-12
9	$2s^2 2p^2 P 3p \ ^3P_1$	9.245E-12	1.092E-11
10	$2s^2 2p^2 P 3p \ ^3D_3$	3.189E-11	2.719E-11
11	$2s^2 2p^2 P 3p \ ^3S_1$	7.738E-12	6.269E-12
12	$2s^2 2p^2 P 3p \ ^3P_2$	6.233E-12	4.996E-12
13	$2s^2 2p^2 P 3p \ ^1D_2$	1.283E-11	1.135E-11
14	$2s 2p^2(^3P) \ ^4P 3s \ ^5P_1$	1.076E-12	1.100E-12
15	$2s^2 2p^2 P 3d \ ^3F_2$	7.397E-13	1.053E-12
16	$2s^2 2p^2 P 3p \ ^1S_0$	4.580E-12	3.896E-12
17	$2s 2p^2(^3P) \ ^4P 3s \ ^5P_2$	1.042E-12	1.074E-12
18	$2s^2 2p^2 P 3d \ ^3F_3$	4.029E-13	3.183E-13
19	$2s^2 2p^2 P 3d \ ^1D_{2a}$	1.386E-13	1.269E-13
20	$2s^2 2p^2 P 3d \ ^3D_1$	7.826E-14	7.927E-14
21	$2s 2p^2(^3P) \ ^4P 3s \ ^5P_3$	9.827E-13	1.078E-12
22	$2s^2 2p^2 P 3d \ ^3F_4$	8.721E-10	8.278E-10
23	$2s 2p^2(^3P) \ ^4P 3s \ ^3P_0$	6.832E-13	7.158E-13
24	$2s^2 2p^2 P 3d \ ^1D_{2b}$	1.277E-13	1.269E-13
25	$2s^2 2p^2 P 3d \ ^3D_3$	8.248E-14	8.720E-14
26	$2s 2p^2(^3P) \ ^4P 3s \ ^3P_1$	6.260E-13	6.448E-13
27	$2s^2 2p^2 P 3d \ ^3P_2$	9.776E-14	1.010E-13
28	$2s^2 2p^2 P 3d \ ^3P_1$	1.078E-13	1.051E-13
29	$2s^2 2p^2 P 3d \ ^3P_0$	1.259E-13	1.243E-13
30	$2s 2p^2(^3P) \ ^4P 3s \ ^3P_2$	6.142E-13	6.324E-13
31	$2s 2p^2(^3P) \ ^4P 3p \ ^5D_0$	1.578E-10	3.426E-10
32	$2s 2p^2(^3P) \ ^4P 3p \ ^5D_1$	9.416E-13	2.254E-13
33	$2s^2 2p^2 P 3d \ ^1F_3$	5.733E-14	5.773E-14
34	$2s^2 2p^2 P 3d \ ^1P_1$	9.543E-14	1.360E-13

Table 3. Continued.

No.	Level	$\tau_l(GRASP)$	$\tau_l(AS)$
35	$2s2p^2(\frac{3}{2}P) 4P 3p {}^3S_1$	5.074E-13	4.956E-13
36	$2s2p^2(\frac{3}{2}P) 4P 3p {}^5D_2$	2.270E-10	2.284E-10
37	$2s2p^2(\frac{3}{2}P) 4P 3p {}^5D_3$	1.662E-10	1.120E-10
38	$2s2p^2(\frac{3}{2}P) 4P 3p {}^5P_1$	9.980E-13	9.738E-13
39	$2s2p^2(\frac{3}{2}P) 4P 3p {}^5P_2$	4.438E-12	5.307E-12
40	$2s2p^2(\frac{3}{2}P) 4P 3p {}^5D_4$	6.430E-10	4.333E-10
41	$2s2p^2(\frac{3}{2}P) 4P 3p {}^5P_3$	2.856E-12	3.599E-12
42	$2s2p^2(\frac{3}{2}P) 4P 3p {}^3D_1$	3.021E-13	2.871E-13
43	$2s2p^2(\frac{3}{2}P) 4P 3p {}^3D_2$	3.092E-13	2.948E-13
44	$2s2p^2(\frac{1}{2}D) {}^2D 3s {}^3D_1$	5.347E-13	5.264E-13
45	$2s2p^2(\frac{1}{2}D) {}^2D 3s {}^3D_2$	5.334E-13	5.256E-13
46	$2s2p^2(\frac{1}{2}D) {}^2D 3s {}^3D_3$	5.142E-13	5.114E-13
47	$2s2p^2(\frac{3}{2}P) 4P 3p {}^5S_2$	7.317E-12	9.195E-12
48	$2s2p^2(\frac{3}{2}P) 4P 3p {}^3P_0$	3.010E-13	3.029E-13
49	$2s2p^2(\frac{3}{2}P) 4P 3p {}^3D_3$	3.229E-13	3.057E-13
50	$2s2p^2(\frac{3}{2}P) 4P 3p {}^3P_1$	2.954E-13	2.895E-13
51	$2s2p^2(\frac{3}{2}P) 4P 3p {}^3P_2$	3.083E-13	2.993E-13
52	$2s2p^2(\frac{1}{2}D) {}^2D 3s {}^1D_2$	1.132E-12	1.096E-12
53	$2s2p^2(\frac{3}{2}P) 4P 3d {}^5F_1$	1.142E-11	1.126E-11
54	$2s2p^2(\frac{3}{2}P) 4P 3d {}^5F_2$	3.905E-12	3.867E-12
55	$2s2p^2(\frac{3}{2}P) 4P 3d {}^5F_3$	1.648E-12	1.618E-12
56	$2s2p^2(\frac{3}{2}P) 4P 3d {}^5F_4$	1.696E-11	1.839E-11
57	$2s2p^2(\frac{3}{2}P) 4P 3d {}^5D_0$	6.379E-12	2.805E-12
58	$2s2p^2(\frac{3}{2}P) 4P 3d {}^5D_1$	1.146E-12	1.194E-12
59	$2s2p^2(\frac{3}{2}P) 4P 3d {}^5D_2$	4.356E-13	4.541E-13
60	$2s2p^2(\frac{3}{2}P) 4P 3d {}^5D_3$	2.253E-13	2.310E-13
61	$2s2p^2(\frac{3}{2}P) 4P 3d {}^5F_5$	1.104E-09	1.029E-09
62	$2s2p^2(\frac{1}{0}S) {}^2S 3s {}^3S_1$	5.928E-13	5.799E-13
63	$2s2p^2(\frac{3}{2}P) 4P 3d {}^5D_4$	5.981E-10	6.915E-10
64	$2s2p^2(\frac{3}{2}P) {}^2P 3s {}^3P_0$	6.013E-13	7.158E-13
65	$2s2p^2(\frac{3}{2}P) 4P 3d {}^3P_2$	2.100E-13	2.022E-13
66	$2s2p^2(\frac{3}{2}P) 4P 3d {}^5P_3$	9.302E-14	9.035E-14
67	$2s2p^2(\frac{3}{2}P) 4P 3d {}^3F_2$	1.972E-13	1.893E-13
68	$2s2p^2(\frac{1}{2}D) {}^2D 3p {}^3F_2$	7.139E-13	7.233E-13
69	$2s2p^2(\frac{3}{2}P) 4P 3d {}^5P_2$	7.559E-14	7.408E-14
70	$2s2p^2(\frac{3}{2}P) 4P 3d {}^3P_1$	1.729E-13	1.364E-13
71	$2s2p^2(\frac{3}{2}P) 4P 3d {}^5P_1$	6.909E-14	7.538E-14
72	$2s2p^2(\frac{1}{2}D) {}^2D 3p {}^3F_3$	6.413E-12	8.862E-12

Table 3. Continued.

No.	Level	$\tau_l(GRASP)$	$\tau_l(AS)$
73	$2s2p^2(^3P) 4P 3d ^3F_3$	2.029E-13	1.942E-13
74	$2s2p^2(^3P) 4P 3d ^3P_0$	2.042E-13	3.095E-13
75	$2s2p^2(^1D) ^2D 3p ^1D_2$	3.421E-13	3.345E-13
76	$2s2p^2(^1D) ^2D 3p ^3F_4$	1.817E-10	1.701E-10
77	$2s2p^2(^1D) ^2D 3p ^3D_1$	6.621E-13	6.871E-13
78	$2s2p^2(^3P) ^2P 3s ^3P_1$	6.664E-13	6.660E-13
79	$2s2p^2(^1D) ^2D 3p ^1F_3$	2.739E-13	2.256E-13
80	$2s2p^2(^1D) ^2D 3p ^3D_2$	1.978E-12	1.903E-12
81	$2s2p^2(^3P) 4P 3d ^3F_4$	2.011E-13	1.941E-13
82	$2s2p^2(^3P) ^2P 3s ^3P_2$	7.563E-13	7.215E-13
83	$2s2p^2(^1D) ^2D 3p ^3D_3$	1.394E-12	7.735E-13
84	$2s2p^2(^1D) ^2D 3p ^1P_1$	2.620E-13	2.524E-13
85	$2s2p^2(^3P) ^2P 3s ^1P_1$	3.369E-13	2.763E-13
86	$2s2p^2(^1S) ^2S 3s ^1S_0$	9.777E-13	9.234E-13
87	$2s2p^2(^1D) ^2D 3p ^3P_0$	4.036E-12	4.776E-12
88	$2s2p^2(^1D) ^2D 3p ^3P_1$	1.951E-12	1.908E-12
89	$2s2p^2(^3P) 4P 3d ^3D_1$	1.323E-13	1.363E-13
90	$2s2p^2(^3P) 4P 3d ^3D_2$	1.319E-13	1.265E-13
91	$2s2p^2(^1D) ^2D 3p ^3P_2$	1.256E-12	1.285E-12
92	$2s2p^2(^3P) 4P 3d ^3D_3$	1.172E-13	1.122E-13
93	$2s2p^2(^3P) ^2P 3p ^3P_{0a}$	1.254E-12	1.277E-12
94	$2s2p^2(^3P) ^2P 3p ^3D_1$	8.528E-13	8.534E-13
95	$2s2p^2(^3P) ^2P 3p ^3D_2$	1.891E-12	1.903E-12
96	$2s2p^2(^3P) ^2P 3p ^3P_1$	7.336E-13	6.853E-13
97	$2s2p^2(^1D) ^2D 3d ^3G_3$	9.146E-12	1.000E-11
98	$2s2p^2(^3P) ^2P 3p ^1S_0$	3.905E-12	4.538E-12
99	$2s2p^2(^1D) ^2D 3d ^3G_4$	1.430E-12	1.889E-12
100	$2s2p^2(^1D) ^2D 3d ^3G_5$	2.761E-10	2.600E-10
101	$2s2p^2(^1D) ^2D 3d ^3F_2$	7.954E-14	7.758E-14
102	$2s2p^2(^1D) ^2D 3d ^3F_3$	8.212E-14	8.076E-14
103	$2s2p^2(^1D) ^2D 3d ^3F_4$	8.064E-14	7.720E-14
104	$2s2p^2(^1S) ^2S 3p ^1P_1$	3.932E-13	3.921E-13
105	$2s2p^2(^1D) ^2D 3d ^3D_1$	8.086E-14	7.919E-14
106	$2s2p^2(^1S) ^2S 3p ^3P_2$	2.022E-12	1.836E-12
107	$2s2p^2(^1D) ^2D 3d ^3D_2$	8.141E-14	7.982E-14
108	$2s2p^2(^3P) ^2P 3p ^3D_3$	1.016E-12	7.735E-13
109	$2s2p^2(^1D) ^2D 3d ^3D_3$	1.130E-13	9.191E-14
110	$2s2p^2(^1D) ^2D 3d ^1F_3$	1.622E-13	1.760E-13

Table 3. Continued.

No.	Level	$\tau_l(GRASP)$	$\tau_l(AS)$
111	$2s2p^2(^3P) 2P 3p ^3P_2$	9.197E-13	9.316E-13
112	$2s2p^2(^3P) 2P 3p ^3S_1$	5.032E-13	4.956E-13
113	$2s2p^2(^3P) 2P 3p ^3P_{0b}$	2.835E-12	2.341E-12
114	$2s2p^2(^1S) 2S 3p ^3P_1$	7.738E-13	6.853E-13
115	$2s2p^2(^1D) 2D 3d ^1G_4$	5.452E-13	5.450E-13
116	$2s2p^2(^1D) 2D 3d ^3P_0$	9.886E-14	9.521E-14
117	$2s2p^2(^1D) 2D 3d ^3P_1$	1.980E-13	9.681E-14
118	$2s2p^2(^1D) 2D 3d ^3P_2$	1.024E-13	9.965E-14
119	$2s2p^2(^1D) 2D 3d ^3S_1$	1.464E-13	1.370E-13
120	$2s2p^2(^1D) 2D 3d ^1D_2$	9.973E-14	9.658E-14
121	$2s2p^2(^1D) 2D 3d ^1P_1$	2.227E-13	2.202E-13
122	$2s2p^2(^3P) 2P 3p ^1D_2$	2.309E-12	2.855E-12
123	$2p^3(^4S) 3s ^5S_2$	1.251E-11	4.884E-12
124	$2s2p^2(^1D) 2D 3d ^1S_0$	1.665E-13	1.592E-13
125	$2s2p^2(^3P) 2P 3p ^1P_1$	1.244E-12	1.269E-12
126	$2s2p^2(^3P) 2P 3d ^3F_2$	1.867E-13	1.893E-13
127	$2s2p^2(^3P) 2P 3d ^3F_3$	1.598E-13	1.942E-13
128	$2s2p^2(^1S) 2S 3d ^3D_1$	2.448E-13	2.332E-13
129	$2s2p^2(^1S) 2S 3d ^3D_2$	2.822E-13	2.952E-13
130	$2p^3(^4S) 3s ^3S_1$	4.721E-13	4.714E-13
131	$2s2p^2(^1S) 2S 3d ^3D_3$	2.292E-13	1.516E-13
132	$2s2p^2(^3P) 2P 3d ^3F_4$	4.453E-13	4.182E-13
133	$2s2p^2(^3P) 2P 3d ^3D_2$	1.467E-13	1.568E-13
134	$2s2p^2(^3P) 2P 3d ^1P_1$	1.061E-13	1.000E-13
135	$2s2p^2(^3P) 2P 3d ^3D_3$	4.140E-13	3.757E-13
136	$2s2p^2(^3P) 2P 3d ^3D_1$	1.410E-13	1.427E-13
137	$2s2p^2(^1S) 2S 3d ^1D_2$	3.722E-13	3.201E-13
138	$2s2p^2(^3P) 2P 3d ^3P_2$	8.993E-14	9.749E-14
139	$2s2p^2(^3P) 2P 3d ^3P_0$	7.422E-14	7.086E-14
140	$2s2p^2(^3P) 2P 3d ^3P_1$	7.817E-14	8.123E-14
141	$2p^3(^2D) 3s ^3D_1$	9.982E-13	9.609E-13
142	$2p^3(^2D) 3s ^3D_2$	1.045E-12	1.500E-12
143	$2p^3(^4S) 3p ^5P_1$	5.943E-13	3.712E-13
144	$2s2p^2(^3P) 2P 3d ^1F_3$	5.335E-14	5.031E-14
145	$2p^3(^2D) 3s ^3D_3$	1.013E-12	9.875E-13
146	$2p^3(^4S) 3p ^5P_2$	6.503E-13	2.944E-13
147	$2p^3(^4S) 3p ^5P_3$	6.118E-13	6.364E-13
148	$2p^3(^2D) 3s ^1D_2$	5.038E-13	4.865E-13

Table 3. Continued.

No.	Level	$\tau_l(GRASP)$	$\tau_l(AS)$
149	$2s2p^2(^3P) 2P 3d ^1D_2$	6.177E-14	5.877E-14
150	$2p^3(^4S) 3p ^3P_1$	3.788E-13	3.745E-13
151	$2p^3(^4S) 3p ^3P_2$	2.373E-13	2.251E-13
152	$2p^3(^4S) 3p ^3P_0$	3.868E-13	3.899E-13
153	$2p^3(^3D) 3p ^3D_1$	4.781E-13	4.631E-13
154	$2p^3(^2P) 3s ^3P_0$	9.518E-13	9.070E-13
155	$2p^3(^2P) 3s ^3P_1$	8.375E-13	8.100E-13
156	$2p^3(^3D) 3p ^3D_2$	6.467E-13	6.529E-13
157	$2p^3(^3D) 3p ^3D_3$	6.636E-13	6.713E-13
158	$2p^3(^3D) 3p ^3F_2$	6.739E-13	7.354E-13
159	$2p^3(^2P) 3s ^3P_2$	7.907E-13	7.678E-13
160	$2p^3(^3D) 3p ^1P_1$	4.257E-13	3.917E-13
161	$2p^3(^3D) 3p ^3F_3$	6.157E-13	6.521E-13
162	$2p^3(^3D) 3p ^1F_3$	6.900E-13	7.957E-13
163	$2p^3(^3D) 3p ^3F_4$	7.624E-13	8.423E-13
164	$2p^3(^4S) 3d ^5D_0$	1.100E-11	1.022E-11
165	$2p^3(^4S) 3d ^5D_1$	6.802E-12	8.466E-12
166	$2p^3(^4S) 3d ^5D_2$	1.050E-11	1.092E-11
167	$2p^3(^4S) 3d ^5D_3$	1.989E-11	1.993E-11
168	$2p^3(^4S) 3d ^5D_4$	2.957E-11	2.721E-11
169	$2p^3(^2P) 3s ^1P_1$	4.840E-13	4.508E-13
170	$2p^3(^3D) 3p ^3P_0$	5.332E-13	5.769E-13
171	$2p^3(^3D) 3p ^3P_1$	4.967E-13	5.318E-13
172	$2p^3(^4S) 3d ^3D_2$	4.649E-13	3.931E-13
173	$2p^3(^3D) 3p ^3P_2$	3.808E-13	4.800E-13
174	$2p^3(^4S) 3d ^3D_3$	3.687E-13	3.220E-13
175	$2p^3(^4S) 3d ^3D_1$	3.441E-13	3.016E-13
176	$2p^3(^3D) 3p ^1D_2$	5.182E-13	5.803E-13
177	$2p^3(^2P) 3p ^3D_1$	5.454E-13	5.592E-13
178	$2p^3(^2P) 3p ^3S_1$	4.966E-13	4.912E-13
179	$2p^3(^3D) 3d ^3F_2$	3.083E-12	3.120E-12
180	$2p^3(^2P) 3p ^3D_2$	6.335E-13	6.529E-13
181	$2p^3(^3D) 3d ^3F_3$	3.315E-12	3.519E-12
182	$2p^3(^3D) 3d ^3G_4$	7.633E-11	7.700E-11
183	$2p^3(^3D) 3d ^1S_0$	3.132E-11	2.790E-11
184	$2p^3(^3D) 3d ^3G_3$	3.783E-12	3.885E-12
185	$2p^3(^2P) 3p ^3D_3$	6.197E-13	6.459E-13
186	$2p^3(^2P) 3p ^1P_1$	4.084E-13	3.917E-13

Table 3. Continued.

No.	Level	$\tau_l(GRASP)$	$\tau_l(AS)$
187	$2p^3(^3D) 3d ^3F_4$	7.424E-11	6.771E-11
188	$2p^3(^3D) 3d ^3G_5$	8.321E-11	7.752E-11
189	$2p^3(^3D) 3d ^1G_4$	9.254E-11	8.679E-11
190	$2p^3(^1P) 3p ^3P_0$	3.710E-13	3.759E-13
191	$2p^3(^3D) 3d ^3D_1$	1.848E-13	1.769E-13
192	$2p^3(^1P) 3p ^3P_1$	3.789E-13	3.745E-13
193	$2p^3(^1P) 3p ^3P_2$	5.799E-13	6.125E-13
194	$2p^3(^1P) 3p ^1D_2$	3.253E-13	3.162E-13
195	$2p^3(^3D) 3d ^3D_2$	1.212E-13	1.131E-13
196	$2p^3(^3D) 3d ^1P_1$	1.640E-13	1.612E-13
197	$2p^3(^3D) 3d ^3D_3$	8.239E-14	7.955E-14
198	$2p^3(^3D) 3d ^3P_2$	7.729E-14	7.696E-14
199	$2p^3(^3D) 3d ^3P_0$	1.486E-13	1.412E-13
200	$2p^3(^3D) 3d ^3P_1$	1.180E-13	1.123E-13
201	$2p^3(^3D) 3d ^1D_2$	1.622E-13	1.572E-13
202	$2p^3(^3D) 3d ^3S_1$	7.458E-14	7.800E-14
203	$2p^3(^3D) 3d ^1F_3$	9.480E-14	9.268E-14
204	$2p^3(^1P) 3d ^3F_2$	1.145E-12	1.194E-12
205	$2p^3(^1P) 3d ^3F_3$	1.439E-12	1.155E-12
206	$2p^3(^1P) 3p ^1S_0$	3.390E-13	3.579E-13
207	$2p^3(^1P) 3d ^3F_4$	3.437E-11	3.125E-11
208	$2p^3(^1P) 3d ^3P_2$	1.965E-13	2.524E-13
209	$2p^3(^1P) 3d ^3P_0$	1.368E-13	1.356E-13
210	$2p^3(^1P) 3d ^3P_1$	1.576E-13	1.538E-13
211	$2p^3(^1P) 3d ^1D_2$	2.042E-13	1.572E-13
212	$2p^3(^1P) 3d ^3D_1$	7.814E-14	7.121E-14
213	$2p^3(^1P) 3d ^3D_3$	2.707E-13	2.520E-13
214	$2p^3(^1P) 3d ^3D_2$	9.484E-14	1.131E-13
215	$2p^3(^1P) 3d ^1F_3$	6.558E-14	5.779E-14
216	$2p^3(^1P) 3d ^1P_1$	5.725E-14	5.220E-14

216 lifetimes are reported in Tab. 3. There is no values to compare with, but from the two different methods (TFDA and MCDHF), the difference is less than 10 %.

3.2. Transition parameters of the V XVIII ion

Table 4. Weighted oscillator strengths and transition probabilities calculated by the AS code ($gf(AS)$ and $gA(AS)$) and by the GRASP2018 code ($gf(GRASP)$ and $gA(GRASP)$), compared with NIST database values $gf(NIST)$ and $gA(NIST)$

No.	L	U	gf (GRASP)	gf (AS)	gA (GRASP)	gA (AS)	gf (NIST)	gA (NIST)
1	1	22	5.55E-02	5.26E-02	1.22E+12	1.15E+12		
2	1	24	1.84E-03	1.78E-03	4.15E+10	4.00E+10		
3	1	40	1.25E+00	1.25E+00	3.14E+13	3.13E+13		
4	1	48	4.27E-03	6.02E-04	1.09E+11	1.54E+10		
5	1	55	4.49E-02	4.79E-02	1.17E+12	1.25E+12		
6	1	58	7.92E-02	7.27E-02	2.08E+12	1.91E+12		
7	1	62	2.06E-01	2.23E-01	5.46E+12	5.92E+12		
8	1	70	4.43E-02	4.49E-02	1.20E+12	1.22E+12		
9	1	97	2.73E-02	2.84E-02	7.77E+11	8.13E+11		
10	1	114	1.11E-02	2.84E-02	3.26E+11	8.13E+11		
11	1	116	5.98E-02	4.49E-02	1.77E+12	1.22E+12		
12	2	21	5.68E-02	5.59E-02	1.23E+12	1.21E+12		
13	2	22	3.36E-02	3.28E-02	7.28E+11	7.08E+11		
14	2	23	7.51E-02	7.11E-02	1.66E+12	1.57E+12		
15	2	24	7.95E-03	7.46E-03	1.77E+11	1.66E+11		
16	2	35	1.32E-02	3.30E-02	3.21E+11	8.02E+11		
17	2	39	1.05E+00	1.10E+00	2.59E+13	2.75E+13		
18	2	40	2.58E-01	2.16E-01	6.37E+12	5.36E+12		
19	2	44	1.19E+00	1.10E+00	2.98E+13	2.75E+13		
20	2	47	2.36E-01	1.76E-01	5.94E+12	4.45E+12		
21	2	48	6.86E-01	7.22E-01	1.73E+13	1.83E+13	6.90E-01	1.70E+13
22	2	49	3.15E-01	3.18E-01	7.94E+12	8.05E+12		
23	2	51	1.69E-04	8.00E-07	4.33E+09	2.04E+07		
24	2	52	4.15E-02	4.01E-02	1.06E+12	1.67E+12		
25	2	54	1.30E-02	9.79E-04	3.32E+11	2.51E+10		
26	2	55	7.49E-02	7.86E-02	1.93E+12	2.02E+12		
27	2	58	1.45E-02	2.12E-02	3.77E+11	5.50E+11		
28	2	59	4.27E-02	3.53E-02	1.11E+12	9.18E+11		
29	2	62	1.62E-01	1.64E-01	4.25E+12	4.29E+12		
30	2	63	5.68E-01	5.95E-01	1.50E+13	1.57E+13		
31	2	67	4.79E-03	3.81E-03	1.27E+11	1.01E+11		
32	2	68	1.23E-01	1.23E-01	3.27E+12	3.24E+12		
33	2	70	6.91E-02	7.21E-02	1.85E+12	1.93E+12		
34	2	71	6.08E-02	6.13E-02	1.63E+12	1.64E+12		
35	2	88	3.52E-03	3.49E-03	9.82E+10	9.76E+10		
36	2	95	6.79E-03	6.19E-03	1.91E+11	1.75E+11		

Table 4. Continued.

No.	L	U	gf (GRASP)	gf (AS)	gA (GRASP)	gA (AS)	gf (NIST)	gA (NIST)
37	2	97	2.57E-02	2.67E-02	7.23E+11	7.56E+11		
38	2	114	3.77E-02	2.67E-02	1.10E+12	7.56E+11		
39	2	116	2.84E-02	7.21E-02	8.29E+11	1.93E+12		
40	2	126	6.93E-02	6.13E-02	2.06E+12	1.64E+12		
41	2	132	4.84E-03	2.04E-04	1.45E+11	2.90E+10		
42	2	134	2.63E-02	7.21E-02	7.87E+11	1.93E+12		
43	3	22	9.14E-02	8.99E-02	1.96E+12	1.92E+12		
44	3	23	1.90E-01	1.82E-01	4.15E+12	3.98E+12		
45	3	24	1.68E-03	1.59E-03	3.70E+10	3.48E+10		
46	3	35	1.29E-01	8.89E-02	3.09E+12	2.14E+12		
47	3	38	6.60E-01	8.48E-01	1.60E+13	2.07E+13		
48	3	39	1.37E-01	1.56E-01	3.34E+12	3.87E+12		
49	3	40	9.38E-03	1.54E-02	2.30E+11	3.78E+11		
50	3	44	7.28E-02	1.56E-01	1.80E+12	3.87E+12		
51	3	45	3.33E+00	3.10E+00	8.28E+13	7.72E+13	3.10E+00	7.70E+13
52	3	47	1.42E+00	1.35E+00	3.54E+13	3.37E+13		
53	3	48	3.67E-01	3.58E-01	9.17E+12	8.97E+12	3.45E-01	8.70E+12
54	3	52	3.19E-02	2.61E-02	8.08E+11	6.61E+11		
55	3	53	1.24E-01	1.45E-01	3.16E+12	3.67E+12		
56	3	55	8.58E-02	8.98E-02	2.19E+12	2.29E+12		
57	3	56	5.13E-04	2.87E-04	1.31E+10	7.32E+09		
58	3	57	1.12E-03	1.87E-03	2.89E+10	4.81E+10		
59	3	58	1.50E-02	1.77E-02	3.86E+11	4.55E+11		
60	3	61	8.58E-02	6.64E-02	2.23E+12	1.72E+12		
61	3	62	2.36E-03	1.80E-03	6.13E+10	4.69E+10		
62	3	63	4.23E-02	4.47E-02	1.10E+12	1.17E+12		
63	3	67	1.92E-02	1.49E-02	5.06E+11	3.91E+11		
64	3	69	7.73E-01	7.91E-01	2.04E+13	2.09E+13		
65	3	70	2.49E-01	2.50E-01	6.59E+12	6.63E+12		
66	3	71	5.22E-01	5.34E-01	1.38E+13	1.42E+13		
67	3	88	4.45E-02	4.52E-02	1.23E+12	1.25E+12		
68	3	92	1.73E-02	2.24E-02	4.81E+11	6.23E+11		
69	3	95	4.76E-02	5.19E-02	1.33E+12	1.45E+12		
70	3	97	2.99E-02	2.87E-02	8.33E+11	8.03E+11		
71	3	100	3.21E-02	4.47E-02	8.99E+11	1.17E+12		
72	3	103	3.22E-02	4.45E-03	9.03E+11	1.99E+11		
73	3	115	2.07E-02	4.47E-02	5.98E+11	1.17E+12		
74	3	132	1.01E-01	8.98E-02	3.00E+12	2.29E+12		
75	3	142	1.02E-02	3.89E-03	3.06E+11	1.73E+11		
76	4	22	1.24E-02	1.23E-02	2.57E+11	2.54E+11		
77	4	23	2.92E-02	2.98E-02	6.18E+11	6.28E+11		

Table 4. Continued.

No.	L	U	gf (<i>GRASP</i>)	gf (<i>AS</i>)	gA (<i>GRASP</i>)	gA (<i>AS</i>)	gf (<i>NIST</i>)	gA (<i>NIST</i>)
78	4	24	1.99E-01	1.95E-01	4.25E+12	4.14E+12		
79	4	35	1.43E-01	7.71E-02	3.34E+12	1.80E+12		
80	4	38	5.67E-02	5.56E-02	1.33E+12	1.31E+12		
81	4	39	2.89E-01	3.34E-01	6.81E+12	8.02E+12		
82	4	40	2.07E-03	3.09E-03	4.90E+10	7.36E+10		
83	4	44	3.18E-01	3.34E-01	7.60E+12	8.02E+12		
84	4	45	8.63E-02	1.27E-01	2.08E+12	3.05E+12		
85	4	47	4.05E-01	4.70E-01	9.79E+12	1.14E+13		
86	4	48	4.75E-02	4.81E-02	1.15E+12	1.17E+12		
87	4	52	6.84E-03	1.77E-03	1.68E+11	7.16E+10		
88	4	53	4.84E+00	4.78E+00	1.19E+14	1.18E+14		
89	4	54	5.00E-02	2.72E-02	1.23E+12	6.67E+11		
90	4	55	2.75E-03	3.80E-03	6.80E+10	9.39E+10		
91	4	57	9.66E-05	1.40E-04	2.41E+09	3.48E+09		
92	4	58	3.68E-04	5.36E-04	9.19E+09	1.34E+10		
93	4	59	1.07E-04	1.67E-04	2.67E+09	4.16E+09		
94	4	61	8.29E-03	8.05E-03	2.09E+11	2.02E+11		
95	4	62	4.79E-04	5.07E-04	1.21E+10	1.28E+10		
96	4	63	1.83E-03	2.36E-03	4.65E+10	5.98E+10		
97	4	67	7.98E-04	7.32E-04	2.04E+10	1.87E+10		
98	4	69	4.90E-02	7.65E-02	1.25E+12	1.96E+12		
99	4	70	1.35E-02	1.52E-02	3.47E+11	3.90E+11		
100	4	71	1.92E-02	2.29E-02	4.94E+11	5.90E+11		
101	4	88	2.09E-01	2.03E-01	5.60E+12	5.48E+12		
102	4	92	2.09E-02	4.31E-03	5.62E+11	1.17E+11		
103	4	95	4.79E-01	4.84E-01	1.30E+13	1.31E+13		
104	4	97	7.37E-02	6.54E-02	2.00E+12	1.78E+12		
105	4	100	5.10E-03	2.36E-03	1.39E+11	5.98E+10		
106	4	103	1.47E-01	7.65E-02	4.02E+12	1.96E+12		
107	4	108	1.59E-02	1.52E-02	4.36E+11	3.90E+11		
108	4	111	8.75E-02	2.29E-02	2.41E+12	5.90E+11		
109	4	114	3.09E-02	1.45E-02	8.67E+11	2.70E+11		
110	4	115	8.03E-04	2.36E-03	2.26E+10	5.98E+10		
111	4	128	7.01E-02	7.65E-02	2.01E+12	1.96E+12		
112	4	131	6.86E-02	2.29E-02	1.97E+12	5.90E+11		
113	4	132	4.01E-02	3.80E-03	1.16E+12	9.39E+10		
114	5	22	3.52E-03	3.14E-03	7.01E+10	6.24E+10		
115	5	24	6.74E-02	6.57E-02	1.38E+12	1.34E+12		
116	5	40	1.28E-02	1.11E-02	2.92E+11	4.28E+11		
117	5	48	4.95E-03	4.98E-03	1.16E+11	1.17E+11		
118	5	52	2.19E-02	1.53E-02	5.20E+11	6.04E+11		

Table 4. Continued.

No.	L	U	gf (GRASP)	gf (AS)	gA (GRASP)	gA (AS)	gf (NIST)	gA (NIST)
119	5	54	1.25E+00	8.55E-01	2.97E+13	2.03E+13		
120	5	55	2.26E-02	1.55E-02	5.40E+11	3.70E+11		
121	5	58	5.42E-03	5.18E-03	1.31E+11	1.25E+11		
122	5	62	5.36E-03	6.55E-03	1.30E+11	1.59E+11		
123	5	70	6.48E-04	8.26E-04	1.61E+10	2.05E+10		
124	5	97	2.85E-03	3.02E-03	7.47E+10	7.94E+10		
125	5	114	3.93E-02	6.55E-03	1.06E+12	1.59E+11		
126	5	116	3.85E-02	8.26E-04	1.05E+12	2.05E+10		
127	5	132	1.67E-02	1.55E-02	4.66E+11	3.70E+11		
128	5	134	6.56E-02	8.26E-04	1.83E+12	2.05E+10		

Oscillator strengths and transition probabilities are presented in Tab. 4. The differences between the calculated values and the NIST database values are less than 5 %. In average the AS and GRASP oscillator strengths and transition probabilities values differ by about 30 %.

Comparing our results of energy values, lifetimes, oscillator strengths and transition probabilities using the TFDA and MCDHF methods with available values, we recommend our MCDHF data calculated using the GRASP atomic structure code. The TFDA method gives data which are near the MCDHF results.

4. Conclusions

In this work, we calculated energy levels of the vanadium carbon-like ion V XVIII using two different methods: The TFDA and the fully relativistic MCDHF methods using the AS and the GRASP2018 atomic structure codes. We obtained good values of energy levels, new lifetime values, weighted oscillator strengths and transition probabilities for transitions from the fundamental configurations levels. Our results are interesting for plasma and astrophysical applications.

References

- Aggarwal, K. M., Oscillator Strengths for Transitions in C-like Ne, Mg, Si, and S Ions. 1998, *APJS*, **118**
- Aggarwal, K. M., Hibbert, A., & Keenan, F. P., Oscillator Strengths for Transitions in O III. 1997, *APJS*, **108**

- Aggarwal, K. M., Keenan, F. P., & Msezane, A. Z., Oscillator Strengths for Transitions in C-like Ions between F IV and Ar XIII. 2001, *APJS*, **136**
- Al-Modlej, A., Alraddadi, R. A. B., & Ben Nessib, N., Energy levels and oscillator strengths for carbon isoelectronic sequence from C I to Ne V. 2018, *The European Physical Journal Plus*, **133**, 1
- Aller, L. H. and Keyes, C. D., A Spectroscopic Survey of 51 Planetary Nebulae. 1987, *APJS*, **65**, 405
- Almodlej, A., Alrashed, H., Ben Nessib, N., & et al., Atomic structure for carbon-like ions from Na VI to Ar XIII. 2021, *Monthly Notices of the Royal Astronomical Society*, **507**, 3228
- Alwadie, N., Almodlej, A., Ben Nessib, N., & et al., Atomic structure of the carbon like ion Ca XV. 2020, *Contributions of the Astronomical Observatory Skalnat Pleso*, **50**, 86
- Badnell, N., Dielectronic recombination of Fe^{22+} and Fe^{21+} . 1986, *Journal of Physics B: Atomic and Molecular Physics*, **19**, 3827
- Badnell, N., A Breit–Pauli distorted wave implementation for autostructure. 2011, *Computer Physics Communications*, **182**, 1528
- Badnell, N., General Program for Calculation of Atomic and Ionic Properties. version 28.46, 2022. 2022, *Astrophysics Source Code Library*, <http://amdpp.phys.strath.ac.uk/autos/>
- Bhatia, A. K. & Doschek, G. A., Atomic Data and Spectral Line Intensities for C-Like Si IX. 1993, *ADNDT*, **55**
- Cowan, R. D. 1981, *The theory of atomic structure and spectra* (Univ of California Press)
- Eissner, W., Jones, M., & Nussbaumer, H., Techniques for the calculation of atomic structures and radiative data including relativistic corrections. 1974, *Computer Physics Communications*, **8**, 270
- Ekman, J., Jönsson, P., Gustafsson, S., et al., Calculations with spectroscopic accuracy: energies, transition rates, and Landé gJ-factors in the carbon isoelectronic sequence from Ar XIII to Zn XXV. 2014, *Astronomy & Astrophysics*, **564**, A24
- Fawcett, B. C., Oscillator Strengths of Allowed Transitions for C I, N II, and O III. 1987, *ADNDT*, **37**
- Fischer, C. F., Godefroid, M., Brage, T., Jnsson, P., & Gaigalas, G., Advanced multiconfiguration methods for complex atoms: I. Energies and wave functions. 2016, *Journal of Physics B: Atomic, Molecular and Optical Physics*, **49**, 182004, DOI: 10.1088/0953-4075/49/18/182004
- Froese Fischer, C., Gaigalas, G., Jnsson, P., & Biero, J., GRASP2018A Fortran 95 version of the General Relativistic Atomic Structure

- Package. 2019, *Computer Physics Communications*, **237**, 184, DOI: <https://doi.org/10.1016/j.cpc.2018.10.032>
- Froese Fischer, C. & Tachiev, G., BreitPauli energy levels, lifetimes, and transition probabilities for the beryllium-like to neon-like sequences. 2004, *ADNDT*, **87**
- Goldsmith, S., Feldman, U., Crooker, A., & Cohen, L., Carbon-Like Spectra of Sc xvi, Ti xvii, and V xviii in the Range 16–22 Å. 1972, *JOSA*, **62**, 260
- Jönsson, P., Rynkun, P., & Gaigalas, G., Energies, E1, M1, and E2 transition rates, hyperfine structures, and Landé gJ factors for states of the 2s22p2, 2s2p3, and 2p4 configurations in carbon-like ions between F IV and Ni XXIII. 2011, *ADNDT*, **97**
- Jnsson, P., Rynkun, P., & Gaigalas, G., Energies, E1, M1, and E2 transition rates, hyperfine structures, and Land gJ factors for states of the 2s22p2, 2s2p3, and 2p4 configurations in carbon-like ions between F IV and Ni XXIII. 2011, *Atomic Data and Nuclear Data Tables*, **97**, 648, DOI: <https://doi.org/10.1016/j.adt.2011.05.001>
- Keenan, F. P., Aggarwal, K. M., & Berrington, K. A., Electron density diagnostics for Ca XV in Tokamak plasmas. 1988, *JPHB*, **21**, L89
- Kramida, A., Yu. Ralchenko, Reader, J., & and NIST ASD Team. 2021, NIST Atomic Spectra Database (ver. 5.9), [Online]. Available: <https://physics.nist.gov/asd> [2022, March 28]. National Institute of Standards and Technology, Gaithersburg, MD.
- Li, J., Zhang, C., Del Zanna, G., et al., Large-scale Multiconfiguration Dirac–Hartree–Fock Calculations for Astrophysics: C-like Ions from O iii to Mg vii. 2022, *The Astrophysical Journal Supplement Series*, **260**, 50
- Luo, D. & Pradhan, A. K., Atomic data for opacity calculations. XI. The carbon isoelectronic sequence. 1989, *JPHB*, **22**, 3377
- Widing, K. G. & Cook, J. W., SKYLAB XUV Observations of Densities, Thermal Structure, and Mass Motions in a Compact Flare. 1987, *APJ*, **320**, 913
- Widing, K. G., Feldman, U., & Bhatia, A. K., The Extreme-Ultraviolet Spectrum (300–630 Angstrom) of an Errupting Prominence Observed from SKYLAB. 1986, *APJ*, **308**, 982
- Wu, C., Wu, Y., Yan, J., Chang, T., & Gao, X., Transition energies and oscillator strengths for the intrashell and intershell transitions of the C-like ions in a thermodynamic equilibrium plasma environment. 2022, *Physical Review E*, **105**, 015206
- Zhang, H. L. & Sampson, D. H., Relativistic Distorted-Wave Collision Strengths and Oscillator Strengths for the $\Delta n = 0$ Transitions with $n = 2$ in C-like Ions with $9 \leq Z \leq 54$. 1996, *ADNDT*, **63**

New database for collisional excitation/ ionization processes of astrophysical interest

V. Vujčić¹ , V.A. Srećković²  and D. Jevremović¹

¹ *Astronomical Observatory, Volgina 7, 11060 Belgrade, Serbia (E-mail: veljko@aob.rs)*

² *Institute of Physics Belgrade, University of Belgrade, Pregrevica 118, 11080 Belgrade, Serbia (E-mail: vlada@ipb.ac.rs)*

Received: August 23, 2022; Accepted: October 2, 2022

Abstract. In this paper, ACol database for the collisional processes in atom and Rydberg atom collisions is described. Database (DB) is hosted and is a part of the Serbian Virtual Observatory (SerVO) and VAMDC project. The database contains the rate coefficients for excitation and ionization collisional processes in hydrogen, helium and alkali plasmas. The ACol dataset could help with the investigation and modeling of laboratory low temperature plasmas as well as weakly ionized layers in various atmospheres and cosmic objects.

Key words: Atomic data – Modeling – Astrophysical plasma – Line profile – Planetary geochemistry – AGN

1. Introduction

Atomic and molecular (A&M) data and databases [Sahal-Bréchet et al. \(2014\)](#); [Marinković et al. \(2017\)](#); [Albert et al. \(2020\)](#) have become essential for diagnostics and development of models and simulations of complex physical processes and for the interpretation of data provided by measurements e.g. in laboratory and astrophysical plasmas ([Christensen-Dalsgaard et al., 1996](#); [Fontenla et al., 2009](#); [Srećković et al., 2017](#); [Hauschildt & Baron, 2010](#); [Husser et al., 2013](#)). Diagnostics and development of models and simulations of low temperature laboratory and astrophysical plasmas (LTPs) requires usage of accurate A&M data, both experimental and theoretical [Jevremović et al. \(2020\)](#); [Albert et al. \(2020\)](#).

It is shown [Adamovich et al. \(2017, 2022\)](#) that such data is very important in the development of plasmas as an enabling technology for a vast range of fields associated with modern society. From technological perspective, this often means heterogeneous e-ecosystem, consisting of different datasets and formats and various programming frameworks synchronized to work together, such as in VAMDC (vamdc.org) project efforts ([Dubernet et al., 2016](#)). Access to large amounts of A&M data is now required by the plasma community, and VAMDC

provides 30+ nodes, several of them containing recommended data relevant to modeling LTPs.

The A&M community revealed a grown maturity in the process of curating (i.e. collecting, categorizing, archiving and distributing) dynamical data relevant to the kinetic modeling of LTPs, moving from the cold gas approximation to the state-to-state approach, in the perspective of deepening the knowledge on elementary processes involving both electron and heavy species collisions (Marinković et al., 2017; Srećković et al., 2018; Adamovich et al., 2022).

In this contribution, ACol database for heavy particle collisions i.e. for the collisional processes in atom and Rydberg atom collisions is described. Database is hosted and is a part of the Serbian Virtual Observatory (SerVO). It contains the rate coefficients for excitation and ionization collisional processes in hydrogen, helium and alkali plasmas. ACol database (DB) is in the development phase. The dataset could help with the investigation and modeling of laboratory low temperature plasmas as well as weakly ionized layers in various atmospheres and cosmic objects (Srećković et al., 2014; Klyucharev et al., 2007; Ignjatović et al., 2019).

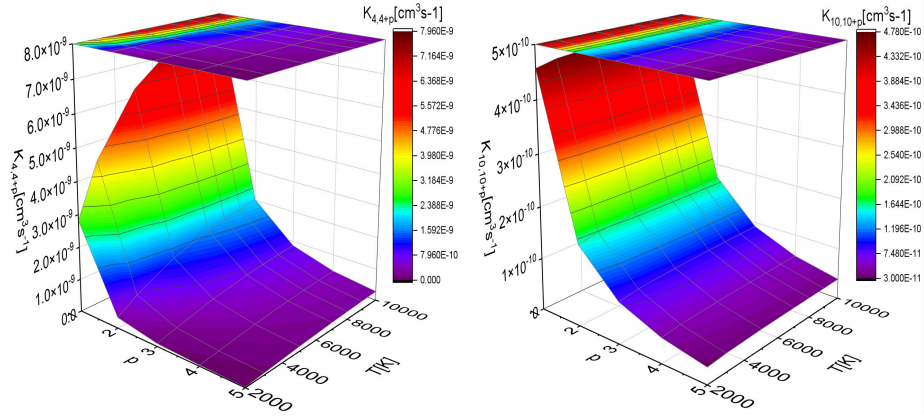
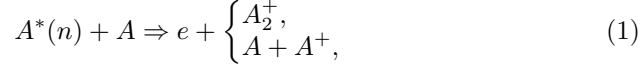


Figure 1. Left: Rate coefficients $K_{4,4+p}(T)$ for the excitation processes $H^*(n) + H \Rightarrow H^*(n=n+p) + H$ in hydrogen plasmas ($n=4$, $1 \leq p \leq 5$, $A=H$ in Eq.(2)). Right: Rate coefficients $K_{10,10+p}(T)$ for excitation processes $H^*(n) + H \Rightarrow H^*(n=n+p) + H$ in hydrogen plasmas ($n=10$, $1 \leq p \leq 5$, $A=H$ in Eq.(2)).

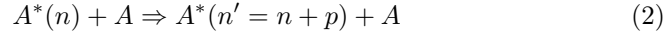
2. The collisional processes

ACol database contains calculated data for excitation and ionization processes in heavy particle collisions. In other words, the database consists of collisional

ionization



and excitation



data. Here A are atoms and their ions in the ground states, $A^*(n)$ is the Rydberg atom (RA), and A_2^+ their molecular ions.

2.1. DRM

The data are obtained within the DRM i.e., the collisional reactions have been treated by the so-called dipole resonant mechanism (DRM). In this characterization, the processes are caused by the dipole part of the electrostatic interaction between the outer highly excited i.e. Rydberg electron and the inner (ion-atom) system. This method is especially effective when used with the so-called decay approximation. A detailed description can be found in paper of Mihajlov and coworkers (Mihajlov et al., 2011; Mihajlov et al., 2012; Srećković et al., 2018).

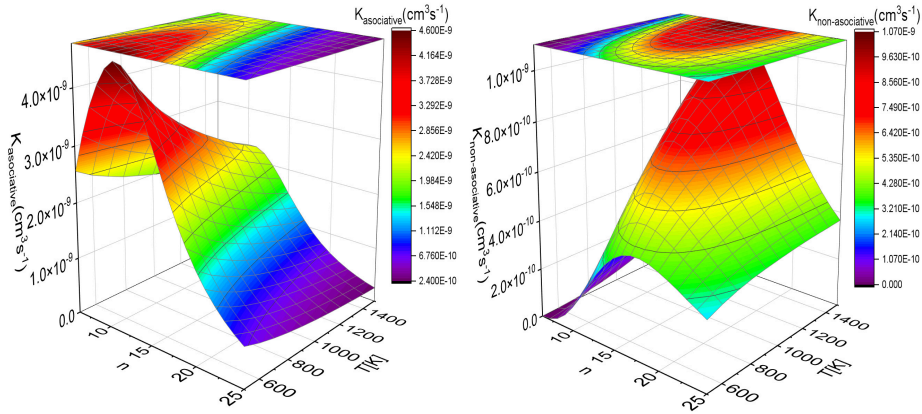


Figure 2. Left: Rate coefficient $Ka(n; T)$ for ionization collisional processes Eq.(1a) in potassium plasmas. Associative channel; Right: Rate coefficient $Kb(n; T)$ for ionization collisional processes Eq.(1b) in potassium plasmas. Non-associative channel

2.2. The obtained quantities

In the process of ACol DB creation, we collected needed data, made a corresponding model and we calculated rate coefficients. For the calculations, we

developed sophisticated model for corresponding collision processes. We determined theoretically - calculated cross-sections and rate coefficients for the ionization and excitation processes for hydrogen, helium and alkali plasmas, for conditions of interest of laboratory/astrophysical LTPs.

The figures 1 and 2 show heavy species collisions - rate coefficients from the calculations we carried out (see e.g. Mihajlov et al. (2011); Srećković et al. (2018)).

Validation is also a crucial step in the development of databases (Srećković et al., 2017). For instance, measurements of the rate coefficients of associative ionization in collisions of metastable atoms necessitate meeting several technical challenges as noted in the literature (Boyd & Josyula, 2021). Perhaps the biggest challenge of these measurements is isolating the associative ionization in atomic collisions (Adamovich et al., 2022)

3. Software and Data

We wrote data model (shown in Fig 3) for our new atomic collisional data node (ACol) as a subset of XSAMS (XML Schema for Atoms, Molecules and Solids - <https://vamdc-standards.readthedocs.io/en/latest/dataModel/vamdcxsams/structure.html>) to set up a new VAMDC node for the LTP data that could be useful for the laboratory and astrophysical community. After translating data model into Django-Python models class, we generated a MySQL (MariaDB) database with object-relational mapping to tables. We converted data from a textual source to the database. We customly fit software for this new VAMDC node, according to the NodeSoftware project (<https://github.com/VAMDC/NodeSoftware>).

In Figure 3 is presented a class diagram for the ACol node (logical model).

The result is a new VAMDC node, hosted on Serbian virtual observatory <http://servo.aob.rs/acol/>. Establishing this database/node might be important for diagnostics and modeling of LTPs which are used for the modeling astrophysical and laboratory plasmas. The node is in debug phase and will need some time to be officially included to VAMDC portal (https://portal.vamdc.eu/vamdc_portal/home.seam). Tap query already is available as a web service (also via TAPValidator). Capabilities listed at <http://servo.aob.rs/acol/tap/capabilities>; sample query: `servo.aob.rs/acol/tap/sync?LANG=VSS2&REQUEST=doQuery&FORMAT=XSAMS&QUERY=select+*`. Also, we will host queries locally on the website which also deliver data in XSAMS format defined by the VAMDC (servo.aob.rs/acol/).

4. Summary

Based on the foregoing, it can be inferred that examined collisional excitation/ionization processes and data in ACol DB could play a important role in the

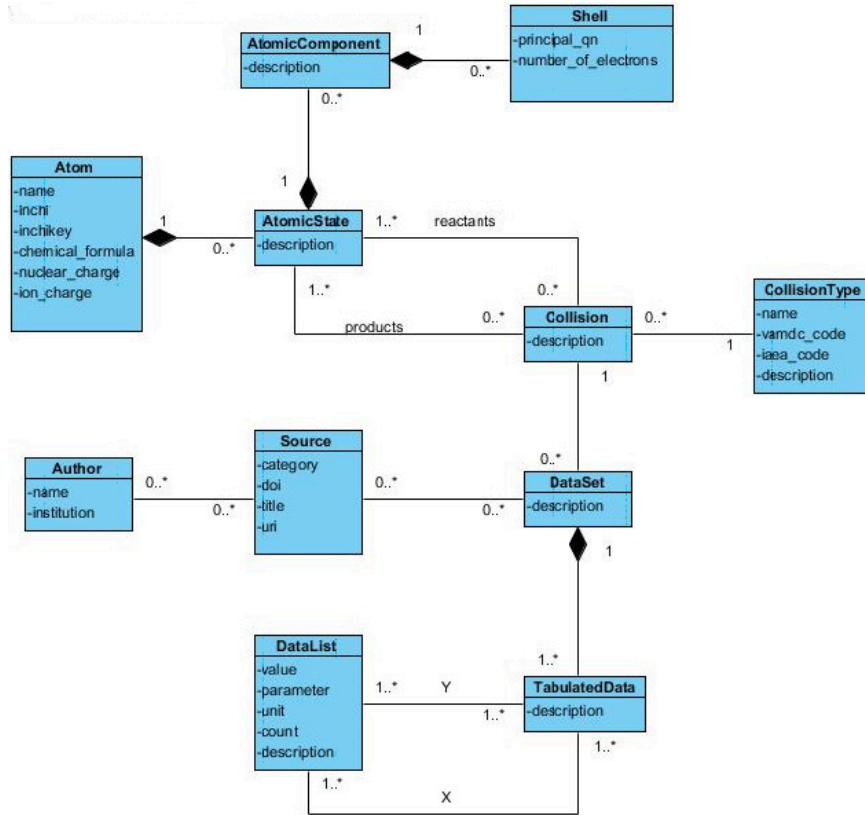


Figure 3. Class diagram for the ACol node (logical model)

spectral exploration of many astrophysical environments and laboratory LTPs (Wilson et al., 2002; Klyucharev et al., 2007; Ignjatović et al., 2019; Adamovich et al., 2022) although it is in the development i.e. debug stage. Due to their rapid expansion in the modern world, services like atomic databases and astronomical virtual observatories must continue to be developed and offered. This is the rationale behind SerVO’s and VAMDC’s ACol continued database development.

Acknowledgements. The authors acknowledge the support from the Astronomical observatory and Institute of Physics, Belgrade, which was made possible by grants from the Ministry of Education, Science and Technological Development of the Republic of Serbia. This article is based upon work from COST Action 19110 PIAgri, supported by COST (European Cooperation in Science and Technology). We would also like to express our gratitude to Ognjan Kouchev for time and effort put into this work, as well as for a fruitful discussion.

References

- Adamovich, I., Agarwal, S., Ahedo, E., et al., The 2022 Plasma Roadmap: low temperature plasma science and technology. 2022, *Journal of Physics D Applied Physics*, **55**, 373001, DOI: 10.1088/1361-6463/ac5e1c
- Adamovich, I., Baalrud, S. D., Bogaerts, A., et al., The 2017 Plasma Roadmap: Low temperature plasma science and technology. 2017, *Journal of Physics D Applied Physics*, **50**, 323001, DOI: 10.1088/1361-6463/aa76f5
- Albert, D., Antony, B. K., Ba, Y. A., et al., A Decade with VAMDC: Results and Ambitions. 2020, *Atoms*, **8**, 76, DOI: 10.3390/atoms8040076
- Boyd, I. D. & Josyula, E., Analysis of Associative Ionization Rates for Hypersonic Flows. 2021, *Journal of Thermophysics and Heat Transfer*, **35**, 484, DOI: 10.2514/1.T6109
- Christensen-Dalsgaard, J., Dappen, W., Ajukov, S. V., et al., The Current State of Solar Modeling. 1996, *Science*, **272**, 1286, DOI: 10.1126/science.272.5266.1286
- Dubernet, M. L., Antony, B. K., Ba, Y. A., et al., The virtual atomic and molecular data centre (VAMDC) consortium. 2016, *Journal of Physics B Atomic Molecular Physics*, **49**, 074003, DOI: 10.1088/0953-4075/49/7/074003
- Fontenla, J. M., Curdt, W., Haberreiter, M., Harder, J., & Tian, H., Semiempirical Models of the Solar Atmosphere. III. Set of Non-LTE Models for Far-Ultraviolet/Extreme-Ultraviolet Irradiance Computation. 2009, *Astrophysical Journal*, **707**, 482, DOI: 10.1088/0004-637X/707/1/482
- Hauschildt, P. H. & Baron, E., A 3D radiative transfer framework. VI. PHOENIX/3D example applications. 2010, *Astronomy and Astrophysics*, **509**, A36, DOI: 10.1051/0004-6361/200913064
- Husser, T. O., Wende-von Berg, S., Dreizler, S., et al., A new extensive library of PHOENIX stellar atmospheres and synthetic spectra. 2013, *Astronomy and Astrophysics*, **553**, A6, DOI: 10.1051/0004-6361/201219058
- Ignjatović, L. M., Srećković, V. A., & Dimitrijević, M. S., The collisional atomic processes of Rydberg alkali atoms in geo-cosmical plasmas. 2019, *Monthly Notices of the Royal Astronomical Society*, **483**, 4202, DOI: 10.1093/mnras/sty3294
- Jevremović, D., Srećković, V. A., Marinković, B. P., & Vujčić, V., Databases for collisional and radiative processes in small molecules needed for spectroscopy use in astrophysics. 2020, *Contributions of the Astronomical Observatory Skalnaté Pleso*, **50**, 44, DOI: 10.31577/caosp.2020.50.1.44
- Klyucharev, A. N., Bezuglov, N. N., Matveev, A. A., et al., Rate coefficients for the chemi-ionization processes in sodium- and other alkali-metal geocosmical plasmas. 2007, *New Astronomy Review*, **51**, 547, DOI: 10.1016/j.newar.2007.05.001
- Marinković, B. P., Jevremović, D., Srećković, V. A., et al., BEAMDB and Mold - databases for atomic and molecular collisional and radiative processes: Belgrade nodes of VAMDC. 2017, *European Physical Journal D*, **71**, 158, DOI: 10.1140/epjd/e2017-70814-6

- Mihajlov, A., Srećković, V., Ignjatović, L. M., & Klyucharev, A., The Chemi-ionization Processes in Slow Collisions of Rydberg Atoms with Ground State Atoms: Mechanism and Applications. 2012, *Journal of Cluster Science*, **23**, 47, DOI: 10.1007/s10876-011-0438-7
- Mihajlov, A. A., Ignjatović, L. M., Srećković, V. A., & Dimitrijević, M. S., Chemi-ionization in Solar Photosphere: Influence on the Hydrogen Atom Excited States Population. 2011, *The Astrophysical Journal Supplement Series*, **193**, 2, DOI: 10.1088/0067-0049/193/1/2
- Sahal-Bréchet, S., Dimitrijević, M. S., Moreau, N., & Ben Nessib, N., The STARK-B database as a resource for “STARK” widths and shifts data: State of advancement and program of development. 2014, *Advances in Space Research*, **54**, 1148, DOI: 10.1016/j.asr.2013.08.015
- Srećković, V., Dimitrijević, M., Ignjatović, L., Bezuglov, N., & Klyucharev, A., The Collisional Atomic Processes of Rydberg Hydrogen and Helium Atoms: Astrophysical Relevance. 2018, *Galaxies*, **6**, 72, DOI: 10.3390/galaxies6030072
- Srećković, V., Ignjatović, L., Jevremović, D., Vujčić, V., & Dimitrijević, M., Radiative and Collisional Molecular Data and Virtual Laboratory Astrophysics. 2017, *Atoms*, **5**, 31, DOI: 10.3390/atoms5030031
- Srećković, V. A., Mihajlov, A. A., Ignjatović, L. M., & Dimitrijević, M. S., Ion-atom radiative processes in the solar atmosphere: quiet Sun and sunspots. 2014, *Advances in Space Research*, **54**, 1264, DOI: 10.1016/j.asr.2013.11.017
- Wilson, J. K., Mendillo, M., Baumgardner, J., et al., The Dual Sources of Io’s Sodium Clouds. 2002, *Icarus*, **157**, 476, DOI: 10.1006/icar.2002.6821

Transport coefficients for He^+ ions in mixtures He/CF_4 : modeling laboratory and astrophysical plasmas

Ž.D. Nikitović and Z.M. Raspopović

*Institute of Physics Belgrade, University of Belgrade, Pregrevica 118, 11080
Belgrade, Serbia*

Received: July 23, 2022; Accepted: October 1, 2022

Abstract. A complete set of cross sections for helium ions in a mixture of helium and carbon tetrafluoride is recommended. The transport properties for He^+ ions in He/CF_4 mixtures required to model the discharge containing the mentioned ions were calculated by the Monte Carlo method at a temperature of $T = 300$ K. In this paper we give the drift velocity, characteristic energy, reduced mobility and specially rate coefficients for low and moderately reduced electric fields E/N (E -electric field, N -gas density) and accounting for non-conservative collisions. This paper is dedicated to the presentation of the set for He^+ ions scattering cross-sections in CF_4 which is estimated using available experimental data for exothermic charge transfer cross-sections producing CF_3^+ and CF_2^+ ions and endothermic charge transfer cross-section producing CF^+ , C^+ and F^+ ions. The aim of this paper is to determine how the addition of a percentage for He in He/CF_4 mixtures affects the separation of bulk and flux transport parameters for He^+ ions.

Key words: He^+ – He/CF_4 mixtures – Monte Carlo simulations – cross sections – transport coefficients

1. Introduction

$\text{He}-\text{CF}_4$ mixtures are used in gaseous electronic multipliers for various imaging purposes (X-rays, charged particles, thermal neutrons and dark matter detection) (Fraga et al., 2003; Kaboth et al., 2008). After hydrogen, which makes up about 90% of the cosmos, helium is the second most abundant element (about 9%).

We notice the importance of obtained results as atomic and molecular data which are input parameters for modeling of various environments. Low temperature can change the state of metals, gases, liquids and solids, cause damage to organisms depending on length of exposure, and change the functionality of mechanized processes. Electron multiplication bursts affect the production of various ions that can affect the time distribution of detected particles (Bošnjaković, 2016). The experimental transport coefficients required as input data for He^+ ion transport models in He are existing (Viehland et al., 2017;

Basurto et al., 2000; Helm, 1977; Stefansson et al., 1988; Viehland & Mason, 1995). Only bulk values in CF₄ of transport coefficients can be experimentally determined (Robson, 1991). Due to significant particle losses in He⁺ in CF₄, the experimental transport coefficients were not measured. Although some experimental points for the cross sections of He⁺ ion scattering in CF₄ were obtained by (Fisher et al., 1990). A complete set of cross-sections for this system with more details is given in the paper (Nikitović et al., 2017). Quantum-mechanical calculation of a certain cross-section is a required task that requires knowledge of the surface potential energy of ions and molecules to be constructed from the structure of the reactants. Less intensive computational methods, such as the Denpoh-Nanbu theory (Denpoh & Nanbu, 1998; Nikitović et al., 2014; Petrović et al., 2007), require knowledge of thermodynamic formation data and are applicable to a range of molecules. Although thermodynamic formation data are known in this case, such an approach is difficult to apply, since the reaction does not take place via the excited (HeCF₄⁺ *) complex but via the excited CF₄⁺ (CF₄⁺ *) states. It is also more appropriate to select the limit energies for the reaction products from the energy thresholds of the CF₄⁺ state (Motohashi et al., 2005) than from the enthalpies of formation.

Ion charge transfer reactions with molecules are important elementary processes in modeling kinetics in all types of plasma. In many cases, it is known that the cross section for these reactions represents the most important part of the set of cross section. From the observation of the line spectra of excited F atoms obtained by spectrometric measurements (Motohashi et al., 2005) in CF₄, it can be concluded that the charge transfer reaction is the dominant process in collisions with inert gas ions. This argument seems to be enough to ignore other possible reactions. The aim of this paper is to report on a topic important for both basic studies and application. We estimated the set of cross sections for He⁺ in He/CF₄ using existing experimental data (Viehland et al., 2017; Basurto et al., 2000; Helm, 1977; Stefansson et al., 1988; Viehland & Mason, 1995). In the next section, we will discuss the compilation of existing data and establish one possible set of cross-sections. We will then describe the calculation of transport parameters and finally discuss our results. The coefficients of velocity, flux and bulk reduced mobilities, calculated from flux and bulk drift velocities by Monte Carlo simulation are significantly different in the region of moderate E/N.

2. Cross section sets

Our goal in this section will be to establish a set of cross sections because only the set of cross sections contains relevant information for calculating the transport properties of the selected ion in a given gas. In our chosen case, the general knowledge of the total cross-section indicates that at low energies they

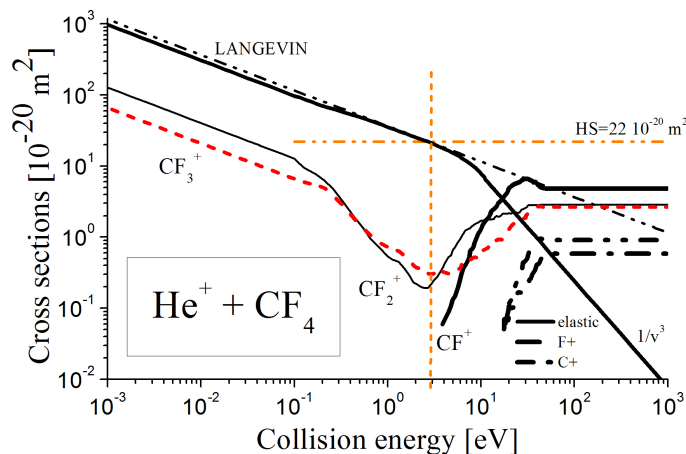


Figure 1.: Cross section set for $\text{He}^+ + \text{CF}_4$.

would be affected by attractive long-range forces, while at high energies they would be affected by repulsive forces.

For low energies, when the interaction potential is very close to the induced dipole potential, it can be assumed that the total cross section of the moment transfer is $\sigma_{mt} = 1.105 \sigma_L$ where σ_L is the Langevin cross section (McDaniel et al., 1970). The Langevin cross section was determined using the average gas polarizability. The average polarizability of CF_4 is poorly determined (Fisher et al., 1990) and can lead to deviations in the calculated ion mobility in CF_4 (Stojanović et al., 2014; Georgieva et al., 2003). As a consequence, this would affect the prediction of plasma parameters in modeling. The value of $3.86 \cdot 10^{-30} \text{ m}^3$ used by Stojanović et al. (2014) who found an excellent agreement between the experimental and the calculated reduced mobility of CF_3^+ ions in CF_4 .

From measurements of exothermic cross sections Fisher et al. (1990) for the production of CF_2^+ and CF_3^+ from $\text{He}^+ + \text{CF}_4$ it can be concluded that the scattering is appropriate to describe with induced polarization potential up to 0.2 eV. Thus, assuming that charge transfer reactions are the dominant interaction, a cross section of elastic moment transmission can be obtained by deduction of experimental reactive cross sections (Fisher et al., 1990) from the assumed total moment transfer.

Extrapolation of the behavior of the cross section of the transmission of elastic moment outside the Langevin point of intersection to the cross section of the soft sphere (Fisher et al., 1990) was done by smooth connection with the trend $1/v^3$ (Krstić & Schultz, 2009; Raspopović et al., 2015) where v is the center-velocity of mass (see Figure 1). Extrapolation is performed in the energy

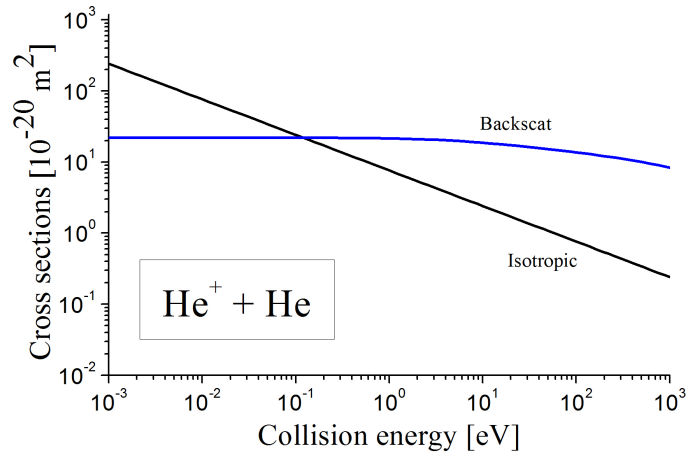


Figure 2.: Cross section set for He⁺ + He.

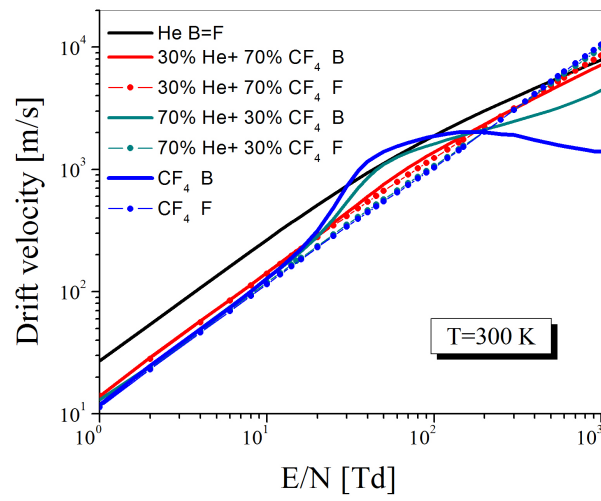


Figure 3.: Drift velocity for He⁺ in He/CF₄ mixtures as a function of E/N.

region where a repulsive interaction is expected to occur, which is estimated to be above about 3 eV. Finally, all exothermic and endothermic cross-sections of Fisher *et al.* (1990). Reactive cross sections were approximated by constant values at all kinetic energies of ions above 50 eV using data for the production ratio between the observed ions as proposed in (Parker & El-Ashhab, 1983).

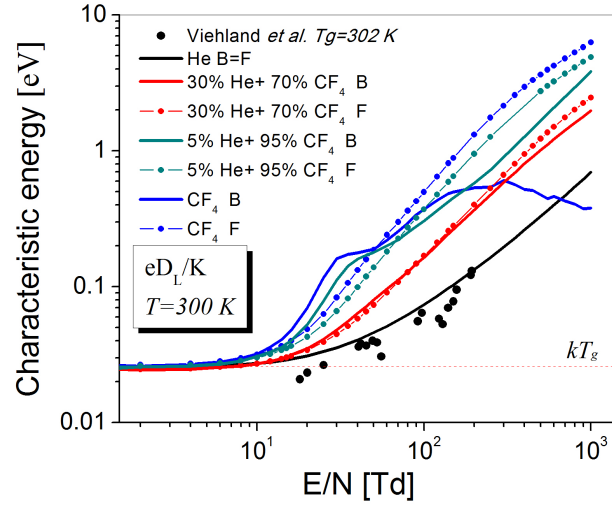


Figure 4.: Longitudinal characteristic energy for He^+ in He/ CF_4 mixtures as a function of E/N .

It was found that different extrapolations (short dot-dashed or dashed line in Figure 1) of unusual low energy behavior observed by cross-sectional measurement led to CF_2^+ formation (where exothermic reaction behavior is expected regardless of, He^+ spin state) have negligible impact on mobility. In the case of the system, He^+ on He, the Phelps sections taken from the database were used for (Phelps, 2011). The section consists of two components: Isotropic and Backscat is given in Figure 2.

3. Transport parameters

Transport properties needed for modeling CF_4 discharges containing He^+ ions are calculated by the Monte Carlo method. A code that properly takes into account thermal collisions was used (Ristivojevic & Petrović, 2012). It has passed all relevant benchmarks Fisher *et al.* (1990) and was tested in our work on several types of charged particles (Petrović *et al.*, 2007; de Urquijo *et al.*, 2013).

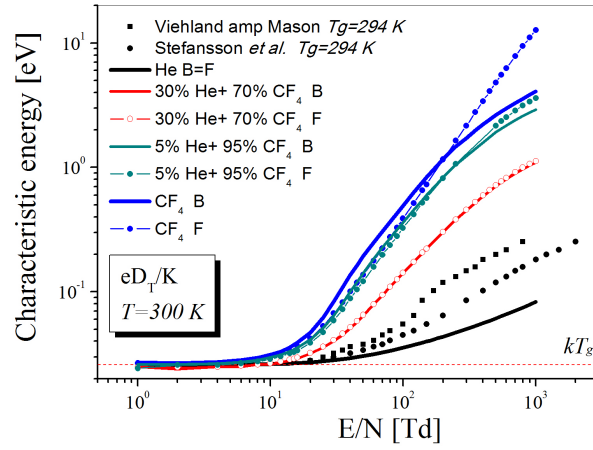


Figure 5.: Transversal characteristic energy for He⁺ in He/CF₄ mixtures as a function of E/N.

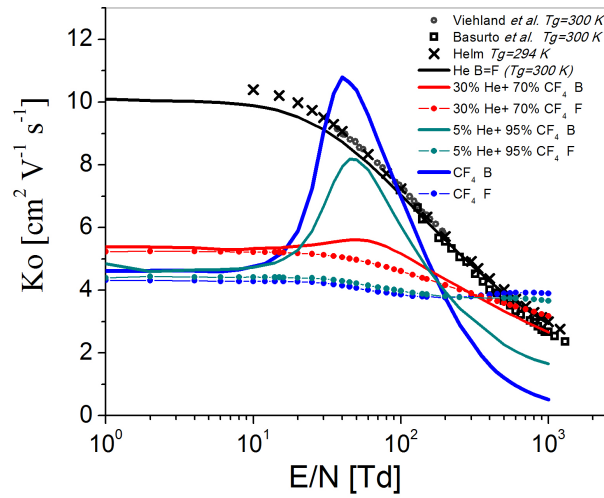


Figure 6.: The bulk and flux reduced mobility for He⁺ in He/CF₄ mixtures as a function of E/N.

Swarm parameters of He^+ in He/CF_4 mixtures for a temperature of $T=300$ K are presented.

The calculated transport parameters are the mean energy, characteristic energy, drift velocity, diffusion coefficients, ionization and attachment coefficients and chemical reaction coefficients for ions (Petrović et al., 2009). The excitation coefficients are also measured but seldom used in modeling. Note that these transport parameters are the only information present in the literature up to now and there are no published experimental data for the transport coefficients of He^+ in He/CF_4 mixtures. The transport parameters of He^+ ions swarm in neutral gases He and CF_4 , as well as in mixtures were calculated: (1) 5% He + 95% CF_4 (2) 30% He + 70% CF_4 and (3) 70% He + 30% CF_4 .

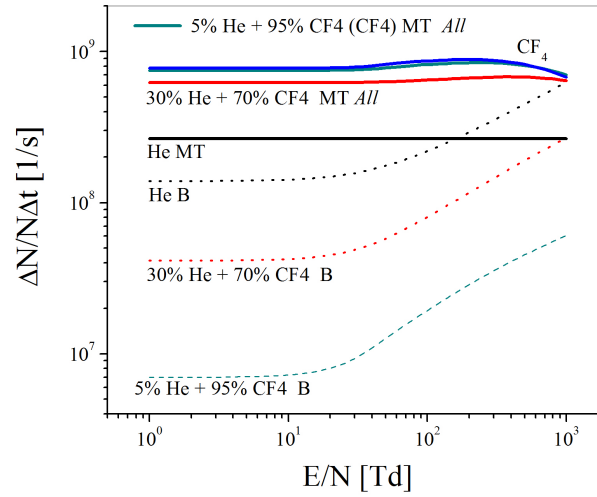


Figure 7.: Rate coefficients for He^+ in He/CF_4 mixtures as a function of E/N : momentum transfer.

The flux and bulk drift velocities (Robson et al., 2005; Ness & Robson, 1986; Nikitović et al., 2018; Nikitović & Raspopović, 2021) for He^+ in He/CF_4 mixtures as a function of E/N are given in Figure 3. The drift velocities obtained by the Monte Carlo simulation are calculated in real space (bulk) and in velocity space (flux) values which are obtained as $d \langle x \rangle / dt$ and $\langle v \rangle$, respectively. At low energies, at $E/N < 200$ Td due to intense formation of CF_3^+ and CF_2^+ ions in charge transfer reactions instead of He^+ ions, the center of mass of the swarm moves forward, so that the bulk velocity is greater than the flux. With further increase $E/N > 200$ Td when the high-energy ions from the distribution function increasingly have non-conservative collisions in which the CF^+ , C^+ and F^+ be-

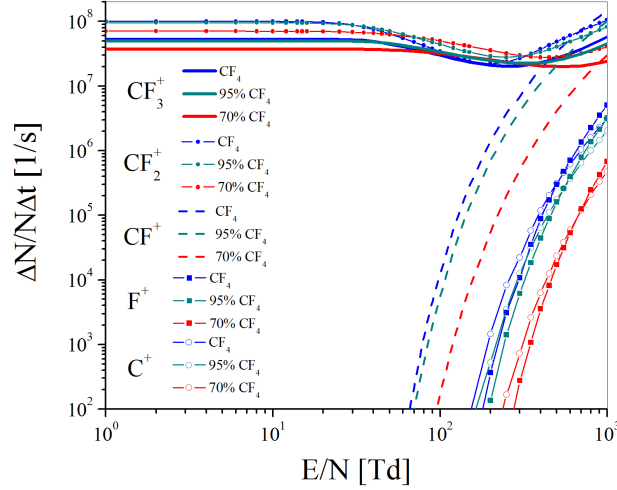


Figure 8.: Rate coefficients for He⁺ in He/CF₄ mixtures as a function of E/N: production reactions.

coming He⁺ ions disappear, shifting the center of mass of the swarm backward, resulting in a bulk velocity less than the flux.

In Figure 4 we present the characteristic energies (diffusion coefficient normalized to mobility D/K in units of eV) determined in the direction of the electric field. Figure 4) are shown that with increasing percentage of CF₄ molecules in the mixture with He there is an increase in bulk and flux values of longitudinal characteristic energy, except in the case of bulk values of eDL/K at CF₄ concentrations higher than 95% for $E/N > 40$ Td. Already 5% He⁺ ions in a mixture with CF₄ significantly reduces the differences between bulk and flux values of longitudinal characteristic energy, and in a mixture with 30% He these differences are still noticeable. Figure 4) also includes the experimentally measured values of eDL/K by Viehland et al. (2017) for the system He⁺ + He (black symbols).

The transversal characteristic energy also increases with increasing percentage of He/CF₄ mixtures (Figure 5). Smaller differences between bulk and flux values are in transversal compared to longitudinal characteristic energy. With 30% He in the mixture there is no difference between bulk and eDT/K flux. In Figure 5) the experimentally measured values of eDT/K by Stefansson et al. (1988) and Viehland & Mason (1995) for the system He⁺ + He (black symbols).

Reduced mobility for He⁺ ions in CF₄ as a function of E/N (E-electric field strength, N-gas number density) compared with bulk and flux values is shown in Figure 6. Significant peak in the bulk reduced mobility is obtained as a

result of difference in energy dependence of elastic and exothermic cross sections (Nikitović et al., 2019). Let us remind the reader that the bulk drift velocity ($W = d \langle x \rangle / dt$) is reaction corrected flux drift velocity ($w = \langle v \rangle$): $W = w + S$, where S is the term representing a measure of the effect of reactions on the drift velocity. Difference between bulk and flux reduced mobilities is a consequence of energy dependent reactions. We found that the cross section leading to formation of CF_2^+ (where irrespective of the He^+ spin state exothermic behavior of reaction is expected) are negligible on mobility.

Mobility of $\text{He}^+ + \text{CF}_4$ depending on E/N has a pronounced maximum at about 40 Td, while mobility of $\text{He}^+ + \text{He}$ does not; has a plateau at low E/N that immediately declines as a result of pronounced backscattering interaction. At low E/N higher values of K_0 for the $\text{He}^+ + \text{He}$ system than those for $\text{He}^+ + \text{CF}_4$ are due to less the reduced mass of the ion neutral pair. At low E/N bulk values for K_0 are higher than flux values as a consequence of low-energy capture of He^+ ions by CF_4 molecules in an exothermic reaction in which CF_3^+ ion is formed. At large E/N flux values are higher than the bulk values due to higher ion capture at high energies than at lower ones. With increasing He concentration in the mixture, the differences between bulk and flux values are significantly reduced. For a mixture of 30% He + 70% CF_4 these differences can be clearly seen only in the region of about 40 Td. In Figure 6 the experimentally measured values of K_0 by Viehland et al. (2017), Basurto et al. (2000) and Helm (1977) for the system $\text{He}^+ + \text{He}$ (black symbols).

In Figures 7 and 8 we show rate coefficients for elastic momentum transfer and for all reactive processes as a function of E/N . The rate coefficients as final output of our calculations is needed as input in fluid equations for description of ion transport in He/ CF_4 mixtures. The rate coefficients for all reactions presented in the cross-section sets are significantly different than one that should be obtained with cross sections obtained from statistical theories such as those obtained by Denpoh-Nanbu theory (Denpoh & Nanbu, 1998).

4. Conclusion

In this paper we have determined the cross section of elastic moment transport as a function of energy for He^+ scattering on CF_4 that can be used in modeling He^+ transport in He/ CF_4 mixtures. We used the data for a simple theoretical cross-section of the transmission of the total moment and obtained the cross-section of the transmission of the elastic moment by deduction of all experimentally obtained cross-sections of the charge transfer. In doing so, we assumed that the measured cross-sections of the charge transfer were collisions with the highest probability. Thus, in this paper, we have estimated the set of cross sections for He^+ ions in He/ CF_4 that can be used as an independent input in modeling He^+ ion transport. This estimation was performed using measured cross-sections of charge transfer.

Since, according to our knowledge, there is no direct information in the literature on how the mobility of high recombination energy ions, such as He⁺ ions, behave in He/CF₄ mixtures, we calculated transport parameters using the Monte Carlo simulation method (Nikitović et al., 2014; Nikitović et al., 2016, 2019).

In this work, we obtained and considered data on longitudinal and transversal characteristic energy, bulk and flux reduced mobility and rate coefficients. Data on swarm coefficients for positive and negative ions are required for hybrid and fluid codes (White et al., 2014) and the current focus on liquids or liquids in rare gas mixtures dictates the need to produce data compatible with these models. Given the current interest in liquid and / or liquid models in mixtures with rare gases, data on swarm coefficients for positive and negative ions for hybrid and fluid codes are needed. Atmospheric and near-atmospheric pressure glow discharges generated in both pure helium and helium-air mixtures have been studied using a plasma chemistry code originally developed for simulations of electron-beam-produced air plasmas.

Acknowledgements. The authors acknowledge funding provided by the Institute of Physics University of Belgrade, through the grant by the Ministry of Education, Science and Technological Development of the Republic of Serbia.

References

- Basurto, E., de Urquijo, J., Alvarez, I., & Cisneros, C., Mobility of He⁺, Ne⁺, Ar⁺, N⁺₂, O⁺₂, and CO⁺₂ in their parent gas. 2000, *Phys. Rev. E*, **61**, 3053, DOI: 10.1103/PhysRevE.61.3053
- Bošnjaković, D., Ph Dissertation. 2016, *Faculty of Electrical Engineering, University of Belgrade, Belgrade, Serbia*
- de Urquijo, J., Jovanović, J. V., Bekstein, A., Stojanović, V., & Petrović, Z. L., Ion mobilities and transport cross sections of daughter negative ions in N₂O and N₂O-N₂ mixtures. 2013, *Plasma Sources Sci. Technol.*, **22**, 025004, DOI: 10.1088/0963-0252/22/2/025004
- Denpoh, K. & Nanbu, K., Self-consistent particle simulation of radio-frequency CF₄ discharge with implementation of all ion-neutral reactive collisions. 1998, *J. Vac. Sci. Technol. A*, **16**, 1201, DOI: 10.1116/1.581259
- Fisher, E. R., Weber, M. E., & Armentrout, P. B., Dissociative charge transfer reactions of Ar⁺, Ne⁺, and He⁺ with CF₄ from thermal to 50 eV. 1990, *J. Chem. Phys.*, **92**, 2296, DOI: 10.1063/1.457969
- Fraga, M. M. F. R., Fraga, F. A. F., Fetal, S. T. G., et al., The GEM scintillation in He-CF₄, Ar-CF₄, Ar-TEA and Xe-TEA mixtures. 2003, *Nucl. Instrum. Meth. in Phys. Res. A*, **504**, 88, DOI: 10.1016/S0168-9002(03)00758-7
- Georgieva, V., Bogaerts, A., & Gijbels, R., Particle-in-cell/Monte Carlo simulation of a capacitively coupled radio frequency Ar/CF₄ discharge: Effect of gas composition. 2003, *J. Appl. Phys.*, **93**, 2369, DOI: 10.1063/1.1542920

- Helm, H., The cross section for symmetric charge exchange of He^+ in He at energies between 0.3 and 8 eV. 1977, *J. Phys. B*, **10**, 3683, DOI: 10.1088/0022-3700/10/18/025
- Kaboth, A., Monroe, J., Ahlen, S., et al., A measurement of photon production in electron avalanches in CF_4 . 2008, *Nucl. Instrum. Meth. in Phys. Res. A*, **592**, 63, DOI: 10.1016/j.nima.2008.03.120
- Krstić, P. S. & Schultz, D. R., Elastic and related transport cross sections for singly charged ion-atom scattering of light metals (Li, Be, B) and hydrogen. 2009, *J. Phys. B: At. Mol. Opt. Phys.*, **42**, 065207, DOI: 10.1088/0953-4075/42/6/065207
- McDaniel, E. W., Cermak, V., & Ferguson, E. E. 1970, *Ion-molecule reactions*
- Motohashi, K., Takahashi, T., Takahashi, N., & Tsurubuchi, S., Emission cross sections in low-energy collisions between He^+ , Ne^+ ions and CF_4 molecule. 2005, *J. Phys. B: At. Mol. Opt. Phys.*, **38**, 3339, DOI: 10.1088/0953-4075/38/18/005
- Ness, K. F. & Robson, R. E., Velocity distribution function and transport coefficients of electron swarms in gases. II. Moment equations and applications. 1986, *Phys. Rev. A*, **34**, 2185, DOI: 10.1103/PhysRevA.34.2185
- Nikitović, Ž., Raspopović, Z., Stojanović, V., & Jovanović, J., Transport parameters of F^- ions in Ar/ BF_3 mixtures. 2014, *EPL*, **108**, 35004, DOI: 10.1209/0295-5075/108/35004
- Nikitović, Ž. D. & Raspopović, Z. M., Rate coefficients for Ar^+ in Ar/ BF_3 mixtures. 2021, *Eur. Phys. J. D*, **75**, 118, DOI: 10.1140/epjd/s10053-021-00061-3
- Nikitović, Ž. D., Raspopović, Z. M., & Stojanović, V. D., Reduced mobility of He^+ in CF_4 . 2017, *Plasma Sources Sci. Technol.*, **26**, 044004, DOI: 10.1088/1361-6595/aa61db
- Nikitović, Ž. D., Raspopović, Z. M., & Stojanović, V. D., Cross sections set and transport coefficients for Ar^+ in Ar/ CF_4 mixtures. 2018, *Eur. Phys. J. D*, **72**, 168, DOI: 10.1140/epjd/e2018-90059-1
- Nikitović, Ž. D., Raspopović, Z. M., & Stojanović, V. D., Reduced mobility of Ar^+ in Ar/ BF_3 mixtures. 2019, *EPL*, **128**, 15001, DOI: 10.1209/0295-5075/128/15001
- Nikitović, Ž. D., Stojanović, V. D., & Raspopović, Z. M., Modeling elastic momentum transfer cross-sections from mobility data. 2016, *EPL*, **114**, 25001, DOI: 10.1209/0295-5075/114/25001
- Parker, J. E. & El-Ashhab, F. S. M., Charge-transfer reactions of carbon tetrafluoride. 1983, *Int. J. Mass Spectrom. Ion. Phys.*, **47**, 159, DOI: 10.1016/0020-7381(83)87160-5
- Petrović, Z. L., Dujko, S., Marić, D., & Malović, G., & Nikitović, O. Šašić, J Jovanović, V Stojanović, and M Radmilović-Radjenović. Measurement and interpretation of swarm parameters and their application in plasma modelling. 2009, *J. Phys. D: Appl. Phys.*, **42**, 194002, DOI: 10.1088/0022-3727/42/19/194002
- Petrović, Z. L., Raspopović, Z. M., Stojanović, V. D., et al., Data and modeling of negative ion transport in gases of interest for production of integrated circuits and nanotechnologies. 2007, *J. Appl. Surf. Sci.*, **253**, 6619, DOI: 10.1016/j.apsusc.2007.02.005

- Phelps, A. 2011, database, <https://nl.lxcat.net/cache/62710de742cec/>, [Online; accessed 19-July-2022]
- Raspopović, Z., Stojanović, V., & Nikitović, Ž., Effect of exothermic reactions on the mobility of Ar⁺ in CF₄. 2015, *EPL*, **111**, 45001, DOI: 10.1209/0295-5075/111/45001
- Ristivojevic, Z. & Petrović, Z. L., A Monte Carlo simulation of ion transport at finite temperatures. 2012, *Plasma Sources Sci. Technol.*, **21**, 035001, DOI: 10.1088/0963-0252/21/3/035001
- Robson, R. E., Transport phenomena in the presence of reactions: Definition and measurement of transport coefficients. 1991, *Aust. J. Phys.*, **44**, 685, DOI: 10.1071/PH910685
- Robson, R. E., White, R. D., & Petrović, Z. L., Colloquium: Physically based fluid modeling of collisionally dominated low-temperature plasmas. 2005, *Rev. Mod. Phys.*, **77**, 1303, DOI: 10.1103/RevModPhys.77.1303
- Stefansson, T., Berge, T., Lausund, R., & Skullerud, H. R., Measurements of transport coefficients for lithium ions in argon and helium ions in helium with a drift-tube mass spectrometer. 1988, *J. Phys. D*, **21**, 1359, DOI: 10.1088/0022-3727/21/9/008
- Stojanović, V., Raspopović, Z., Jovanović, J. V., de Urquijo, J., & Petrović, Z. L., Mobility of positive ions in CF₄. 2014, in *Journal of Physics Conference Series*, Vol. **514**, *J. Phys.:Conf. Series*, 012059
- Viehland, L. A., Lutfullaeva, A., Dashdorj, J., & Johnsen, R., Accurate gaseous ion mobility measurements. 2017, *International Journal for Ion Mobility Spectrometry*, **20**, 95, DOI: 10.1007/s12127-017-0220-0
- Viehland, L. A. & Mason, E. A., Transport Properties of Gaseous Ions over a Wide Energy Range, Part IV. 1995, *At. Data. Nucl. Data Tables*, **60**, 37, DOI: 10.1006/adnd.1995.1004
- White, R., Tattersall, W., Boyle, G., et al., Low-energy electron and positron transport in gases and soft-condensed systems of biological relevance. 2014, *Appl. Radiat. Isot.*, **83**, 77, DOI: <https://doi.org/10.1016/j.apradiso.2013.01.008>

Electron-impact processes involving small molecular ions relevant for the astrochemistry

V.A. Srećković¹, L.M. Ignjatović¹ and M.S. Dimitrijević^{2,3}

¹ *Institute of Physics Belgrade, University of Belgrade, Pregrevica 118, 11080 Belgrade, Serbia (E-mail: vlada@ipb.ac.rs)*

² *Astronomical Observatory, Volgina 7, 11060 Belgrade, Serbia (E-mail: mdimitrijevic@aob.rs)*

³ *Observatoire de Paris, PSL Universit, CNRS, Sorbonne Universit, F-92195 Meudon, France*

Received: July 28, 2022; Accepted: October 1, 2022

Abstract. We investigated the electron-impact processes involving hydrogen, lithium and sodium molecular cations. Rate coefficients for the dissociative recombination in domains of principal quantum numbers $n \geq 4$ and temperatures from 500 K to 10 000K are reported. Considered collisional processes have an impact on the ionization level and atom excited-state populations as well on optical characteristics. The data are useful for the modeling of the kinetics of the Early Universe and for geocosmical plasma investigation.

Key words: atomic data – line profiles – Early Universe – astrophysical plasma–optical characteristics

1. Introduction

In modern science researchers are very interested in collision processes that involve hydrogen and alkali atoms and molecules (Iacob et al., 2019; Ignjatović et al., 2019, 2020; Coppola et al., 2013; Klyucharev et al., 2007). The reason is because of how they affect the spectral properties of astrophysical and laboratory plasmas (Srećković et al., 2014; Tielens, 2013; Beuc et al., 2018a). The ionization level, atom excited-state populations, and optical characteristics can all be affected by collisional events that involve electrons, atoms, ions, and small molecule ions (Schneider et al., 1991; Mihajlov et al., 2011; Srećković et al., 2017; Beuc et al., 2018b; Majlinger et al., 2020).

Atomic hydrogen, helium, lithium, and their cations are said to have been the first species generated by the nucleosynthetic activity that occurred after the Big Bang, according to theories of the early Universe (Epée Epée et al., 2022; Tielens, 2013). Later, simple molecules and their cations were created by the reactions of atoms. Dissociative recombination affects these molecules and molecules ions (Coppola et al., 2011; Djuissi et al., 2020).

For the examples involving lithium, sodium, and hydrogen, we obtained rate coefficients for dissociative recombination. For a wide range of parameters ($500 \text{ K} \leq T \leq 5\,000 \text{ K}$) and principal quantum numbers up to 20, the collisional data are acquired. Our goal is to produce high-quality data that can be correctly incorporated into current codes [Hauschildt & Baron \(2010\)](#); [Hubeny & Lanz \(2017\)](#) and databases for modeling planetary atmospheres, laboratory plasma, geocosmic plasma, and the ionosphere [Albert et al. \(2020\)](#); [Marinković et al. \(2017\)](#). The presented data may be of interest and for investigation and modelling of sodium clous on Iovian satellites Io [Grava et al. \(2014\)](#) and Europa [Leblanc et al. \(2005\)](#).

1.1. The method

We investigated the collisional processes i.e. electron driven processes involving molecular cations



Here A are hydrogen, lithium or sodium atoms in the ground states, $A^*(n)$ are highly excited atom i.e. Rydberg atoms, A_2^+ are the molecular ions in the ground electronic states.

The calculations were performed within the DRM i.e., the collisional reactions (1) have been treated by the so-called dipole resonant mechanism (DRM). In this characterization, the processes are caused by the dipole part of the electrostatic interaction between the outer highly excited i.e. Rydberg electron and the inner (ion-atom) system. This method is especially effective when used with the so-called decay approximation. A thorough and detailed description can be discovered in paper of Mihajlov and coworkers ([Mihajlov et al., 2012](#); [Mihajlov et al., 2003](#)). Here, we present a brief description of the method with the basic theory.

We use the DRM to obtain the rate coefficients for the principal quantum number $4 \leq n \leq 20$ and for temperatures from 500 K to 10000 K. The data are presented and discussed in details in Section 2.

1.2. The obtained quantities

Rate coefficients for the dissociative recombination can be expressed as

$$K_r = C_n(T) \cdot \int_{R_{min}}^{R_n} \exp \left[\frac{U_{12}(R)}{kT} - \frac{U_1(R)}{kT} \right] \cdot X(R, T) \cdot \frac{R^4 dR}{a_0^5} \quad (2)$$

in accordance with the theory from ([Mihajlov et al., 2003, 2011](#)). Here $U_{12}(R) = U_2(R) - U_1(R)$, R is the internuclear distance, and $U_1(R)$ and $U_2(R)$ are the ground and first excited electronic states of the molecular ion. R_n is the largest root of the equation $U_{12}(R) = I_n$, and R_{min} is determined as in [Mihajlov et al.](#)

(2003). Quantity $C_n(T)$ is given by

$$C_n(T) = \frac{(2\pi)^{5/2}}{3^{3/2}} \frac{(\hbar e a_0)^2}{(mkT)^{3/2}} n^{-3} \exp\left(\frac{I_n}{kT}\right). \quad (3)$$

I_n denotes the ionization energy of the excited atom. Parameter $X(R, T)$ can be given by

$$X(R, T) = \begin{cases} \gamma\left(\frac{3}{2}; -\frac{U_1(R)}{kT}\right) / \Gamma\left(\frac{3}{2}\right) & U_1 < 0, \\ 0, & U_1 \geq 0 \end{cases} \quad (4)$$

where γ and Γ are incomplete gamma functions.

Various atmosphere models [Hauschildt & Baron \(2010\)](#) and spectrum synthesis codes [Hubeny & Lanz \(2017\)](#) depend on the rate coefficients and cross sections as input parameters. Our aim is to determine high quality data in order to be properly included in modern codes and databases for modelling planetary atmospheres, early Universe chemistry, geocosmic plasma, etc ([Albert et al., 2020](#); [Jevremović et al., 2020](#); [Marinković et al., 2017](#)).

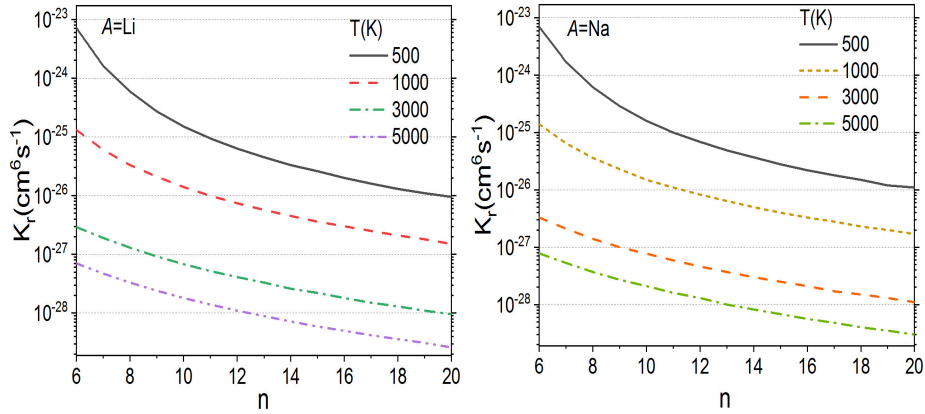


Figure 1. Left: Calculated values for rate coefficient Kr ($\text{cm}^6 \text{s}^{-1}$) as a function of n and T for lithium case ($A=\text{Li}$ in Eq(1)); Right: Calculated values for rate coefficient Kr ($\text{cm}^6 \text{s}^{-1}$) as a function of n and T for sodium case ($A=\text{Na}$ in Eq(1)).

2. Results and Discussion

The data i.e. the total recombination rate coefficients $Kr(n, T)$, obtained by Eq. (2), for lithium and sodium are presented in figure 1. The figs. 1a,b cover the

region $6 \leq n \leq 20$ and $500 \text{ K} \leq T \leq 5000 \text{ K}$. One can see that probability for dissociative recombination is higher for lower n and lower temperature. Thus apparently these collisions become one of the main reactions for the creation of Rydberg atoms for investigated environment under these conditions. Similar behavior is for the case of hydrogen i.e. $A = \text{H}$.

Table 1. The coefficients in the Eq.(5) for lithium case corresponding to the rate coefficient obtained by Eq.(2).

n	ζ_0	ζ_1	ζ_2
6	7.43209	- 16.86487	2.03664
10	-11.4306	- 6.51424	0.57043
15	-16.69436	- 3.79753	0.18394
18	-17.92629	- 3.24067	0.10772
20	-18.19294	- 3.16733	0.09762

To enable an easier use of data, we give for recombination rate coefficient a simple logarithmic second-degree polynomial formula, with n -dependent coefficients $\zeta_i(n)$. A straightforward analytical expression for the dissociative recombination rate coefficient $K_r(n, T)$

$$\log(K_r(n, T)) = \sum_{i=0}^2 \zeta_i(n) \cdot (\log(T))^i \quad (5)$$

is valid in region of investigated plasma parameters in this study.

The selected fits (for $6 \leq n \leq 20$) for lithium and sodium collisions are listed in Tabs. 1 and 2. $A = \text{H}$ fits (for $4 \leq n \leq 8$) are listed in Tab. 3.

Table 2. The coefficients in the Eq.(5) for sodium case corresponding to the rate coefficient obtained by Eq.(2).

n	ζ_0	ζ_1	ζ_2
6	6.30554	- 16.17964	1.93667
10	-11.24121	- 6.63408	0.59369
15	-16.41778	- 3.96127	0.21307
18	-17.73199	- 3.33623	0.12335
20	-17.96593	- 3.2857	0.11752

The fits are valid within the temperature range $500 \leq T \leq 5000 \text{ K}$ for lithium and sodium collisions and $3000 \leq T \leq 10000 \text{ K}$ for hydrogen case in reaction (1).

Table 3. The coefficients in the Eq.(5) for hydrogen case corresponding to the rate coefficient obtained by Eq.(2).

n	ζ_0	ζ_1	ζ_2
4	61.86661	- 42.61027	4.94202
5	-15.9987	- 4.15003	0.20879
6	-18.32435	- 3.07864	0.07813
7	-19.66572	- 2.49104	0.00637
8	-20.04561	- 2.38883	-0.00388

3. Summary

In this paper we have calculated the rate coefficients for the dissociative recombination in domains of principal quantum numbers $n \geq 4$ and temperatures from 500 K to 10 000 K for the electron-impact processes involving hydrogen H_2^+ , lithium Li_2^+ and sodium Na_2^+ molecular cations. The numerical data show that the investigated processes have a considerable impact on the atom excited-state populations and ionization levels and consequently on the optical properties in the weakly ionized layers of atmospheres of various stars. Moreover the provided collisional data are ready to be used in the early Universe chemistry, modeling of interstellar medium and cold plasmas.

Acknowledgements. The authors acknowledge the support from the Institute of Physics, Belgrade, which was made possible by grants from the Ministry of Education, Science and Technological Development of the Republic of Serbia. This article is based upon work from COST Action CA18212 - Molecular Dynamics in the GAS phase (MD-GAS), supported by COST (European Cooperation in Science and Technology). We would also like to express our gratitude to Magdalena Christova for her time and effort put into this work, as well as for a fruitful discussion.

References

- Albert, D., Antony, B. K., Ba, Y. A., et al., A Decade with VAMDC: Results and Ambitions. 2020, *Atoms*, **8**, 76, DOI: 10.3390/atoms8040076
- Beuc, R., Movre, M., & Pichler, G., High Temperature Optical Spectra of Diatomic Molecules at Local Thermodynamic Equilibrium. 2018a, *Atoms*, **6**, 67, DOI: 10.3390/atoms6040067
- Beuc, R., Peach, G., Movre, M., & Horvati, B., Lithium, sodium and potassium resonance lines pressure broadened by helium atoms. 2018b, *Astronomical and Astrophysical Transactions*, **3**, 315
- Coppola, C. M., Galli, D., Palla, F., Longo, S., & Chluba, J., Non-thermal photons and H_2 formation in the early Universe. 2013, *MNRAS*, **434**, 114, DOI: 10.1093/mnras/stt1007

- Coppola, C. M., Longo, S., Capitelli, M., Palla, F., & Galli, D., Vibrational Level Population of H_2 and H_2^+ in the Early Universe. 2011, *The Astrophysical Journal Supplement Series*, **193**, 7, DOI: 10.1088/0067-0049/193/1/7
- Djuissi, E., Bogdan, R., Abdoulanziz, A., et al., Electron driven reactive processes involving H^+H_2 and HD^+ molecular cations in the Early Universe. 2020, *Romanian Astronomical Journal*, **30**, 101
- Epée Epée, M. D., Motapon, O., Pop, N., et al., Dissociative recombination and rotational transitions of D_2^+ in collisions with slow electrons. 2022, *MNRAS*, **512**, 424, DOI: 10.1093/mnras/stac501
- Grava, C., Schneider, N. M., Leblanc, F., et al., Solar control of sodium escape from Io. 2014, *Journal of Geophysical Research (Planets)*, **119**, 404, DOI: 10.1002/2013JE004504
- Hauschildt, P. H. & Baron, E., A 3D radiative transfer framework. VI. PHOENIX/3D example applications. 2010, *Astronomy and Astrophysics*, **509**, A36, DOI: 10.1051/0004-6361/200913064
- Hubeny, I. & Lanz, T., A brief introductory guide to TLUSTY and SYNSPEC. 2017, *arXiv e-prints*, arXiv:1706.01859
- Iacob, F., Pop, N., Mezei, J. Z., et al., Recombination and excitation of molecular cations with electrons: Application to, H_2^+ , BeD^+ and BeT^+ . 2019, in American Institute of Physics Conference Series, Vol. **2071**, *Tim 18 Physics Conference*, 020007
- Ignjatović, L. M., Srećković, V. A., & Dimitrijević, M. S., The collisional atomic processes of Rydberg alkali atoms in geo-cosmical plasmas. 2019, *MNRAS*, **483**, 4202, DOI: 10.1093/mnras/sty3294
- Ignjatović, L. M., Srećković, V. A., & Dimitrijević, M. S., Photoionization of the alkali molecular ions in geo-cosmical plasmas. 2020, *Contributions of the Astronomical Observatory Skalnaté Pleso*, **50**, 187, DOI: 10.31577/caosp.2020.50.1.187
- Jevremović, D., Srećković, V. A., Marinković, B. P., & Vujčić, V., Databases for collisional and radiative processes in small molecules needed for spectroscopy use in astrophysics. 2020, *Contributions of the Astronomical Observatory Skalnaté Pleso*, **50**, 44, DOI: 10.31577/caosp.2020.50.1.44
- Klyucharev, A. N., Bezuglov, N. N., Matveev, A. A., et al., Rate coefficients for the chemi-ionization processes in sodium- and other alkali-metal geocosmical plasmas. 2007, *New Astronomy Review*, **51**, 547, DOI: 10.1016/j.newar.2007.05.001
- Leblanc, F., Potter, A. E., Killen, R. M., & Johnson, R. E., Origins of Europa Na cloud and torus. 2005, *Icarus*, **178**, 367, DOI: 10.1016/j.icarus.2005.03.027
- Majlinger, Z., Dimitrijević, M. S., & Srećković, V. A., Stark Broadening of Co II Lines in Stellar Atmospheres. 2020, *Data*, **5**, 74, DOI: 10.3390/data5030074
- Marinković, B. P., Jevremović, D., Srećković, V. A., et al., BEAMDB and MolD - databases for atomic and molecular collisional and radiative processes: Belgrade nodes of VAMDC. 2017, *European Physical Journal D*, **71**, 158, DOI: 10.1140/epjd/e2017-70814-6

- Mihajlov, A., Srećković, V., Ignjatović, L. M., & Klyucharev, A., The Chemi-Ionization Processes in Slow Collisions of Rydberg Atoms with Ground State Atoms: Mechanism and Applications. 2012, *Journal of Cluster Science*, **23**, 47, DOI: 10.1007/s10876-011-0438-7
- Mihajlov, A. A., Ignjatović, L. M., Dimitrijević, M. S., & Djurić, Z., Symmetrical Chemi-Ionization and Chemi-Recombination Processes in Low-Temperature Layers of Helium-rich DB White Dwarf Atmospheres. 2003, *The Astrophysical Journal Supplement Series*, **147**, 369, DOI: 10.1086/375621
- Mihajlov, A. A., Ignjatović, L. M., Srećković, V. A., & Dimitrijević, M. S., Chemi-ionization in Solar Photosphere: Influence on the Hydrogen Atom Excited States Population. 2011, *The Astrophysical Journal Supplement Series*, **193**, 2, DOI: 10.1088/0067-0049/193/1/2
- Schneider, I. F., Dulieu, O., & Giusti-Suzor, A., The role of Rydberg states in H^+_2 dissociative recombination with slow electrons. 1991, *Journal of Physics B Atomic Molecular Physics*, **24**, L289, DOI: 10.1088/0953-4075/24/12/002
- Srećković, V., Ignjatović, L., Jevremović, D., Vujčić, V., & Dimitrijević, M., Radiative and Collisional Molecular Data and Virtual Laboratory Astrophysics. 2017, *Atoms*, **5**, 31, DOI: 10.3390/atoms5030031
- Srećković, V. A., Mihajlov, A. A., Ignjatović, L. M., & Dimitrijević, M. S., Ion-atom radiative processes in the solar atmosphere: quiet Sun and sunspots. 2014, *Advances in Space Research*, **54**, 1264, DOI: 10.1016/j.asr.2013.11.017
- Tielens, A. G. G. M., The molecular universe. 2013, *Reviews of Modern Physics*, **85**, 1021, DOI: 10.1103/RevModPhys.85.1021

The usage of perceptron, feed and deep feed forward artificial neural networks on the spectroscopy data: astrophysical & fusion plasmas

N.M. Sakan , I. Traparić, V.A. Srećković  and M. Ivković

*Institute of Physics Belgrade, University of Belgrade, Pregrevica 118, 11080
Belgrade, Serbia (E-mail: nsakan@ipb.ac.rs)*

Received: July 28, 2022; Accepted: October 1, 2022

Abstract. Artificial neural networks are gaining a momentum for solving complex problems in all sorts of data analysis and classification matters. As such, idea of determining their usability on complex plasma came up. The choice for the input data for the analysis is a set of stellar spectral data. It consists of complex composition plasma under vast variety of conditions, dependent on type of star, measured with calibrated standardized procedures and equipment. The results of the analysis has shown that even a simple type of perceptron artificial neural network could lead to results of acceptable quality for the analysis of spectra of complex composition. The analyzed ANNs performed good on a limited data set. The results can be interpreted as a figure of merit for further development of complex neural networks in various applications e.g. in astrophysical and fusion plasmas.

Key words: Atomic processes–Line: profiles–astrophysical & fusion plasmas

1. Introduction

The usage of machine learning algorithms is a growing field of research (D’Isanto et al., 2016; Baron, 2019; Kates-Harbeck et al., 2019). Since the computer power is constantly growing its usage is often found in a wide variety of applications: from determination of objects on a photograph all the way to expert systems capable to determine adequate states and predicted outcomes of complex systems; from difficult-to-maintain machines states and prediction of conditions, up to the assistance in human health monitoring.

Even the specific fields of spectroscopy rely deeply on artificial neural networks, as is the case for instance with medical spectroscopy application Wang et al. (2015), or for instance agricultural application Basile et al. (2022); Longin et al. (2019). The material recognition in extraterrestrial spectroscopic probing is also a very difficult task, since the limitations of the mass and resolving power of the onboard instruments are a very difficult limiting factor (Koujelev et al., 2010; Bornstein et al., 2005).

Usage of the artificial neural networks (ANN) fell into focus of our interest because of flexibility of their application, as well as a variety of complex problems that they have already solved.

All of the mentioned has been a factor for applying neural networks to the decision process of determining a stellar spectral type as an example of application on astrophysical data (Albert et al., 2020). Artificial neural networks are often used in astrophysics (e.g. for the integral field spectral analysis of galaxies in Hampton et al. 2017). There is an expectation of development of further focus on convolutional neural networks application on spectroscopic data (Castorena et al., 2021). Also, even more complex predictions based on back-propagation in neural networks as well as complex artificial neural networks structures in spectroscopic usage are known (Li et al., 2017). In order to have insight of applicability of the ANN usage we have limited our research on simplest case as a figure of merit.

Few random spectral curves from database Pickles (1998) are presented here in results. Entire database set consists of spectra for 12 types of stars, spectral type O normal; B normal; A normal; F normal; F Metal rich; F metal weak; G normal; G Metal rich; G metal weak; K normal; K Metal rich; K metal weak; and M normal. Our aim was to create test case as a method of determining a quality of specific ANN in various machine learning analysis, from stellar and fusion spectra analysis, material analysis, up to extremely specific cases as enhancing a low resolution instrument performance for specific applications (Marinković et al., 2019; Albert et al., 2020).

2. ANN basics and principles

The usage of systems related to the functions of neural networks has been in focus of investigation since mid-1940 McCulloch & Pitts (1943), but the real usage has evolved with the application of modern day digital computers, which enabled construction of networks of enlarged complexity. One of the simplest neural networks, that could be seen more as a test case of validity of operation of artificial intelligence systems, is perceptron (Rosenblatt, 1958). The prediction as well as sensitivity of the training data set is in favor of more complex networks. It is the primary goal of our investigation, along with their application on spectral data sets and measurements.

The choice for the dataset was made on open access data files for the 131 stellar spectra published by Pickles (1998) (available at accompanying reference appended to the bibliographical entry, as seen in May 2022). The results are promising and further research on the field is expected. The quality of the trained artificial neural network prediction is related to the data set as well as its structure. An effort of applying it on a large scale dataset or database should be carried out.

The problem of finding out a category of data subset is an inherent problem for any sort of machine learning and as such for the artificial neural networks also. The artificial neural network is a system of mathematical functions trying to resemble a simplified animal brain. The network consists of artificial neurons.

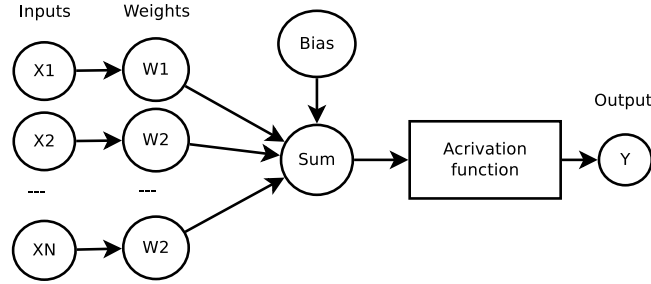


Figure 1. The concept of a neuron. Schematic presentation.

A neuron is described as a function that adopts output value based on its input values and bias value by the means of reaction function. The simplest neuron concept could be seen on a Figure 1. The neuron determines its output state as an output of activation function based on a weighted sum of input values and a bias value itself, and could be described by equation

$$y_{out} = f_{act} \left(Bias + \sum_{i=1}^N x_i w_i \right), \quad (1)$$

where f_{act} is a activation function, x_i and w_i are the i -th input value as well as adequate input weight.

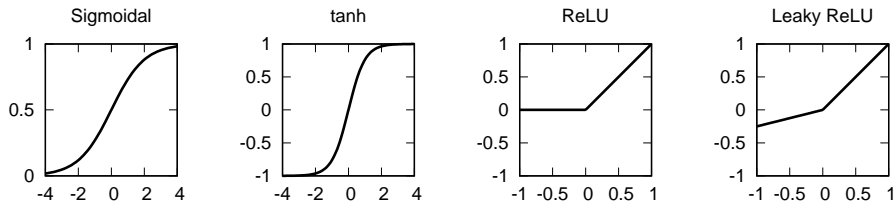


Figure 2. Four most common neuron reaction functions.

The neuron reaction on external stimulus is strongly dependent on its reaction function. In order to determine the neuron behavior on a micro scale, the reaction function as well as the method of adopting the weight values plays a determining role. Four most common reaction functions are shown on Figure 2.

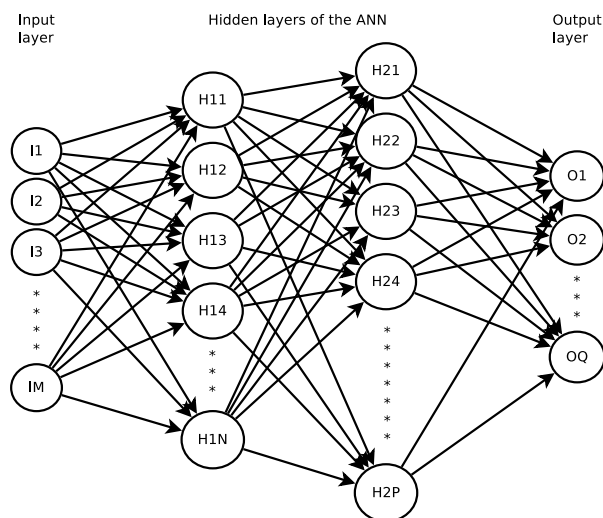


Figure 3. Concept of ANN of perceptron, feed forward and deep feed forward. The shown ANN consists of M input neurons, two hidden layers of N and P neurons and output layer of Q neurons.

A topology of the neural network as well as the learning method are determining the global reaction of the neural network. For the goal of usability analysis the simplest ANN topologies, perceptron, is chosen. The Feed Forward and Deep Feed Forward topologies are based upon fully connected dense layers of neurons, see Figure 3. The two specific layers, input and output, have the dimensionality of the input data and output states consequently and are the only limiting factors of the network. When there is more than one hidden layer, the neural network is considered to be the deep one.

3. Results and discussion

In Figure 4 several random spectral curves from database Pickles (1998) are presented. Entire dataset consists of spectra for 12 types of stars, spectral type O normal; B normal; A normal; F normal; F Metal rich; F metal weak; G normal; G Metal rich; G metal weak; K normal; K Metal rich; K metal weak; and M normal. Each epoch of the dataset was divided into 70% for training set and 30% for the test set.

As a test bench for the application of the ANN to the selection set of perceptron, Feed Forward and Deep Feed Forward networks are used. As a reaction function ReLU (rectified linear unit) was used, and the input data was normalized to unit using standardization

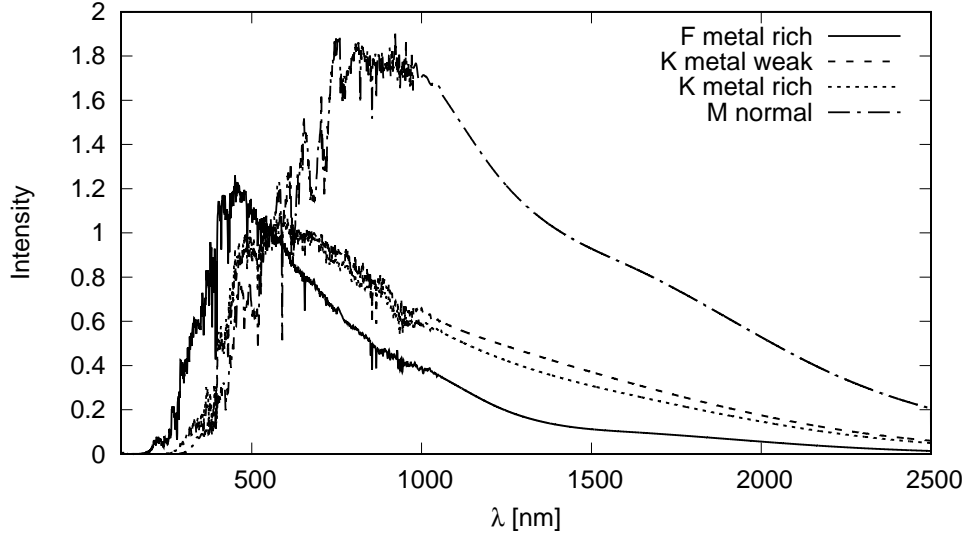


Figure 4. Several sample spectra. Spectra i.e. data is taken from [Pickles \(1998\)](#).

$$x' = \frac{x - \mu}{\sigma}, \quad \hat{\mu} = \frac{1}{N} \sum_{i=1}^N x_i, \quad \hat{\sigma} = \sqrt{\frac{1}{N-1} \sum_{i=1}^N (x_i - \hat{\mu})^2}. \quad (2)$$

No additional data preparation was imposed. The investigated neural network topologies were let to train on the set of data for 200 epochs. Input layer consisted of 4771 input values of available data, output layer consisted of 12 types of stars, spectral type O normal; B normal; A normal; F normal; F Metal rich; F metal weak; G normal; G Metal rich; G metal weak; K normal; K Metal rich; K metal weak; and M normal. The hidden layers consisted of 5000 neurons in first, 1000 in second and 512 neurons in third layer. They were included consequently in order to compare ANN behavior, see Figure 5.

It is obvious, by the analysis of calculated data presented in Figure 5, that the deeper ANNs are capable to learn faster and have better predictions after smaller epochs of learning. This capability is a winning solution in the case of complex spectra. The ANN could fall into pseudo stable states and produce a non-minimal error. Such falls into local minimum state could be avoided by several advanced methods one of which is providing an algorithm for forgetting of the learned state, e.g. algorithm that disturbs a learned state after each application.

Also, there are probably better methods for the input dataset preparation, from pure mathematical procedures up to convolutional ANN (CNN) incorporation. It is proven that, even in its simplest forms, ANN could be used for such

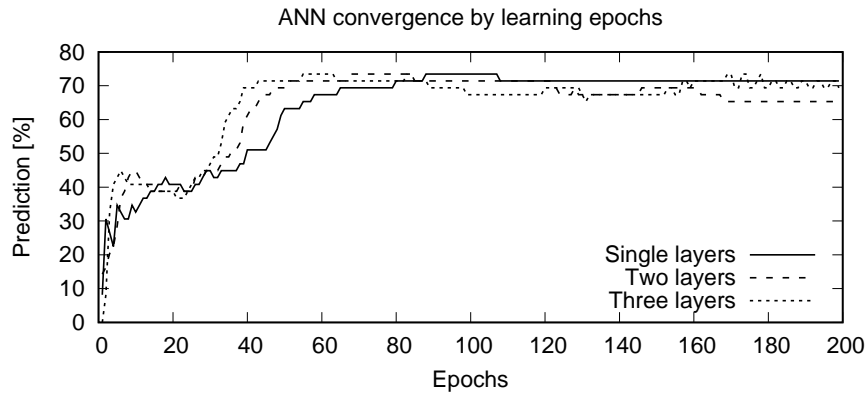


Figure 5. Convergence of ANN of perceptron, feed forward and deep feed forward, on analyzed dataset.

tasks. It is to expect that there are better ANN topologies for such a task, and this is a field for further investigation.

From the above it is obvious that even in its crudest form artificial neural networks are capable to successfully deal with the spectra classification. It is confirmed that this case could be used as a figure of merit for the further development of ANN and machine learning applications in general.

4. Conclusions and future possibilities

The results are promising and the further research on the field is expected. The first goal of analysis of a single set of complex spectral data recorded under similar conditions is achieved with reasonably good prediction. Concerning minute differences in comparison to each other it is considerable result for the basic ANN structure.

Since the quality of the trained artificial neural network prediction is related to its structure as well as the dataset quality and volume, an effort on a large-scale database collection should be carried out. One of the first steps should be inclusion of pre-trained convolutional ANN for the purpose of input data pre-processing before entering of selector ANN.

Commercial packages as well as some specific open-source solutions for the analysis of the spectra with the help of predefined ANN exist. Their application is usually very specific and does not allow the opportunity to fit the best ANN nor to perform unique mathematical procedures during input data preparation that could be best suited for the sought purpose. This possibility is the winning factor in each specific case. Such approach should enable systems for more specialized problem solutions, from stellar and fusion spectra analysis up to more

specific expert systems related to technical solutions. The further development in both ANN structures as well as data preparation should be carried out with the specified problem in mind.

Acknowledgements. The research was funded by the Ministry of Education, Science and Technological Development of the Republic of Serbia, Contract: 451-03-68/2022-14/200024 and supported by the Science Fund of the Republic Serbia, Grant no. 3108/2021.

References

- Albert, D., Antony, B. K., Ba, Y. A., et al., A Decade with VAMDC: Results and Ambitions. 2020, *Atoms*, **8**, 76, DOI: 10.3390/atoms8040076
- Baron, D., Machine Learning in Astronomy: a practical overview. 2019, *arXiv e-prints*, arXiv:1904.07248
- Basile, T., Marsico, A. D., & Perniola, R., Use of Artificial Neural Networks and NIR Spectroscopy for Non-Destructive Grape Texture Prediction. 2022, *Foods*, **11**, DOI: 10.3390/foods11030281
- Bornstein, B., Castano, R., Gilmore, M., Merrill, M., & Greenwood, J., Creation and testing of an artificial neural network based carbonate detector for Mars rovers. 2005, in *2005 IEEE Aerospace Conference*, 378–384
- Castorena, J., Oyen, D., Ollila, A., Legett, C., & Lanza, N., Deep spectral CNN for laser induced breakdown spectroscopy. 2021, *Spectrochimica Acta Part B: Atomic Spectroscopy*, **178**, 106125, DOI: <https://doi.org/10.1016/j.sab.2021.106125>
- D’Isanto, A., Cavuoti, S., Brescia, M., et al., An analysis of feature relevance in the classification of astronomical transients with machine learning methods. 2016, *Monthly Notices of the RAS*, **457**, 3119, DOI: 10.1093/mnras/stw157
- Hampton, E. J., Medling, A. M., Groves, B., et al., Using an artificial neural network to classify multicomponent emission lines with integral field spectroscopy from SAMI and S7. 2017, *Monthly Notices of the Royal Astronomical Society*, **470**, 3395, DOI: 10.1093/mnras/stx1413
- Kates-Harbeck, J., Svyatkovskiy, A., & Tang, W., Predicting disruptive instabilities in controlled fusion plasmas through deep learning. 2019, *Nature*, **568**, 526, DOI: 10.1038/s41586-019-1116-4
- Koujelev, A., Sabsabi, M., Motto-Ros, V., Laville, S., & Lui, S., Laser-induced breakdown spectroscopy with artificial neural network processing for material identification. 2010, *Planetary and Space Science*, **58**, 682, DOI: <https://doi.org/10.1016/j.pss.2009.06.022>, exploring other worlds by exploring our own: The role of terrestrial analogue studies in planetary exploration
- Li, Z., Zhang, X., Mohua, G. A., & Karanassios, V., Artificial Neural Networks (ANNs) for Spectral Interference Correction Using a Large-Size Spectrometer and ANN-Based Deep Learning for a Miniature One. 2017, in *Advanced Applications for Artificial Neural Networks*, ed. A. El-Shahat (Rijeka: IntechOpen)

- Longin, L., Tusek, A. J., Valinger, D., et al., Application of Artificial Neural Networks (ANN) Coupled with Near-InfraRed (NIR) Spectroscopy for Detection of Adulteration in Honey. 2019, *Biodiversity Information Science and Standards*, **3**, e38048, DOI: 10.3897/biss.3.38048
- Marinković, B., Srećković, V., Vujčić, V., et al., BEAMDB and MOLD—Databases at the Serbian Virtual Observatory for Collisional and Radiative Processes. 2019, *Atoms*, **7**, 11, DOI: 10.3390/atoms7010011
- McCulloch, W. S. & Pitts, W., A logical calculus of the ideas immanent in nervous activity. 1943, *The bulletin of mathematical biophysics*, **5**, 115, DOI: 10.1007/BF02478259
- Pickles, A. J., A Stellar Spectral Flux Library: 1150-25000 Å. 1998, *Publications of the ASP*, **110**, 863, DOI: 10.1086/316197
- Rosenblatt, F., The perceptron: A probabilistic model for information storage and organization in the brain. 1958, *Psychological Review*, **65**, 386, DOI: 10.1037/h0042519
- Wang, Q., Zheng, N., Li, Z., & Ma, Z., Quantitative analysis of glucose in whole blood using FT-Raman spectroscopy and artificial neural network. 2015, in *Proceedings of the 2015 International Conference on Computational Science and Engineering* (Atlantis Press), 471–475

Monitoring solar activity during 23/24 solar cycle minimum through VLF radio signals

A. Kolarski, V.A. Srećković^{ib} and Z.R. Mijić^{ib}

Institute of Physics Belgrade, University of Belgrade, Pregrevica 118, 11080 Belgrade, Serbia (E-mail: aleksandra.kolarski@ipb.ac.rs)

Received: July 20, 2022; Accepted: October 2, 2022

Abstract. Solar activity during solar minimum between 23rd and 24th solar cycle was inspected, based on solar X-ray radiation listings from Geostationary Operational Environmental Satellite (GOES) database. Periods of quiet solar conditions with low background X radiation are particularly favourable for analysis and exploration of low intensity solar flare events and their effects on lower ionosphere. Low intensity solar flare events were monitored and examined through Very Low Frequency (VLF) radio signals (3-30 kHz), recorded by the use of Absolute Phase and Amplitude Logger system (AbsPAL) operating at the Institute of Physics Belgrade, Serbia. For the purposes of numerical modeling of low ionospheric response to low class solar flare events, the Long Wave Propagation Capability (LWPC) software, based on Wait's theory, was applied. Main results are presented in this paper.

Key words: Solar activity – Solar X-ray flares – radio signal perturbations

1. Introduction

During quiet solar conditions, ionization i.e. production of electron content within lower ionospheric D-region, within altitude range 50-90 km, is in general related to photoionization processes caused by UV Lyman- α spectral line 121.6 nm, EUV spectral lines ranging from 102.7 nm to 118.8 nm and galactic cosmic rays. One of frequent extraterrestrial causing agents, that become major source of electron density perturbations within D-region, are X-ray solar flare events (0.1-0.8 nm) (Whitten & Poppoff, 1965; Wang et al., 2020; Hayes et al., 2021). Due to additional ionization, electron density height profile of the lower ionosphere changes (Mitra, 1974). Such perturbations affect propagation of Very Low Frequency (VLF) radio signals within Earth-ionosphere waveguide, causing deviations from their regular propagation patterns stable at unperturbed solar conditions (Thomson, 1993; McRae & Thomson, 2000). Since electron production rate coefficients can be considered directly proportional to intensity of incident X-radiation (Ratcliffe et al., 1972), perturbations of VLF radio signals induced by solar flares can be used as diagnostic tool for exploration of lower ionospheric electron content behavior during such events (see Barta et al., 2022, and references therein).

Utilization of VLF radio signals, as the remotesensing technique for exploration of the lower ionosphere (Thomson et al., 2011; McRae & Thomson, 2000; McRae & Thomson, 2004; Thomson et al., 2005), is widely adopted and extensively used by many research groups over several decades, e.g. (Silber & Price, 2017) and references therein. Response of the lower ionosphere to analyzed solar flare events, numerically was modeled by the use of Long Wave Propagation Capability (LWPC) (Ferguson, 1998) software relying on application of Wait's theory (Wait & Spies, 1964).

Effects of low intensity solar flare events of C and B classes, during 23/24 solar minimum, between descending branch of 23rd and ascending branch of 24th solar cycle, were inspected by monitoring recordings of VLF radio signals recorded in Belgrade (44.85 N, 20.38 W) Serbia, within time period from 2008 to 2010. Data related to solar X-rays is obtained from Geostationary Operational Environmental Satellite (GOES) archive database (<https://satdat.ngdc.noaa.gov/sem/goes/data/avg/>).

2. Observations

Periods of quiet solar activity, like during solar minimums, are of great interest for studying quiet ionospheric conditions and accompanying quiet i.e. unperturbed states within Earth-ionosphere waveguide related to VLF radio signals' transmission. In addition, since solar background X radiation during such periods is of small amount, low class solar flare events, like those of lower C class and moderate B class, when occur, are easily noticeable and recognizable, clearly distinguishing themselves from surrounding sections of unperturbed VLF radio signals. This gives a unique opportunity to examine characteristics of low class solar flare events, which are otherwise masked by high solar background X radiation during periods of usual more intense solar activity. An example of active Sun during solar maximum in April 2014 and quiet Sun during solar minimum in December 2019 are given in Figure 1, left and right, respectively. In 23/24 solar minimum, during 2008 there were 8 C class and 1 M class solar flare events reported, with X-ray background flux up to A8.1, while during 2009 there were 28 C class solar flare events reported, with X-ray background flux up to B1.4 (Figure 2).

VLF radio signal recordings obtained from the Absolute Phase and Amplitude Logger receiving station (AbsPAL), located and operating at the Institute of Physics in Belgrade, Serbia, was used as instrumental setup. Within inspected time period from 2008 to 2010, several VLF radio signals were simultaneously recorded by AbsPAL station in Belgrade. Geographical position and transmitter's characteristics of VLF radio signals propagating towards Belgrade are given in Table 1.

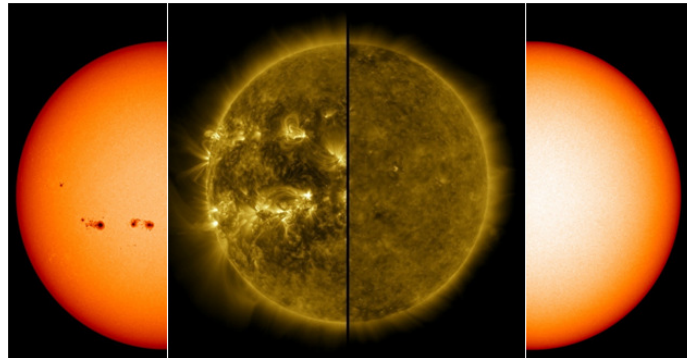


Figure 1. Active Sun during solar max. in April 2014 (left) and quiet Sun during solar min. in December 2019 (right) (taken from <https://www.nasa.gov/>).

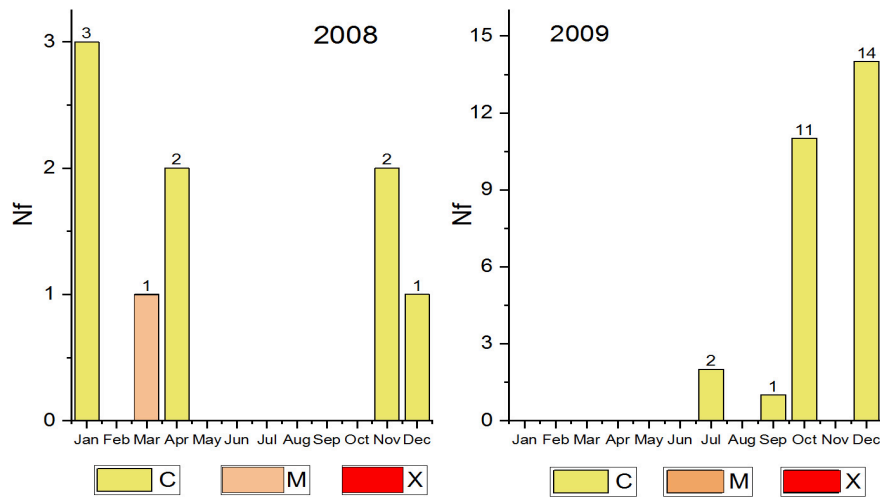


Figure 2. Solar flare events reported in period 2008-2010.

3. Results and discussion

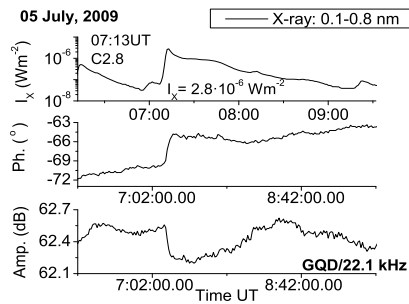
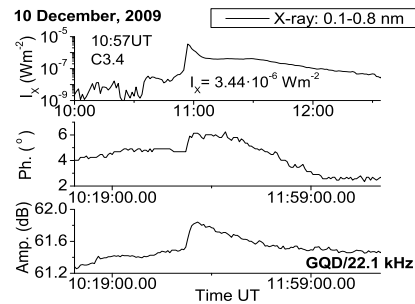
Inspection of low intensity solar flare events of C and B class, on recorded VLF radio signals, was done according to provided solar X radiation listings from GOES database. During inspected period 2008-2010, low class solar flare events exhibited expected behavior, with amplitude perturbations of absolute amount in general of several tenth parts of dB up to few dB and with phase delay perturbations of absolute amount of few degrees to up to 16° . Some typical

Table 1. VLF radio signals registered in Belgrade during 23/24 solar cycle minimum.

VLF signal (kHz)	Transmitter	Broadcast Power (kW)	GCP* Distance (km)
GQD/22.1	Skelton, UK (54.72N; 2.88W)	500	1982
NAA/24.0	Maine, USA (44.63N; 67.28W)	1000	6547
NWC/19.8	H. E. Holt, Australia (27.2S; 114.98E)	1000	11975
DHO/23.4	Rhauderfehn, Germany (53.08N; 7.62E)	800	1301
ICV/20.27	Isola di Tavolara, Italy (NATO) (40.92N; 9.73E)	20	970
HWU/18.3	Rosnay, France (NATO) (46.71N; 1.24E)	400	1493

*Great Circle Path (GCP)

examples of low intensity solar flare events and accompanied VLF radio signal perturbations registered in Belgrade are given in Figures 3-4. However, in some cases, relatively weak solar flare events induced amplitude perturbations of as much as 5 dB and 13° , while from relatively stronger ones, perturbations reached as much as 5 dB and 15° (Figures 5-8). Particularly interesting case was solar flare event of B class B8.35 which induced amplitude perturbation in NAA/24.0 kHz radio signal of 1.5 dB and phase delay perturbation of 10° (Figures 9-10, rounded by oval and enlarged in Figures 11-12).

**Figure 3.** GQD signal perturbation during C2.8 class X-ray solar flare event.**Figure 4.** GQD signal perturbation during C3.4 class X-ray solar flare event.

Electron density height profile within Earth's lower ionosphere changes due to the incident solar X-ray radiation during solar flare events, causing in general descending and "sharpening" of the ionospheric lower boundary. Model of VLF radio signals propagation within Earth-ionosphere waveguide (Wait & Spies, 1964), that describes the electron density by reflecting edge sharpness,

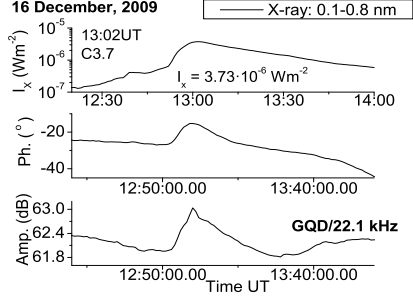


Figure 5. GQD signal perturbation during C3.7 class X-ray solar flare event.

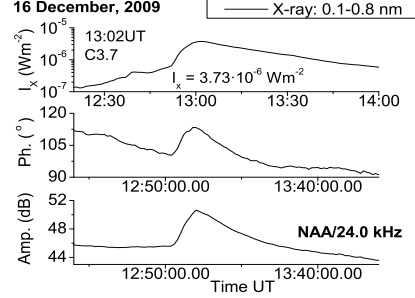


Figure 6. NAA signal perturbation during C3.7 class X-ray solar flare event.

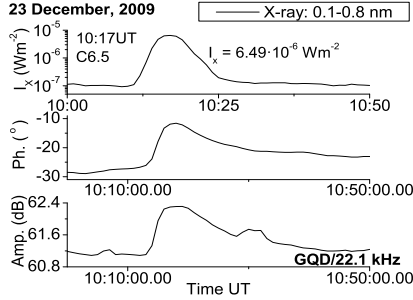


Figure 7. GQD signal perturbation during C6.5 class X-ray solar flare event.

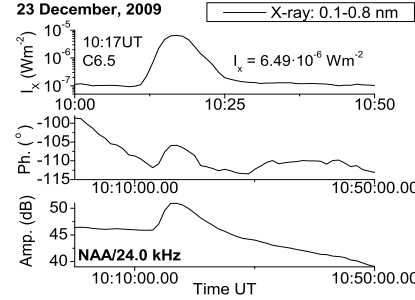


Figure 8. NAA signal perturbation during C6.5 class X-ray solar flare event.

denoted by β (km^{-1}) and reflecting edge height, denoted by H' (km), was used for purposes of numerical simulations of VLF radio signal propagation through Earth-ionosphere waveguide. Obtained results through simulations are in good agreement with VLF signal amplitude and phase delay data measured in Belgrade. Electron density height profiles $N_e(z)$, within altitude range 50-90 km, were obtained through the equation (Wait & Spies, 1964):

$$N_e(z, H', \beta) = 1.43 \cdot 10^{13} e^{-0.15H'} e^{(\beta-0.15)(z-H')} . \quad (1)$$

Numerical simulations were conducted for the entire time evolution of chosen solar flare events, with parameter pairs (β/H') held constant along VLF radio signal's GCPs, depicting "average" ionospheric conditions within waveguide. VLF radio signal's amplitude and phase delay perturbations ΔA (dB) and ΔP ($^\circ$), were determined by comparing measured perturbed to the measured

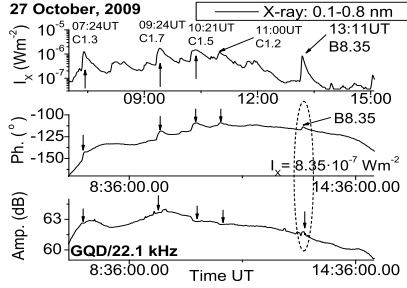


Figure 9. GQD signal perturbations during October 27th, 2009.

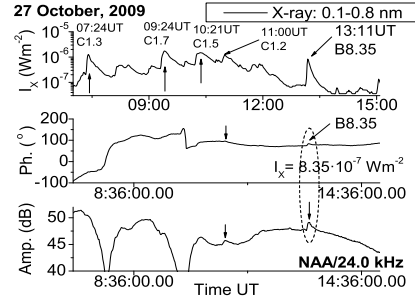


Figure 10. NAA signal perturbations during October 27th, 2009.

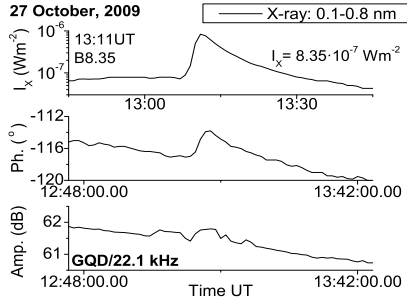


Figure 11. GQD signal perturbation during B8.35 class X-ray solar flare event.

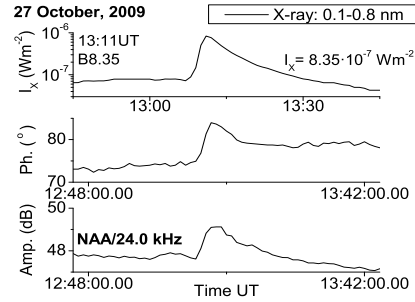


Figure 12. NAA signal perturbation during B8.35 class X-ray solar flare event.

unperturbed amplitude and phase delay values and are calculated as: $\Delta A = A_{flare} - A_{unpert}$ and $\Delta P = P_{flare} - P_{unpert}$. During simulations through iterative process, the goal was to achieve as close as possible to measured data, both absolute values of simulated amplitude and phase delay and relative amount of perturbations. Results obtained through numerical simulations are in good agreements with measured data. Calculated electron density height profiles during maximum of X-ray solar irradiance, in case of NAA/24.0 kHz signal trace, are given in (Figure 13), for some chosen examples of solar flare events: a) low intensity C class solar flare event C3.7 that occurred on December 16th, 2009, at 13:02UT with $I_{max} = 3.73 \cdot 10^{-6} \text{ Wm}^{-2}$, with measured $\Delta A_{flare} = 5 \text{ dB}$ and $\Delta P_{flare} = 13^\circ$ and through simulations obtained parameter pair (β/H') (0.43 $\text{km}^{-1}/69.7 \text{ km}$) with calculated electron density $N_e(74 \text{ km}) = 1.37 \cdot 10^9 \text{ m}^{-3}$, b) moderate intensity C class solar flare event C6.5 that occurred on December

23rd, 2009, at 10:17UT with $I_{max} = 6.49 \cdot 10^{-6} \text{ Wm}^{-2}$ with measured $\Delta A_{flare}=5$ dB and $\Delta P_{flare}=6^\circ$ and through simulations obtained parameter pair (β/H') ($0.43 \text{ km}^{-1}/70.1 \text{ km}$) with calculated electron density $N_e(74 \text{ km})=1.17 \cdot 10^9 \text{ m}^{-3}$ and c) moderate intensity B class solar flare event B8.35 that occurred on October 27th, 2009, at 13:11UT with $I_{max} = 8.35 \cdot 10^{-7} \text{ Wm}^{-2}$ with measured $\Delta A_{flare}=1.5$ dB and $\Delta P_{flare}=10^\circ$ and through simulations obtained parameter pair (β/H') ($0.33 \text{ km}^{-1}/72.3 \text{ km}$) with calculated electron density $N_e(74 \text{ km})=3.79 \cdot 10^8 \text{ m}^{-3}$. Obtained electron density height profiles in flare state, with $N_e(74 \text{ km})$ increase of about one order of magnitude in case of C class flares, with slight increase of about 75% in case of B class flare, are realistic and in line with other studies (Žigman et al., 2007; Grubor et al., 2008; McRae & Thomson, 2004; Kolarski et al., 2011; Nina et al., 2011, 2012; Kolarski & Grubor, 2014; Kolarski et al., 2022; Srećković et al., 2021a,b).

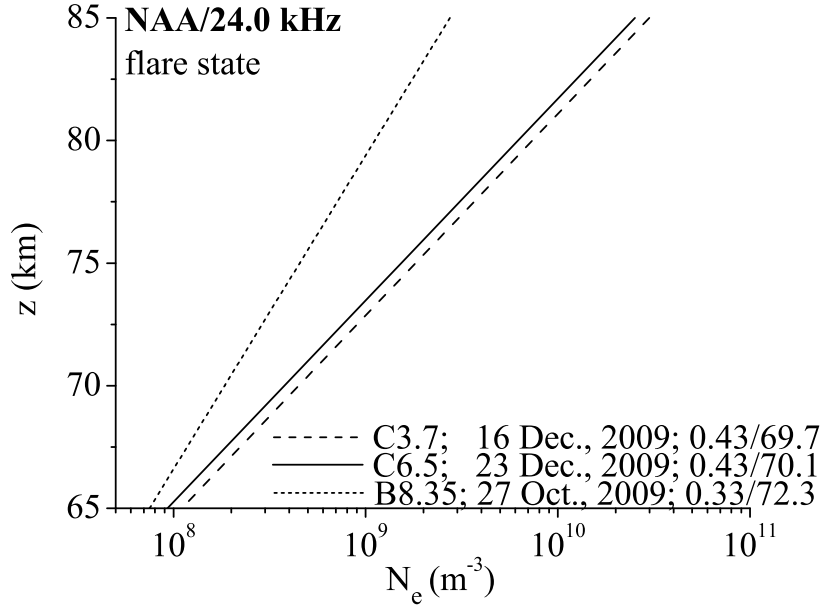


Figure 13. Electron density height profiles during C3.7 (dashed line), C6.5 (solid line) and B8.35 (dotted line) class X-ray solar flare events.

It is possible to draw conclusions about the intensity of the causing X-ray solar flare events, based upon perturbation amounts obtained from VLF radio signal recordings, when taking into consideration single VLF radio signal trace.

However, same solar flare event can produce perturbations different both in pattern and in intensity, when observed on different VLF radio signal traces. Typical examples are in general perturbations induced by solar flare events of moderate and lower intensity classes as recorded in Belgrade during active solar periods on NAA and GQD radio signals. In such cases, NAA signal's both amplitude and phase delay follow in pattern incident X-ray solar irradiance, while in case of GQD signal, amplitude and phase delay follow incident X-ray solar irradiance in pattern, but like mirrored images and only in some cases of higher class solar flare events this feature is more or less mitigated (Žigman et al., 2007; Grubor et al., 2008; Kolarski & Grubor, 2014). Aside to main factor of solar flare intensity (Grubor et al., 2008; Kolarski & Grubor, 2014), this behavior is also strongly under the influence of VLF GCP trace characteristics (Kolarski & Grubor, 2015; Šulić & Srećković, 2014; Šulić et al., 2016). For example, measured absolute perturbation as observed on GQD radio signal trace, in case of C3.7 solar flare event was $\Delta A_{flare}=1$ dB and $\Delta P_{flare}=11.5^\circ$, in case of C6.5 solar flare event was $\Delta A_{flare}=1.2$ dB and $\Delta P_{flare}=15.5^\circ$ and in case of B8.35 solar flare event it was $\Delta A_{flare}=0.4$ dB and $\Delta P_{flare}=3.3^\circ$.

4. Summary

Two year time period of VLF radio signal recordings from Belgrade AbsPAL database, corresponding to 23/24 solar minimum, was examined in order of getting better insight of effects that low intensity solar flare events of C and B classes have on the lower ionospheric region and transmission of VLF radio signals within Earth-ionosphere waveguide. According to GOES database, during inspected period 2008-2010, 38 solar flare events of C and M class were reported, with X-ray background flux in range up to A8.1 for 2008 and B1.4 for 2009. Low intensity solar flare events of C and B class were monitored on all recorded VLF radio signals. Depending on solar flare occurrence time and VLF radio signal's GCP towards Belgrade receiver station, some flares were simultaneously observed on several VLF radio signals, however, detailed analysis in this paper was conducted for cases of NAA/24.0 kHz and GQD/22.1 kHz signal traces.

As expected, majority of low class solar flare events in general revealed perturbations of absolute amount of several tenth parts of dB up to few dB and of few degrees to up to 16° , following the manner of incident solar X-ray flux. However, there were also cases that fall out of the pattern, when relatively weak solar flare events such as C3.7, produced perturbations of 5 dB and 13° , while relatively stronger ones, such C6.5 gave perturbations of similar amount, as 5 dB and 15° . Due to low X-ray background flux, in some cases even B class solar flare events induced noticeable perturbations, as in case of B8.35 with perturbation of 1.5 dB and 10° .

Numerical simulations were conducted using LWPC software package, with goal of achieving simulated VLF data as close as possible to measured VLF data in Belgrade, both in case of absolute values and in case of relative amount of perturbations. Results obtained through iterative numerical simulations are in good agreements with real VLF data measured in Belgrade (Žigman et al., 2007; Grubor et al., 2008; Kolarski et al., 2011; Nina et al., 2011). In case of NAA/24.0 kHz signal, perturbations induced by low class solar flare events produced "sharpening" and descending of the lower ionospheric boundary, as in cases of presented solar flare events reflection height went from unperturbed value of 74 km to 72.3, 70.1 and 69.7 km, while become "sharper" compared to unperturbed value of 0.3 km^{-1} reaching 0.33 and 0.44 km^{-1} . Estimated N_e (74 km) are realistic and in line with other studies (McRae & Thomson, 2004; Nina et al., 2012; Kolarski & Grubor, 2014; Kolarski et al., 2022; Srećković et al., 2021a,b).

Acknowledgements. Authors thank D. Šulić for instrumental setup. This work was funded by the Institute of Physics Belgrade through a grant by the Ministry of Education, Science, and Technological Development of the Republic of Serbia. Authors appreciate comments expressed by referees, which improved this paper.

References

- Barta, V., Natras, R., Srekovi, V., et al., Multi-instrumental investigation of the solar flares impact on the ionosphere on 0506 December 2006. 2022, *Frontiers in Environmental Science*, **10**, DOI: 10.3389/fenvs.2022.904335
- Ferguson, J. 1998, Computer programs for assessment of long-wavelength radio communications, version 2.0: User's guide and source files, Tech. rep., Space and naval warfare systems center San Diego CA
- Grubor, D., Šulić, D., & Žigman, V., Classification of X-ray solar flares regarding their effects on the lower ionosphere electron density profile. 2008, *Annales Geophysicae*, **26**, 1731, DOI: 10.5194/angeo-26-1731-2008
- Hayes, L. A., O'Hara, O. S. D., Murray, S. A., & Gallagher, P. T., Solar Flare Effects on the Earth's Lower Ionosphere. 2021, *Solar Physics*, **296**, 157, DOI: 10.1007/s11207-021-01898-y
- Kolarski, A. & Grubor, D., Sensing the Earths low ionosphere during solar flares using VLF signals and goes solar X-ray data. 2014, *Advances in space research*, **53**, 1595, DOI: 10.1016/j.asr.2014.02.022
- Kolarski, A. & Grubor, D., Comparative analysis of VLF signal variation along trajectory induced by X-ray solar flares. 2015, *Journal of Astrophysics and Astronomy*, **36**, 565, DOI: 10.1007/s12036-015-9361-x
- Kolarski, A., Grubor, D., & Šulić, D., Diagnostics of the Solar X-Flare Impact on Lower Ionosphere through the VLF-NAA Signal Recordings. 2011, *Open Astronomy*, **20**, 591, DOI: 10.1515/astro-2017-0342

- Kolarski, A., Srećković, V. A., & Mijić, Z. R., Response of the Earths Lower Ionosphere to Solar Flares and Lightning-Induced Electron Precipitation Events by Analysis of VLF Signals: Similarities and Differences. 2022, *Applied Sciences*, **12**, 582, DOI: 10.3390/app12020582
- McRae, W. M. & Thomson, N. R., VLF phase and amplitude: Daytime ionospheric parameters. 2000, *Journal of Atmospheric and Solar-Terrestrial Physics*, **62**, 609, DOI: 10.1016/S1364-6826(00)00027-4
- McRae, W. M. & Thomson, N. R., Solar flare induced ionospheric D-region enhancements from VLF phase and amplitude observations. 2004, *Journal of Atmospheric and Solar-Terrestrial Physics*, **66**, 77, DOI: 10.1016/j.jastp.2003.09.009
- Mitra, A. P. 1974, *Ionospheric effects of solar flares* (Springer, Berlin/Heidelberg)
- Nina, A., Čadež, V., Srećković, V., & Šulić, D., The influence of solar spectral lines on electron concentration in terrestrial ionosphere. 2011, *Open Astronomy*, **20**, 609, DOI: 10.1515/astro-2017-0346
- Nina, A., Čadež, V., Srećković, V., & Šulić, D., Altitude distribution of electron concentration in ionospheric D-region in presence of time-varying solar radiation flux. 2012, *Nuclear Instruments and Methods in Physics Research Section B: Beam Interactions with Materials and Atoms*, **279**, 110, DOI: 10.1016/j.nimb.2011.10.019
- Ratcliffe, J. A. et al. 1972, *An introduction to ionosphere and magnetosphere* (CUP Archive, Cambridge, UK)
- Silber, I. & Price, C., On the use of VLF narrowband measurements to study the lower ionosphere and the mesosphere–lower thermosphere. 2017, *Surveys in Geophysics*, **38**, 407, DOI: 10.1007/s10712-016-9396-9
- Srećković, V. A., Šulić, D. M., Ignjatović, L., & Vujčić, V., Low Ionosphere under Influence of Strong Solar Radiation: Diagnostics and Modeling. 2021a, *Applied Sciences*, **11**, 7194, DOI: 10.3390/app11167194
- Srećković, V. A., Šulić, D. M., Vujčić, V., Mijić, Z. R., & Ignjatović, L. M., Novel Modelling Approach for Obtaining the Parameters of Low Ionosphere under Extreme Radiation in X-Spectral Range. 2021b, *Applied Sciences*, **11**, 11574, DOI: 10.3390/app112311574
- Thomson, N., Experimental daytime VLF ionospheric parameters. 1993, *Journal of Atmospheric and Terrestrial Physics*, **55**, 173, DOI: 10.1016/0021-9169(93)90122-F
- Thomson, N. R., Rodger, C. J., & Clilverd, M. A., Large solar flares and their ionospheric D region enhancements. 2005, *Journal of Geophysical Research: Space Physics*, **110**, DOI: <https://doi.org/10.1029/2005JA011008>
- Thomson, N. R., Rodger, C. J., & Clilverd, M. A., Daytime D region parameters from long-path VLF phase and amplitude. 2011, *Journal of Geophysical Research: Space Physics*, **116**, DOI: <https://doi.org/10.1029/2011JA016910>
- Šulić, D. M. & Srećković, V. A., A Comparative Study of Measured Amplitude and Phase Perturbations of VLF and LF Radio Signals Induced by Solar Flares. 2014, *Serbian Astronomical Journal*, **188**, 45, DOI: 10.2298/SAJ1488045S

- Šulić, D. M., Srećković, V. A., & Mihajlov, A. A., A study of VLF signals variations associated with the changes of ionization level in the D-region in consequence of solar conditions. 2016, *Advances in Space Research*, **57**, 1029, DOI: 10.1016/j.asr.2015.12.025
- Wait, J. R. & Spies, K. P. 1964, *Characteristics of the Earth-ionosphere waveguide for VLF radio waves* (US Department of Commerce, National Bureau of Standards, Boulder, CO, USA)
- Wang, X., Chen, Y., Toth, G., et al., Predicting Solar Flares with Machine Learning: Investigating Solar Cycle Dependence. 2020, *Astrophysical Journal*, **895**, 3, DOI: 10.3847/1538-4357/ab89ac
- Whitten, R. & Poppoff, I. 1965, *Physics of the Lower Ionosphere* (Prentice-Hall, Englewood Cliffs, N. J.)
- Žigman, V., Grubor, D., & Šulić, D., D-region electron density evaluated from VLF amplitude time delay during X-ray solar flares. 2007, *Journal of atmospheric and solar-terrestrial physics*, **69**, 775, DOI: 10.1016/j.jastp.2007.01.012

Influence of the solar hydrogen Ly α line on the GNSS signal delay in the ionospheric D-region

D. Petković¹, O. Odalović¹ and A. Nina²

¹ Faculty of Civil Engineering, University of Belgrade, Bulevar kralja Aleksandra 73, 11000 Belgrade, Serbia

² Institute of Physics Belgrade, University of Belgrade, Pregrevica 118, 11080 Belgrade, Serbia (E-mail: sandrast@ipb.ac.rs)

Received: July 20, 2022; Accepted: October 2, 2022

Abstract. Recent research indicates that the influence of the ionospheric D-region on the propagation of satellite signals cannot be ignored during the intense X-radiation emitted during solar X-ray flares. In this paper, we investigate the influence of changes in the solar hydrogen Ly α radiation, which is manifested in variations of the D-region electron density and, consequently, the total electron content in this region, on the propagation of the Global Navigation Satellite System (GNSS) signals. We consider changes during a solar cycle and year, represented by the smoothed daily sunspot number and the day of year. The obtained results indicate that the influence of the D-region on these signals is not negligible for positioning with a single signal recorded by a single receiver during the period around the maximum of a solar cycle.

Key words: solar hydrogen Ly α radiation – total electron content – ionosphere – GNSS signal delay

1. Introduction

The terrestrial atmosphere is constantly exposed to the influence of solar radiation, which significantly affects the characteristics of its upper part. The consequence of that influence is the formation of the ionized layer called the ionosphere (50 km - 1000 km) in which ionization processes occur in collisions of atmospheric particles with different kinds of particles and photons. Photo-ionization processes depend on the incident photons wavelengths and the considered location. Namely, solar photons in the upper ionosphere, which play a dominant role in photo-ionization processes in these altitude domain, have wavelengths in the soft X-domain of the electromagnetic spectrum, while, during quiet solar conditions, the solar hydrogen Ly α photons are the most significant source of these processes in the lowest ionospheric layer called the D-region.

Free electrons produced in the photo-ionization processes play a significant role in the propagation of electromagnetic waves, including the satellite signals emitted by the Global Navigation Satellite System (GNSS). This system refers

to any constellation of satellites used to provide accurate and three-dimensional positioning and navigation on a global or regional scale. The United States Department of Defense has been established NAVSTAR GPS (Global Positioning System) as the very first system of its kind. Following that lead, five other positioning systems were built during the last two decades, including Russia's Global Navigation Satellite System (GLONASS), China's BeiDou (or COMPASS), the Navigation with Indian Constellation (NavIC) (or the Indian Regional Navigation Satellite System (IRNSS)), Japanese Quasi-Zenith Satellite System (QZSS), and the European Union's GALILEO (Hofmann-Wellenhof et al., 2008).

GNSS signals play a very important role in modern life, which is why the study of the ionospheric electron density changes also has practical applications. The influence of the atmosphere on their propagation is significant in the ionosphere and troposphere. At the same time, the ionospheric effect on signal propagation is more important in the upper ionosphere due to a significantly higher electron density than at its lower altitudes. However, recent research indicates that the influence of the perturbed D-region cannot be ignored (Nina et al., 2020). Bearing in mind that even in the absence of sudden disturbances, the characteristics of this ionospheric layer change significantly due to changes in the intensity of incoming Ly α radiation during a solar cycle, year and time of day, the question arises as to how these changes affect the propagation of a GNSS signal. The aim of this paper is to investigate the influence of changes in Ly α radiation during a solar cycle on the delay of the GNSS signal during a year. In this study, we analyse the maximum daily influence of the D-region on the signals, which occurs at noon. This analysis is based on Wait's model of the ionosphere (Wait & Spies, 1964), which describes the ionosphere with two parameters: the "sharpness", β and the signal reflection height, H' , and on the Quiet Ionospheric D-Region (QIonDR) model (Nina et al., 2021), which provides these parameters at noon of the selected day. According to the QIonDR model, White's parameters are counted as functions of the ordinal number of this day in year (Day of Year, DOY) and the smoothed daily sunspot number, σ , relevant for the considered day.

2. Modelling

The solar ionizing radiation (particles and photons in the soft X and UV domains) produces the free electrons in the ionosphere in sufficient quantities to directly affect the radio waves propagation (from 3 kHz up to 300 GHz). The ionospheric parameter which has a significant role in quantification of the ionosphere's state impact on the electromagnetic wave propagation is the Total Electron Content (TEC). It represents the total number of electrons in a column with a 1 m² cross-section area along the signal path from a transmitter

(satellite) to the receiver. Thus, it can be expressed by the simple line integral (Seeber, 2003; Hofmann-Wellenhof et al., 2008):

$$TEC(t) = \int_S^R N_e dh, \quad (1)$$

in which N_e stands for the electron density, R and S are the upper and lower ionosphere boundary, and h is the altitude. TEC is expressed in the Total Electron Content Units (TECU), which amounts to 10^{16} free electrons per m^2 .

TEC delays signal propagation from satellite to receiver. Relationship between TEC and signal delay (P_{ION}) is defined by following equation (Hofmann-Wellenhof et al., 2008):

$$P_{ION} = \pm \frac{40.3}{f^2} \cdot \int_S^R N_e dh = \pm \frac{40.3}{f^2} \cdot TEC, \quad (2)$$

where f denotes frequency of the considered electromagnetic wave, i.e. the used satellite signal.

In this paper, we focus attention on the D-region influence on the signal propagation. For this reason, we modify Equations (1) and (2) such that they only apply to this ionospheric region. If we slightly modify integration boundaries, by setting the upper and lower bounds of the D region instead, i.e. $S = h_{low} = 60$ km and $R = h_{upp} = 90$ km, Equation (1) can be rewritten as follows:

$$TEC_D(t) = \int_{h_{low}}^{h_{upp}} N_e dh, \quad (3)$$

where index D in TEC_D indicates that the TEC value is for ionospheric D-region. In a manner that is analogous to the example given earlier, we are going to refer to the signal delay in the D-region as P_D :

$$P_D = 40.3 \frac{TEC_D}{f^2}. \quad (4)$$

It is necessary to point out that Equations (1) and (3) represents the TEC calculation for the electromagnetic wave that is coming in from the zenith direction (signal path goes perpendicular to the D-region boundary). In the case that the satellite signal does not arrive from the zenith direction, slant TEC ($STEC$ or $STEC_D$ for D-region only) is introduced. $STEC$ can be calculated using the vertical TEC value and the mapping function $S(\theta)$ corresponding to the actual zenith angle θ :

$$STEC_D(t) = S(\theta) \cdot TEC_D(t) = \frac{TEC_D(t)}{\cos(\theta)}. \quad (5)$$

As can be seen Equation (3), the TEC in both the vertical and slant directions is a function of the electron density N_e . Equation that can be used to calculate the electron density is as follows (Thomson, 1993):

$$N_e(\beta, H', h) = 1.43 \cdot 10^{13} \cdot e^{-\beta \cdot H'} \cdot e^{[\beta - 0.15]h}, \quad (6)$$

where the "sharpness", β , and the signal reflection height, H' , are given in km^{-1} and km , respectively. For quiet solar conditions, these parameters can be determined using the expressions developed in (Nina et al., 2021) for the Central Europe using the Quiet Ionosphere D-region (QIonDR) Model. β can be obtained from:

$$\beta(\sigma, \chi) = 0.2635 + 0.002573 \cdot \sigma - 9.024 \cdot 10^{-6} \cdot \sigma^2 + 0.005351 \cdot \cos(2\pi(\chi - 0.4712)). \quad (7)$$

while H' can be calculated as:

$$H'(\sigma, \chi) = 74.74 - 0.02984 \cdot \sigma + 0.5705 \cdot \cos(2\pi(\chi - 0.4712) + \pi). \quad (8)$$

As one can see in previous expressions, both, β and H' , depend on the two parameters which represent dependency on a solar cycle period, described in terms of the smoothed daily sunspot number, σ , and dependency on the season parameter $\chi = \text{DOY}/365$, where DOY is the day of year (Nina et al., 2021).

The following expression, derived from Equations (3) and (6), can be used to calculate the TEC value in the D-region (Todorović Drakul et al., 2016):

$$TEC_D(t) = 1000 \frac{N_e(\beta, H', h_t) - N_e(\beta, H', h_t)}{\beta(\sigma, \chi) - 0.15}. \quad (9)$$

As one can see, the signal delay, P_D , is a function of the seasonal parameter, χ , smoothed daily sunspot number, σ , zenith angle from which electromagnetic wave reached ionospheric layer, θ , and frequency of the considered signal f . In this study, we analyse the dependencies on χ and σ for the three fixed values of θ , and the two f which are used for satellite signals important for the GNSS positioning.

In addition to analysis of P_D dependencies of the indicated parameters, we also provide analysis of its changes with σ (i.e. changes of derivative $\frac{\Delta P_D}{\Delta \sigma}$) depending on the same parameters.

3. Results and discussion

In this contribution, we calculated signal delay P_D for TEC values as function of DOY and the smoothed daily sunspot number. The values of the zenith angles are chosen to cover the best and worst case scenarios regarding the application of GNSS technology - zenith angle values of $\theta = 0^\circ$ and $\theta = 70^\circ$, as well as

their mean value $\theta = 35^\circ$. Calculations of TEC values are performed to cover all seasons and values of smoothed daily sunspot number σ in the range of 20 to 120. Fig. 1 illustrates vertical TEC values. It shows that TEC reaches its peak during the summer months (summer solstice), and increases with σ .

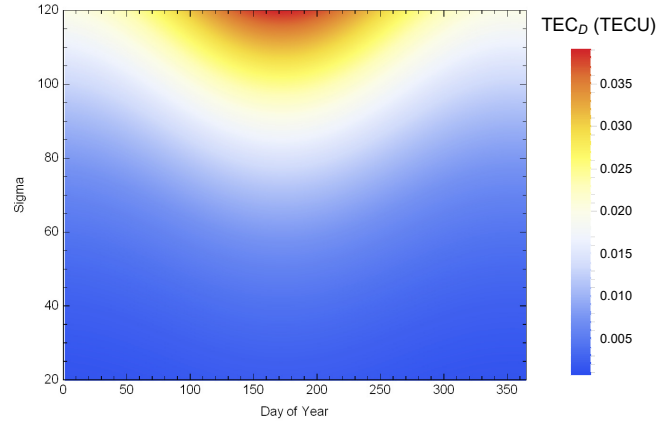


Figure 1. Dependency of vertical TEC_D on the day of year and σ values.

Calculations of the slant TEC are performed based on vertical TEC values and Equation (5). Fig. 2 illustrates those values for zenith angle of $\theta = 35^\circ$ and $\theta = 70^\circ$, respectively. The maximum TEC values for θ values of 0° , 35° , and 70° are respectively 0.04, 0.05, and 0.11 TECU. According to those, we shown that values grow as the zenith angle increases (e.g. as satellite reaches horizon).

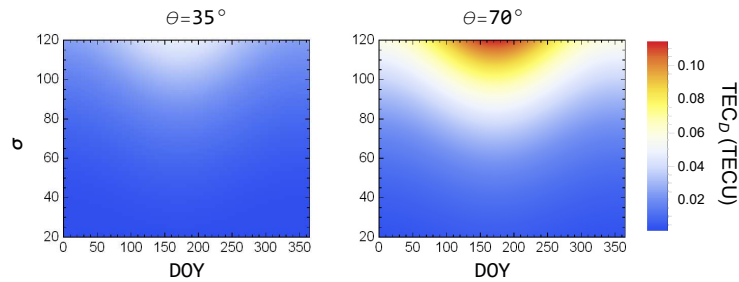


Figure 2. Dependency of the slant TEC_D on the day of year, DOY, and the smoothed daily sunspot number, σ , for the zenith angles $\theta = 35^\circ$ (left) and $\theta = 70^\circ$ (right).

In addition to the TEC values, we analyse the signal delay due to influence of the ionospheric D-region. We consider the frequencies used to broadcast satellite

signals of the satellite systems mentioned in Introduction which are in the range of approximately 1.2 GHz to 1.6 GHz (Hofmann-Wellenhof et al., 2008). In this study we provide calculations for $f_1 = 1.2$ GHz and $f_2 = 1.6$ GHz.

The calculated delays are presented in Fig. 3. In the case of the frequency f_2 , signal delay reached values of 6 mm, 8 mm, and 18 mm for $\theta = 0^\circ$, 35° , and 70° . Within the same spirit, for the frequency f_1 , correspondent delay values are 11mm, 13 mm, and 32 mm. The comparison of the signal delays for the used frequencies are given in the third row of Fig. 3. Analysing this comparison, we can conclude that, even in a relatively small considered frequency range of 0.4 GHz, differences reaches 5 mm, 6 mm, and 14 mm for 0° , 35° , and 70° .

The obtained results indicate that even with the most intense impacts of solar hydrogen Ly α photons on the ionospheric D-region, changes in the propagation of the GNSS signal are significantly smaller than in periods of intense perturbations of this ionospheric layer caused by e.g. solar X-ray flares when P_D can exceed 1 m (Nina et al., 2020). However, for large values of θ parameter, the obtained P_D exceed 1 cm, which represents the minimum value that is included in the total signal delay in Wautelet (2013). For this reason, as well as the fact that the sunspot number can be higher than 120 (the maximum value of σ considered in this analysis), one can conclude that the positioning error that a quiet D-region at solar cycle maxima can cause is not negligible. In other words, variations in the hydrogen Ly α photons that arrive in this layer can provide enough large changes in propagation of a single GNSS signal that using of one GNSS signal and one receiver is not relevant for precise positioning, among others, due to the influence of the quiet D-region during intense radiation from the Sun.

Table 1. The signal delay P_D modelled for Waits parameters presented in Ferguson (1998) (Long Wavelength Propagation Capability (LWPC) numerical model), Bilitza (2018) (International Reference Ionosphere (IRI) model), Thomson et al. (2005), Han et al. (2011), McRae & Thomson (2000) and Thomson et al. (2017) for the signal zenith angle, θ , of 0° , 35° , and 70° , and GNSS signal frequencies, f , of 1.2 GHz and 1.6 GHz.

source of Wait's parameters	P_D ($\theta = 0^\circ$)	P_D ($\theta = 35^\circ$)	P_D ($\theta = 70^\circ$)
		(mm)	
		$f = 1.2/1.6$ GHz	
Ferguson (1998)	0.44/0.25	0.54/0.30	1.29/0.72
Bilitza (2018)	1.59/0.89	1.94/1.09	4.65/2.61
Thomson et al. (2005)	3.77/2.12	4.61/2.59	11.04/6.21
Han et al. (2011)	8.98/5.05	10.97/6.17	26.27/14.78
McRae & Thomson (2000)	4.48/2.52	5.47/3.08	13.11/7.37
Thomson et al. (2017)	1.06/0.59	1.29/0.73	3.09/1.74

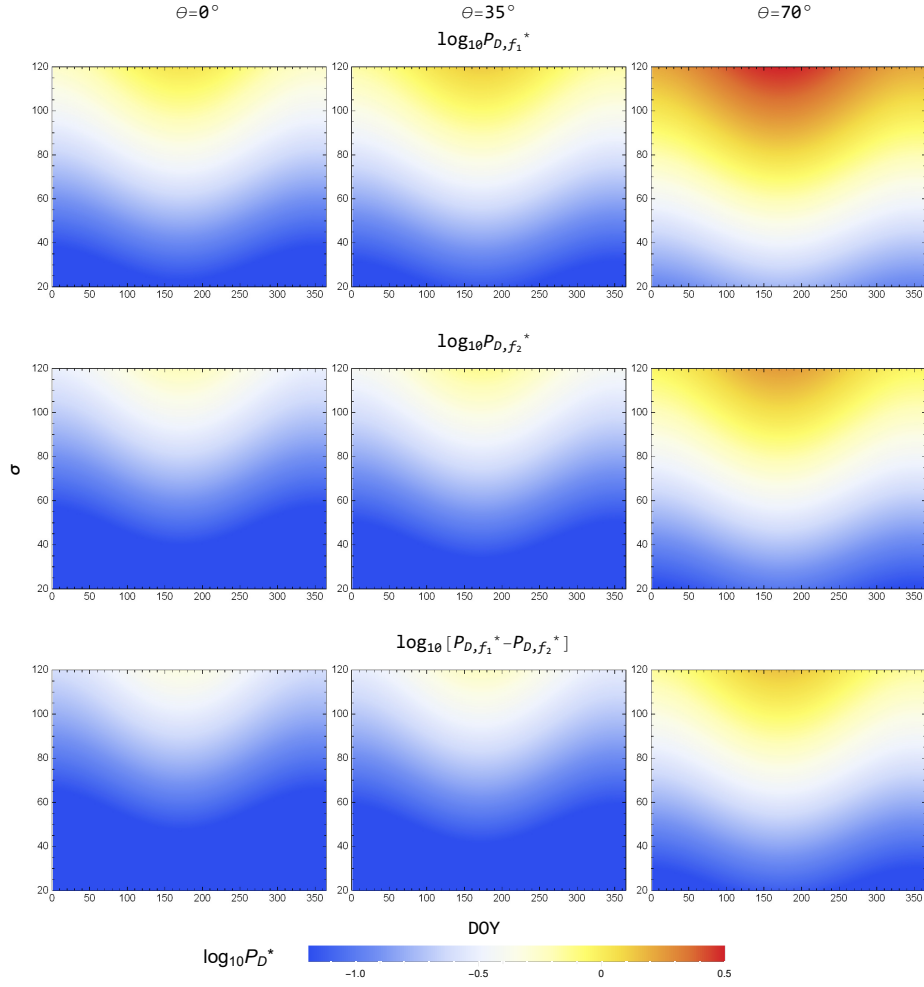


Figure 3. Dependencies of the GNSS signal delay logarithm ($\log_{10}(P_D^*)$) in the ionospheric D-region on the day of year, DOY, and the smoothed daily sunspot number σ . Here, $P_D^* = P_D/1\text{cm}$. The considered zenith angle of the signal are $\theta = 0^\circ$ (first column), $\theta = 35^\circ$ (second column), and $\theta = 70^\circ$ (third column). First two rows represent the signal delay for the specific frequencies $f_1 = 1.2\text{ GHz}$ and $f_2 = 1.6\text{ GHz}$, and the third one represents the difference between those delays.

The obtained values of P_D are in good agreement with those modelled by the presented procedure for the values of Wait's parameters given in [Ferguson \(1998\)](#) (Long Wavelength Propagation Capability (LWPC) numerical model), [Bilitza \(2018\)](#) (International Reference Ionosphere (IRI) model), [Thomson et al.](#)

(2005), Han et al. (2011), McRae & Thomson (2000) and Thomson et al. (2017). Namely, based on the data given in the Tab. 1, it can be seen that all the stated values are within the corresponding ranges obtained in this study.

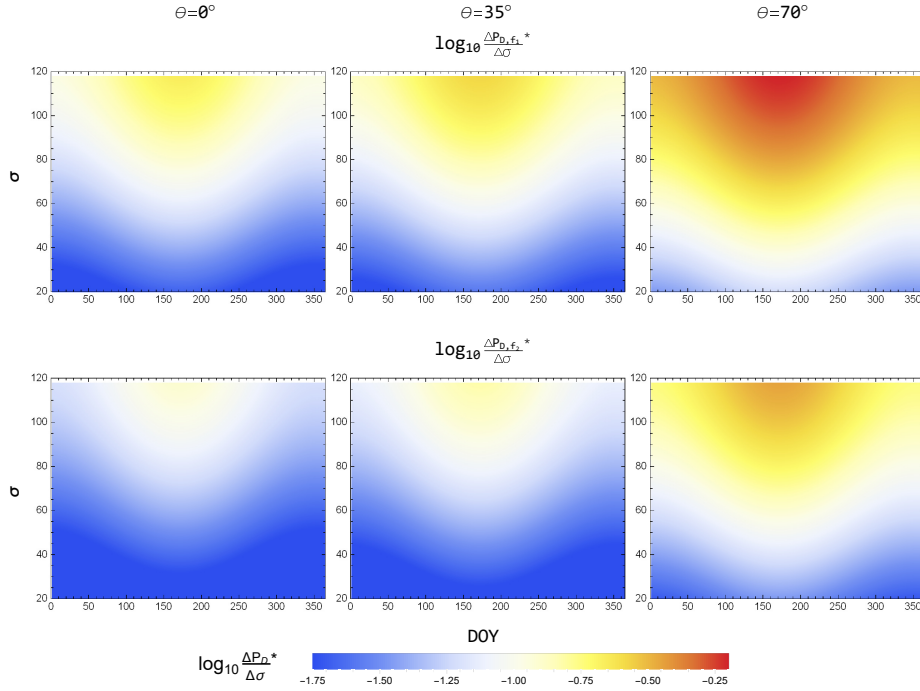


Figure 4. Dependencies of logarithm of the derivative of the GNSS signal delay in the ionospheric D-region with the smoothed daily sunspot number σ ($\log \frac{\Delta P_D^*}{\Delta \sigma}$) on the day of year, DOY, and σ . The considered zenith angle of the signal θ are $\theta = 0^\circ$ (first column), $\theta = 35^\circ$ (second column), and $\theta = 70^\circ$ (third column). The rows represent the considered quantities for the specific frequencies $f_1 = 1.2$ GHz and $f_2 = 1.6$ GHz.

In order to examine the influence of the changes in the solar hydrogen Ly α radiation intensity on changes in P_D , we present an analysis of the dependencies of $\frac{\Delta P_D}{\Delta \sigma}$ on DOY and σ . In Fig. 4, where this dependence is presented for the previously observed values of θ and f , it can be seen that the influence of changes in the sunspot number, i.e. the observed Ly α radiation, on the propagation of the GNSS signal is the greatest during the summer solstice and that it increases with θ . Also, it is important to emphasize that this influence is much more pronounced in the maximum than in the minimum of a solar cycle.

4. Conclusions

In this study, we present a study of the influence of a solar cycle (represented as the smoothed daily sunspot number) and season (represented as the day of year) period, on propagation of the GNSS signals, with the fixed frequency and incident zenith angle, in the ionospheric D-region. We perform the total electron content and signal delay in this ionospheric layer in order to investigate if influence of the quiet D-region can be ignored under all conditions.

The most important conclusion of this study is that variations in the hydrogen Ly α photons arriving in this layer can provide enough large changes in propagation of a single GNSS signal that using of one GNSS signal and one receiver is not relevant for precise positioning.

In addition, the obtained results show the following:

- The total electron content and signal delay increase with the zenith angle and the daily smoothed sunspot number. They are larger in the summer than in the winter months, and reached their maximum values during the summer solstice.
- The obtained signal delays are smaller than in periods of intense perturbations of this ionospheric layer caused by e.g. solar X-ray flares.

Furthermore, various initial conditions affect the ionospheric D-region differently, which consequently affects the propagation of the satellite signals. These influences will be the subject of future research.

Acknowledgements. The authors acknowledge funding provided by the Institute of Physics Belgrade and the Faculty of Civil Engineering, University of Belgrade, through the Ministry of Education, Science, and Technological Development of the Republic of Serbia grants.

References

- Bilitza, D., IRI the International Standard for the Ionosphere. 2018, *Advances in Radio Science*, **16**, 1, DOI: 10.5194/ars-16-1-2018
- Ferguson, J. A. 1998, *Computer Programs for Assessment of Long-Wavelength Radio Communications, Version 2.0*, ed. Space and Naval Warfare Systems Center, San Diego, CA
- Han, F., Cummer, S. A., Li, J., & Lu, G., Daytime ionospheric D region sharpness derived from VLF radio atmospherics. 2011, *Journal of Geophysical Research (Space Physics)*, **116**, 5314, DOI: 10.1029/2010JA016299
- Hofmann-Wellenhof, B., Lichtenegger, H., & Wasle, E. 2008, *GNSS Global Navigation Satellite Systems: GPS, GLONASS, Galileo, and more*, ed. Springer, Vienna, Austria

- McRae, W. M. & Thomson, N. R., VLF phase and amplitude: daytime ionospheric parameters. 2000, *Journal of Atmospheric and Solar-Terrestrial Physics*, **62**, 609, DOI: 10.1016/S1364-6826(00)00027-4
- Nina, A., Nico, G., Mitrović, S., et al., Quiet Ionospheric D-Region (QIonDR) Model Based on VLF/LF Observations. 2021, *Remote Sensing*, **13**, 483, DOI: 10.3390/rs13030483
- Nina, A., Nico, G., Odalović, O., et al., GNSS and SAR Signal Delay in Perturbed Ionospheric D-Region During Solar X-Ray Flares. 2020, *IEEE Geoscience and Remote Sensing Letters*, **17**, 1198, DOI: 10.1109/LGRS.2019.2941643
- Seeber, G. 2003, *Satellite Geodesy*, Walter de Gruyter, Berlin, Germany
- Thomson, N. R., Experimental daytime VLF ionospheric parameters. 1993, *Journal of Atmospheric and Terrestrial Physics*, **55**, 173, DOI: 10.1016/0021-9169(93)90122-F
- Thomson, N. R., Clilverd, M. A., & Rodger, C. J., Midlatitude ionospheric D region: Height, sharpness, and solar zenith angle. 2017, *Journal of Geophysical Research: Space Physics*, **122**, 8933, DOI: 10.1002/2017JA024455
- Thomson, N. R., Rodger, C. J., & Clilverd, M. A., Large solar flares and their ionospheric D region enhancements. 2005, *Journal of Geophysical Research (Space Physics)*, **110**, A06306, DOI: 10.1029/2005JA011008
- Todorović-Drakul, M., Čadež, V., Bajčetić, J., et al., Behaviour of electron content in the ionospheric D-region during solar X-ray flares. 2016, *Serbian Astronomical Journal*, **2016**, 11, DOI: 10.2298/SAJ160404006T
- Wait, J. R. & Spies, K. P. 1964, *Characteristics of the Earth-ionosphere waveguide for VLF radio waves*, NBS Technical Note, CO
- Wautelet, G. 2013, Characterization of Ionospheric Irregularities and Their Influence on High-Accuracy Positioning with GPS over Mid-Latitudes, Doctoral dissertation, University of Liège, Belgium

Analysis of laser induced plasma plume in atmosphere using deep learning

M.S. Rabasovic , B.P. Marinkovic  and D. Sevic 

Institute of Physics, University of Belgrade, Pregrevica 118, 11080 Zemun, Serbia (E-mail: sevic@ipb.ac.rs)

Received: July 27, 2022; Accepted: October 12, 2022

Abstract. The regression analysis of spectra of laser initiated electric discharge spark in atmosphere is presented here. Spectral images of optical emission of atmospheric plasma are obtained by a streak camera and integrated in time to obtain sample spectra of plasma with different apparent temperatures. We already have analyzed such spectra using principal component analysis and classification techniques. Now, we have advanced research through the ANN and deep learning technique. Namely, large set of measured spectra are used to train the artificial neural network to obtain the estimation of apparent plasma temperature. For machine learning approach to data analysis we use Solo+Mia software package (Version 9.0, Eigenvector Research Inc, USA).

Key words: Machine learning – Deep learning – Laser induced breakdown spectroscopy

1. Introduction

Various machine learning (ML) techniques are used more and more for analysis of LIBS data. The combination of the popular machine learning algorithms (PCA and LDA, unsupervised and supervised techniques, respectively) with LIBS are used to complete rapid and precise classification of different samples Bellou et al. (2020); Diaz et al. (2020); Pořízka et al. (2018); Yang et al. (2020); Zhang et al. (2022). An artificial neural network (ANN) algorithm is also used for the determination of electron temperature and electron number density in LIBS Borges et al. (2014); D'Andrea et al. (2015) The advantage of ANNs is in the possibility of reproducing nonlinear relations between the inputs and the output(s).

In our recent work we have combined several machine learning techniques, such as K-nearest neighbors classification together with clustering algorithms in supervised manner which is possible in SOLO software, in order to estimate apparent plasma temperature Rabasovic et al. (2022). In that study we have analyzed the possibilities of using ML for analysis of optical spectra emitted by laser induced breakdown and electric discharge spark in atmosphere.

Now, we have advanced research through the ANN and deep learning technique. Namely, set of measured spectra, of copper plasma in air, similarly obtained as in [Rabasovic et al. \(2022\)](#), are used to train the artificial neural network to achieve the estimation of apparent plasma temperature. For machine learning approach to data analysis we use Solo+Mia software package (Version 9.0, Eigenvector Research Inc, USA) [Wise et al. \(2006\)](#).

2. Methods

Our experimental set-up for obtaining the training spectra for deep learning ANN (ANNDL) is explained in detail in [Rabasovic et al. \(2022\)](#). Shortly, spectral images of optical emission of atmospheric plasma are obtained by a streak camera and integrated in time to obtain sample spectra of plasma with different temperatures. It should be pointed out that, because streak images are resolved in time, we were capable to select time windows for integrating spectra in such a way that intensive optical emission of initial plasma was not included. The apparent electron temperature was calculated using the well known Boltzman plot technique, assuming a local thermal equilibrium (LTE) and also that the plasma is optically thin (absorption and scattering can be neglected) [Asamoah & Hongbing \(2017\)](#); [Shaikh et al. \(2006\)](#). The measured copper atomic lines at wavelength of 510, 515 and 522 nm were used to calculate the electron temperature.

For training the ANNDL we have used the set of 55 copper spectra for input vectors. As output vector we have used the set of calculated apparent electron temperatures of plasma, corresponding to those 55 input vectors.

3. Results and discussion

Measured (calculated by Boltzman plot) temperatures of training set are shown in [Fig. 1](#). Plot of predicted temperatures looks much the same, so we omit to present it here.

The general idea of estimating the electron temperature using ANNDL is to train the network using sample spectra for which the temperature is calculated using Boltzman plot. Through training phase the network iteratively minimizes errors between the calculated and predicted temperatures.

Residuals (differences) between the calculated (used for training) and predicted temperatures obtained by deep learning neural network model are shown in [Fig. 2](#). Errors for the samples inside the training set are relatively small, about 1.25 % is the largest one.

After feeding the network with samples with known, calculated temperatures, and if we were satisfied that residuals are acceptably small, the network could be fed by spectra not seen before.

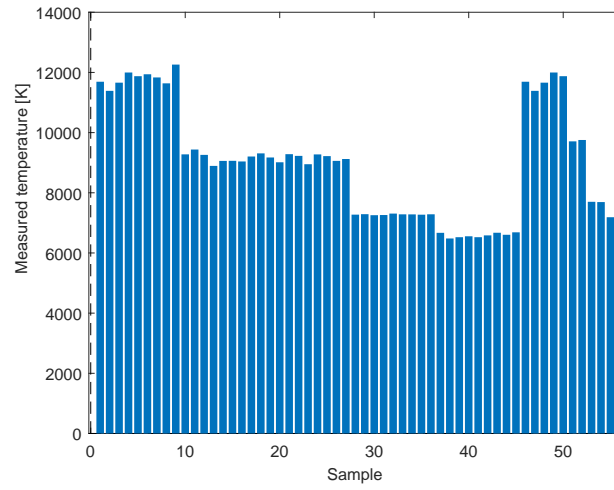


Figure 1. Measured (calculated by Boltzman plot) temperatures of training set.

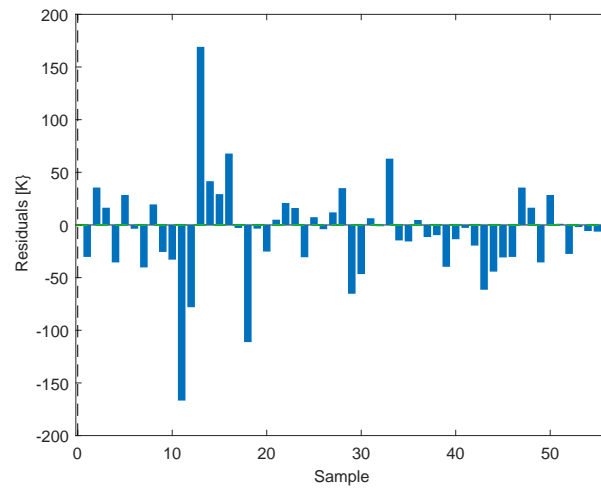


Figure 2. Residuals (differences) between the calculated (used for training) and predicted temperatures obtained by deep learning neural network model.

Table 1. Calculated (using Boltzman plot) and by deep learning neural network predicted temperatures of test samples and their differences.

Test sample	Temperature [K]		
	Calculated	Predicted	Difference
1	11595	11748	-152
2	9400	9221	178
3	8609	9014	-405
4	7331	7283	49
5	6631	6610	21

Fig. 3 shows the predicted temperatures of 5 test samples. Table 1 shows calculated (using Boltzman plot) and by deep learning neural network predicted temperatures of test samples and their differences.

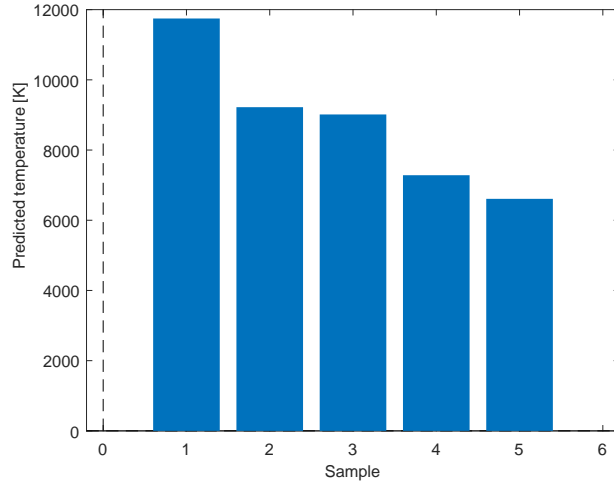


Figure 3. Predicted temperatures of 5 test samples.

Systematic errors when using Boltzman plot come mainly from the uncertainties in the transition probabilities and the measurement of the intensity of spectral lines [Shaikh et al. \(2006\)](#), where uncertainties are estimated to be at least 10 %, so estimation errors visible in Table 1 look fully acceptable. The largest error is about 4.7 %.

4. Conclusions and Discussion

We have used deep learning ANN to estimate the electron temperature of plasma. We have proved that, instead of using the usual way of identifying the spectral peaks and calculating their intensity ratio, it is possible to train the computer by feeding the ANN DL by known spectra with calculated temperatures to estimate the temperature of the spectra not seen before.

Acknowledgements. This work was financially supported by funding provided by the Institute of Physics Belgrade, through the grant by the Ministry of Education, Science and Technological Development of the Republic of Serbia.

References

- Asamoah, E. & Hongbing, Y., Influence of laser energy on the electron temperature of a laser-induced Mg plasma. 2017, *Applied Physics B: Lasers and Optics*, **123**, 22, DOI: 10.1007/s00340-016-6617-3
- Bellou, E., Gyftokostas, N., Stefan, D., Gazeli, O., & Couris, S., Laser-induced breakdown spectroscopy assisted by machine learning for olive oils classification: The effect of the experimental parameters. 2020, *Spectrochimica Acta*, **163**, 105746, DOI: 10.1016/j.sab.2019.105746
- Borges, F. O., Cavalcanti, G. H., Gomes, G. C., Palleschi, V., & Mello, A., A fast method for the calculation of electron number density and temperature in laser-induced breakdown spectroscopy plasmas using artificial neural networks. 2014, *Applied Physics B: Lasers and Optics*, **117**, 437, DOI: 10.1007/s00340-014-5852-8
- D'Andrea, E., Pagnotta, S., Grifoni, E., et al., A hybrid calibration-free/artificial neural networks approach to the quantitative analysis of LIBS spectra. 2015, *Applied Physics B: Lasers and Optics*, **118**, 353, DOI: 10.1007/s00340-014-5990-z
- Diaz, D., Molina, A., & Hahn, D. W., Laser-Induced Breakdown Spectroscopy and Principal Component Analysis for the Classification of Spectra from Gold-Bearing Ores. 2020, *Applied Spectroscopy*, **74**, 42, DOI: 10.1177/0003702819881444
- Pořízka, P., Klus, J., Képeš, E., et al., On the utilization of principal component analysis in laser-induced breakdown spectroscopy data analysis, a review. 2018, *Spectrochimica Acta*, **148**, 65, DOI: 10.1016/j.sab.2018.05.030
- Rabasovic, M. S., Marinkovic, B. P., & Sevic, D., Time resolved study of laser triggered electric discharge spark in atmosphere: Machine learning approach. 2022, *Advances in Space Research*, In Press, DOI: 10.1016/j.asr.2022.04.046
- Shaikh, N. M., Hafeez, S., Rashid, B., Mahmood, S., & Baig, M. A., Optical emission studies of the mercury plasma generated by the fundamental, second and third harmonics of a Nd : YAG laser. 2006, *Journal of Physics D Applied Physics*, **39**, 4377, DOI: 10.1088/0022-3727/39/20/013
- Wise, B. M., Gallagher, N. B., Bro, R., et al. 2006, *Chemometrics tutorial for PLS Toolbox and Solo*, ISBN: 0-9761184-1-6, Eigenvector Research, Inc. USA.

- Yang, Y., Hao, X., Zhang, L., & Ren, L., Application of Scikit and Keras Libraries for the Classification of Iron Ore Data Acquired by Laser-Induced Breakdown Spectroscopy (LIBS). 2020, *Sensors*, **20**, 1393, DOI: 10.3390/s20051393
- Zhang, D., Zhang, H., Zhao, Y., et al., A brief review of new data analysis methods of laser-induced breakdown spectroscopy: machine learning. 2022, *Applied Spectroscopy Reviews*, **57**, 89, DOI: 10.1080/05704928.2020.1843175

Influence of variations in the solar hydrogen Ly α radiation on the ionospheric D-region electron density during a year and solar cycle

A. Nina¹ , V.M. Čadež², L.Č. Popović^{2,3,4} and M. Radovanović^{5,6}

¹ *Institute of Physics Belgrade, University of Belgrade, 11080 Belgrade, Serbia (E-mail: sandrast@ipb.ac.rs)*

² *Astronomical Observatory, 11060 Belgrade, Serbia*

³ *Department of Astronomy, Faculty of mathematics, University of Belgrade, 11000 Belgrade, Serbia*

⁴ *Faculty of Science, University of Banja Luka, 78000 Banja Luka, R. Srpska, Bosnia and Herzegovina*

⁵ *Geographical Institute Jovan Cvijić SASA, 11000 Belgrade, Serbia*

⁶ *South Ural State University, Institute of Sports, Tourism and Service, 454080 Chelyabinsk, Russia*

Received: July 15, 2022; Accepted: October 10, 2022

Abstract. The hydrogen Ly α radiation emitted from the Sun is the main source of photo-ionization processes and, consequently, of the free electron production in the ionospheric D-region. Variations in the intensity of the incoming Ly α radiation affect changes in the electron density and they show up as periodic daily and seasonal changes, and changes during a solar cycle. The Quiet Ionospheric D-Region (QIonDR) model describes these periodic changes. In this study, we analyse how changes during a year and changes in the smoothed daily sunspot number (both processes affect the intensity of incoming radiation in the D-region) affect the electron density changes related to quiet conditions. The presented modelling is based on the results of the QIonDR model obtained for the part of Europe defined by the positions of the very low frequency (VLF) signal transmitters ICV (Sardinia, Italy) and DHO (Lower Saxony, Germany), and the AWESOME (Atmospheric Weather Electromagnetic System for Observation Modeling and Education) receiver position (Belgrade, Serbia) in application of the QIonDR model on real signals.

Key words: solar hydrogen Ly α line – ionospheric D-region – QIonDR model – VLF signals

1. Introduction

Study of the electron density dynamics in the ionosphere is of crucial importance for scientific research of many plasma parameters, and physical and chemical

processes in this atmospheric layer, as well as for modelling of the ionospheric influence on different kinds of electromagnetic waves. Variations in the ionospheric electron density occur as a result of numerous permanent influences coming from the outer space (Basak & Chakrabarti, 2013; Chakraborty & Basak, 2020; Nina, 2022) and terrestrial layers (Kumar et al., 2017; Nina et al., 2020), and their influence can be both periodical and aperiodical.

The most important source of the free electron production in the ionosphere is the solar radiation. Depending on the wavelength of the photons of this radiation, the efficiency in the considered photo-ionization processes depends on the altitude. Thus, the most significant parts of the spectrum that ionize the ionospheric D-region are the Ly α (121.6 nm) during quiet conditions and X-radiation generated by solar X-ray flares.

In this paper we analyse periodical variations of the ionospheric D-region electron density induced by local variations in the intensity of the solar hydrogen Ly α radiation at the considered area. We perform calculations based on Wait's model (Wait & Spies, 1964) by considering the ionosphere as a horizontally uniform medium with the electron density increasing exponentially with height according to an expression described by two independent, the so-called Wait's, parameters: the "sharpness", and the signal reflection height.

There are several procedures for the quiet ionosphere parameters determination. Generally, they are based on the broad-band detection of radio atmospherics in periods of lightning activities (Han et al., 2011; Ammar & Ghalila, 2020) and detection of the narrow-band very low frequency (VLF) signals (Thomson, 1993; McRae & Thomson, 2000; Thomson et al., 2011; Nina et al., 2021). In this paper, we analyse variations of the D-region electron density N depending on the smoothed daily sunspot number, σ , and on its variations in time (t) and on the day of year (DOY). We apply the Quiet ionospheric D-region (QIonDR) model (Nina et al., 2021) that provides dependencies of Wait's parameters on σ and DOY for the part of Europe defined by the positions of the VLF signal transmitters ICV (Sardinia, Italy) and DHO (Lower Saxony, Germany), and the AWESOME (Atmospheric Weather Electromagnetic System for Observation Modeling and Education) receiver (Belgrade, Serbia) which are used to develop this model. The mentioned dependences of these parameters in the QIonDR model were obtained by fitting relevant values calculated in processing of observational data during perturbations caused by 9 solar X-ray flares that occurred during all four seasons in the midday periods from 2009 to 2016. The application of the obtained functions enables the modelling of White's parameters and, consequently, the electron density in the D-region during quiet midday conditions without observational data only by DOY and σ (it can be obtained based on the appropriate data available on the Internet) entering into the calculations for the considered day.

2. Modelling

The electron density modelling is based on Wait's model of the ionosphere, which involves a horizontally uniform ionosphere described by two independent Wait's parameters, the "sharpness" (β) and the signal reflection height (H') and the expression from Thomson (1993):

$$N(\sigma, \chi, h) = 1.43 \cdot 10^{13} e^{-\beta(\sigma, \chi) H'(\sigma, \chi)} e^{[\beta(\sigma, \chi) - 0.15]h}, \quad (1)$$

where N , β and H' are given in m^{-3} , km^{-1} and km , respectively.

The dependencies of Wait's parameters on σ and the seasonal parameter χ are calculated using the QIonDR model (Nina et al., 2021):

$$\beta_0 = 0.2635 + 0.002573 \cdot \sigma - 9.024 \cdot 10^{-6} \sigma^2 + 0.005351 \cdot \cos(2\pi(\chi - 0.4712)), \quad (2)$$

and

$$H'_0 = 74.74 - 0.02984 \cdot \sigma + 0.5705 \cdot \cos(2\pi(\chi - 0.4712) + \pi). \quad (3)$$

These equations were obtained in the aforementioned study based on observational data of the DHO and ICV signals emitted in Germany (53.08 N, 7.61E) and Italy (40.92 N, 9.73 E), respectively, and recorded in Serbia (44.8 N, 20.4 E). For this reason, they are relevant for the area between these transmitters and receivers, i.e. approximately for the D-region above Central Europe.

Here, we point out that the uncertainties of the mentioned procedure are caused both by the approximations related to the White model of the ionosphere and by the approximations applied in the QIonDR model. These approximations primarily refer to considering the D-region as a horizontally uniform medium and the electron density distribution as an exponential function of height. In addition, the functional dependences of Wait's parameters on DOY and σ in the QIonDR model were obtained by fitting the relevant values of observational data for 9 analysed cases that met the analysis criteria. In specific cases, deviations of the relevant values from those given by these fitted functions are expected due to the constant influence of a large number of events and processes on the ionosphere.

The absolute variations of electron density due to changes in the observed σ and DOY are calculated based on the expressions:

$$\frac{\Delta N(\sigma(i), \chi(j), h)}{\Delta \sigma} = \frac{1}{2} (N(\sigma(i+1), \chi, h) - N(\sigma(i-1), \chi, h)), \quad (4)$$

and

$$\frac{\Delta N(\sigma(i), \chi(j), h)}{\Delta d} = \frac{1}{2} (N(\sigma(i), \chi(j+1), h) - N(\sigma(i), \chi(j-1), h)) \quad (5)$$

where the i -th value of $\sigma(i)$ is calculated using the expression $\sigma(i) = 19 + i$ ($i = 1, 2, 3, \dots, 101$), and the value of $\chi(j) = j/\text{NDY}$ ($j=1, 2, 3, \dots, \text{NDY}$, where NDY is the number of days in a year).

In this paper, the relative changes of the electron density with σ and DOY are analysed. They are calculated by dividing Eqs. (4) and (5) with the corresponding value of the electron density, respectively.

3. Results and discussion

In this Section, we present the results of modelling the electron density changes with σ (Section 3.1) and with DOY (Section 3.2). In both cases, we observe absolute and relative changes in the electron density at heights $H= 60$ km, 70 km, 80 km and 90 km for all combinations of DOY and σ ranging between 20 to 120.

3.1. Solar cycle variations

The electron density changes during a year and solar cycle. Consequently, variations in the solar hydrogen Ly α radiation do not have the same effect on the D-region characteristics at different periods. To examine how changes in σ affect changes in electron density under different conditions, we study the dependencies of the derivatives $\frac{\Delta N}{\Delta \sigma}$ versus DOY and σ . The results of this modelling, based on the expressions given in Section 2, are shown in Fig. 1. Based on the obtained panels we can conclude the following:

- The tendencies of the absolute changes of N are the same for all D-region heights.
- The intensity of these changes increases with altitude. For observed heights that differ by 10 km, the values on the scales differ by more than one order of magnitude.

For small values of σ at 70 km, the obtained values of $\frac{\Delta N}{\Delta \sigma}$ are below 10^{-6} m $^{-3}$. Because of approximations taken in the QIonDR model, these values can be considered approximately equal to 0. By decreasing the height, the maximum values of σ to which this approximation is applied increase (the exact value depends on DOY).

- Changes in the electron density for the same DOY increase with σ .
- The most pronounced changes in $\frac{\Delta N}{\Delta \sigma}$ for all values of σ occur in the period around the summer solstice.

Bearing in mind that the electron density changes with height, we analyse its relative changes with sigma to determine the local significance of changes in emitted solar hydrogen Ly α radiation. For this reason, we apply the procedure

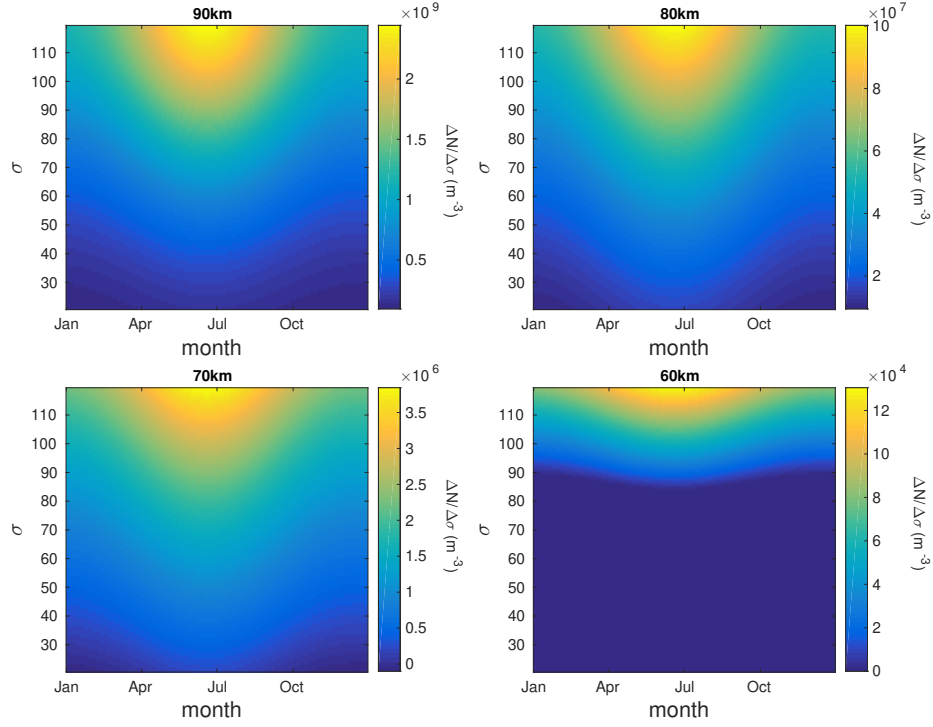


Figure 1. Ratio of variations ΔN and $\Delta\sigma$ $\frac{\Delta N}{\Delta\sigma}$, versus DOY and σ at heights $h=60, 70, 80$ and 90 km.

shown in the previous case to determine the dependencies $\frac{1}{\Delta\sigma} \frac{\Delta N}{N}$. Based on the obtained results visualized in Fig. 2, the following characteristics of $\frac{1}{\Delta\sigma} \frac{\Delta N}{N}$ changes can be observed:

- The maximum values of $\frac{1}{\Delta\sigma} \frac{\Delta N}{N}$ at all D-region heights are within one order of magnitude for the observed values of σ , and they increase with height;
- The maximum considered relative changes occur in the summer solstice period.
- The maximum relative changes of N with the smoothed daily sunspot number occur at smaller values of σ with increasing height.
- As a consequence of the small values of $\frac{\Delta N}{\Delta\sigma}$ in the lower part of the D-region for lower values of σ , it can be concluded that the relative changes in these parameters are negligible.

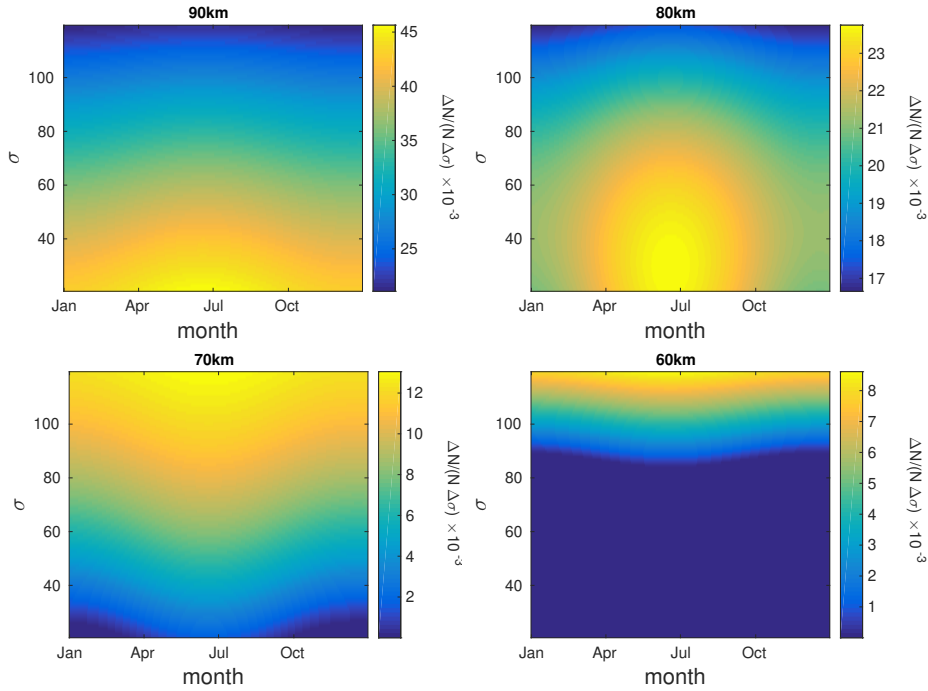


Figure 2. Dependencies of the relative changes in the electron density with the changes of the smoothed daily sunspot number, $\frac{\Delta N}{N \Delta \sigma}$, on DOY and σ at $h = 60, 70, 80$ and 90 km.

3.2. Seasonal variations

The analysis of the electron density absolute and relative changes with DOY is shown in a similar way as in the previous case.

Based on the obtained 3D dependencies of the electron density absolute changes shown in Fig. 3, the following conclusions can be drawn:

- The intensity of these changes increases with the height, and their maxima at the lower and upper boundaries of the D-region differ by about 4 orders of magnitude.
- From the winter to summer solstice $\frac{\Delta N}{\Delta d}$ is positive, while going from a summer to a winter solstice, this parameter is negative. Changes in the electron density with DOY are most pronounced during equinoxes.
- The influence of σ on $\frac{\Delta N(\sigma(i), X(j), h)}{\Delta d}$ increases with height.

The relative changes of the electron density (presented in Fig. 4) show the following characteristics:

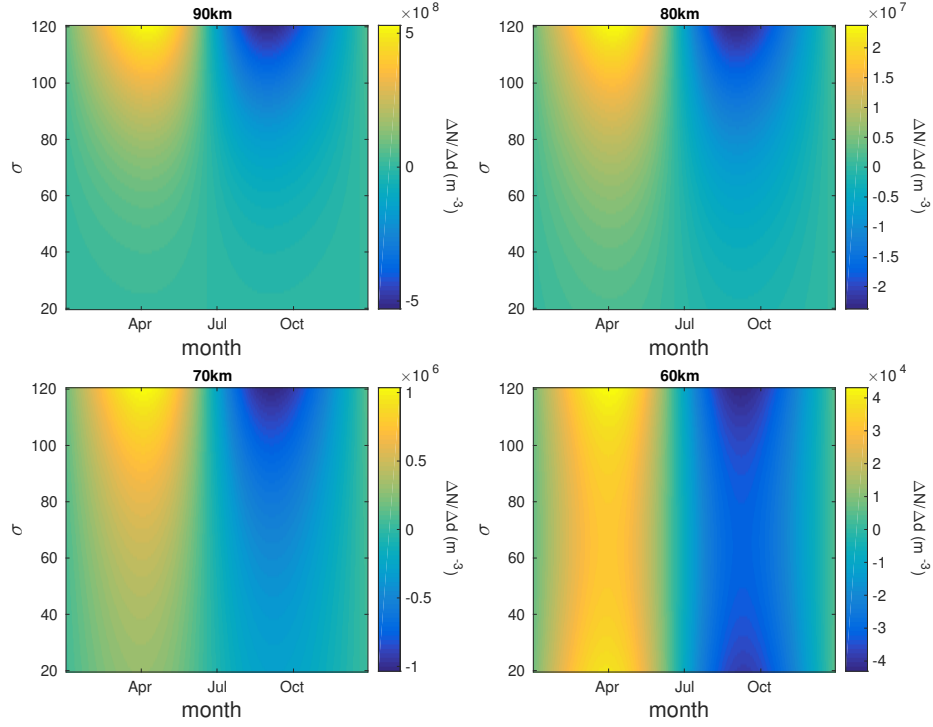


Figure 3. Dependencies of the absolute changes in the electron density with the day $\frac{\Delta N}{\Delta d}$, versus DOY and σ .

- The values of $\frac{1}{\Delta d} \frac{\Delta N}{N}$ for the same σ and for the same day are within one order of magnitude in the entire D-region.
- The influence of σ on the observed changes is not expressed. It is most pronounced during the summer and winter solstices.
- As in the case of absolute changes, $\frac{1}{\Delta d} \frac{\Delta N}{N}$ is positive in the period between the winter solstice and summer solstice, while going from the summer to winter solstice it is negative.

4. Conclusions

In this paper, the absolute and relative changes of the mid-day D-region electron density during a year and a solar cycle were analysed. The analyses are based on modelling the undisturbed ionospheric D-region by the QIonDR model. The obtained results show the following:

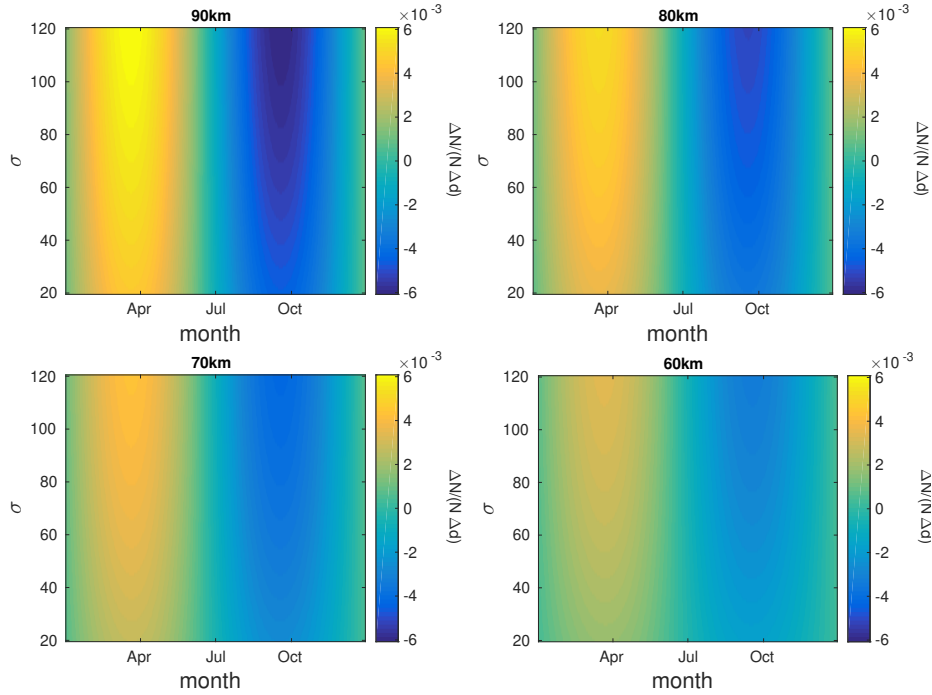


Figure 4. Dependencies of the relative changes in the electron density with the day $\frac{\Delta N}{N \Delta d}$, versus DOY and σ .

- Both, the absolute and relative changes in the electron density with the smoothed daily sunspot number and with the day of year increase with altitude.
- The maximum absolute changes at the upper and lower limits differ by about four orders of magnitude, while the corresponding maximum relative changes differ by about 2 times.
- Due to the small values of changes in the electron density with the smoothed daily sunspot number at the lower altitudes of the D-region, it can be considered that they are negligible for smaller values of the smoothed daily sunspot number.
- The maximum values of the observed changes in the electron density with the smoothed daily sunspot number are in the period of the solstices, while those changes with the day of year are most intense in the periods of equinoxes.

- The resulting assessment of the influence of the smoothed daily sunspot number on the observed changes in the electron density based on the QIonDR model has more complex characteristics than in the case of seasonal changes:
 - The absolute changes in the electron density with the smoothed daily sunspot number increase with this number at all altitudes throughout a year.
 - The maximum relative changes of the electron density with the smoothed daily sunspot number occur during the period of the summer solstice. The smoothed daily sunspot number corresponding to these maximum changes decrease with the D-region heights.
 - At higher altitudes, the absolute changes in the electron density with days at higher altitudes increase with the smoothed daily sunspot number.
 - The relative changes in the electron density with days increase with the smoothed daily sunspot number at all altitudes.

Finally, it should be emphasized that it is not possible to check the obtained dependencies on the basis of other models. Namely, some of the other existing models do not give dependences on both observed parameters, while some expressions use dependences on the Zürich sunspot number, which has been replaced by the international sunspot numbers since 1980. Therefore, it is necessary to verify the obtained conclusions in the future.

Acknowledgements. The authors acknowledge funding provided by the Institute of Physics Belgrade, the Astronomical Observatory (the contract 451-03-68/2020-14/200002) and the Geographical Institute "Jovan Cvijić" SASA through the grants by the Ministry of Education, Science, and Technological Development of the Republic of Serbia.

References

- Ammar, A. & Ghalila, H., Estimation of nighttime ionospheric D-region parameters using tweek atmospherics observed for the first time in the North African region. 2020, *Advances in Space Research*, **66**, 2528, DOI: 10.1016/j.asr.2020.08.025
- Basak, T. & Chakrabarti, S. K., Effective recombination coefficient and solar zenith angle effects on low-latitude D-region ionosphere evaluated from VLF signal amplitude and its time delay during X-ray solar flares. 2013, *Astrophysics and Space Science*, **348**, 315, DOI: 10.1007/s10509-013-1597-9
- Chakraborty, S. & Basak, T., Numerical analysis of electron density and response time delay during solar flares in mid-latitudinal lower ionosphere. 2020, *Astrophysics and Space Science*, **365**, 184, DOI: 10.1007/s10509-020-03903-5
- Han, F., Cummer, S. A., Li, J., & Lu, G., Daytime ionospheric D region sharpness derived from VLF radio atmospherics. 2011, *Journal of Geophysical Research (Space Physics)*, **116**, 5314, DOI: 10.1029/2010JA016299

- Kumar, S., NaitAmor, S., Chanrion, O., & Neubert, T., Perturbations to the lower ionosphere by tropical cyclone Evan in the South Pacific Region. 2017, *Journal of Geophysical Research: Space Physics*, **122**, 8720, DOI: 10.1002/2017JA024023
- McRae, W. M. & Thomson, N. R., VLF phase and amplitude: daytime ionospheric parameters. 2000, *Journal of Atmospheric and Solar-Terrestrial Physics*, **62**, 609, DOI: 10.1016/S1364-6826(00)00027-4
- Nina, A., Modelling of the Electron Density and Total Electron Content in the Quiet and Solar X-ray Flare Perturbed Ionospheric D-Region Based on Remote Sensing by VLF/LF Signals. 2022, *Remote Sensing*, **14**, DOI: 10.3390/rs14010054
- Nina, A., Nico, G., Mitrović, S. T., et al., Quiet Ionospheric D-Region (QIonDR) Model Based on VLF/LF Observations. 2021, *Remote Sensing*, **13**, DOI: 10.3390/rs13030483
- Nina, A., Pulnits, S., Biagi, P., et al., Variation in natural short-period ionospheric noise, and acoustic and gravity waves revealed by the amplitude analysis of a VLF radio signal on the occasion of the Kraljevo earthquake (Mw = 5.4). 2020, *Science of the Total Environment*, **710**, 136406, DOI: 10.1016/j.scitotenv.2019.136406
- Thomson, N. R., Experimental daytime VLF ionospheric parameters. 1993, *Journal of Atmospheric and Terrestrial Physics*, **55**, 173, DOI: 10.1016/0021-9169(93)90122-F
- Thomson, N. R., Rodger, C. J., & Clilverd, M. A., Daytime D region parameters from long-path VLF phase and amplitude. 2011, *Journal of Geophysical Research (Space Physics)*, **116**, 11305, DOI: 10.1029/2011JA016910
- Wait, J. R. & Spies, K. P. 1964, *Characteristics of the Earth-ionosphere waveguide for VLF radio waves*, , NBS Technical Note, CO

PRÁCE ASTRONOMICKÉHO OBSERVATÓRIA
NA SKALNATOM PLESE
LII, číslo 3

Zostavovatelia:	Dr. Vladimír A. Srečkovič Dr. Milan S. Dimitrijevič Dr. Nikola Cvetanovič
Výkonný redaktor:	RNDr. Richard Komžík, CSc.
Vedecký redaktor:	RNDr. Augustín Skopal, DrSc.
Vydal:	Astronomický ústav SAV, Tatranská Lomnica
IČO vydavateľa:	00 166 529
Periodicita:	3-krát ročne
ISSN (on-line verzia):	1336-0337
CODEN:	CAOPF8
Rok vydania:	2022
Počet strán:	142

Contributions of the Astronomical Observatory Skalnaté Pleso are processed using
L^AT_EX 2_ε CAOSP DocumentClass file 3.09 ver. 2022.